2D materials advances: from large scale synthesis and controlled heterostructures to improved characterization techniques, defects and applications

2016 2D Mater. 3 042001

(http://iopscience.iop.org/2053-1583/3/4/042001)

2D Materials

OPEN ACCESS

RECEIVED
12 October 2016

REVISED
11 November 2016

ACCEPTED FOR PUBLICATION
15 November 2016

PUBLISHED
8 December 2016

TOPICAL REVIEW

2D materials advances: from large scale synthesis and controlled heterostructures to improved characterization techniques, defects and applications

Zhong Lin[1,2,27], Amber McCreary[1,2,27], Natalie Briggs[2,3], Shruti Subramanian[2,3], Kehao Zhang[2,3], Yifan Sun[2,4], Xufan Li[5], Nicholas J Borys[6], Hongtao Yuan[7,8], Susan K Fullerton-Shirey[9], Alexey Chernikov[10,11], Hui Zhao[12], Stephen McDonnell[13], Aaron M Lindenberg[14,15], Kai Xiao[5], Brian J LeRoy[16], Marija Drndić[17], James C M Hwang[18], Jiwoong Park[19], Manish Chhowalla[20,21], Raymond E Schaak[2,4], Ali Javey[22,23], Mark C Hersam[24,25], Joshua Robinson[2,3,26] and Mauricio Terrones[1,2,3,4,26]

[1] Department of Physics, The Pennsylvania State University, University Park, PA 16802, USA
[2] Center for 2-Dimensional and Layered Materials, The Pennsylvania State University, University Park, PA 16802, USA
[3] Department of Materials Sciences and Engineering, The Pennsylvania State University, University Park, PA16802, USA
[4] Department of Chemistry, The Pennsylvania State University, University Park, PA 16802, USA
[5] Center for Nanophase Materials Sciences, Oak Ridge National Laboratory, Oak Ridge, TN 37831, USA
[6] Molecular Foundry, Lawrence Berkeley National Laboratory, Berkeley, CA 94720, USA
[7] Geballe Laboratory for Advanced Materials, Stanford University, Stanford, CA 94305, USA
[8] Stanford Institute for Materials and Energy Sciences, SLAC National Accelerator Laboratory, Menlo Park, CA 94025, USA
[9] Department of Chemical and Petroleum Engineering, University of Pittsburgh, Pittsburgh, PA 15213, USA
[10] Institut für Experimentelle und Angewandte Physik, Universität Regensburg, 93040 Regensburg, Germany
[11] Departments of Physics and Electrical Engineering, Columbia University, New York, NY 10027, USA
[12] Department of Physics and Astronomy, The University of Kansas, Lawrence, KS 66045, USA
[13] Department of Materials Science and Engineering, the University of Virginia, Charlottesville, VA 22904, USA
[14] Department of Materials Science and Engineering, Stanford University, Stanford, CA 94305, USA
[15] SLAC National Accelerator Laboratory, Menlo Park, CA 94025, USA
[16] Department of Physics, University of Arizona, Tucson, AZ 85721, USA
[17] Department of Physics and Astronomy, University of Pennsylvania, Philadelphia, PA 19104, USA
[18] Department of Electrical and Computer Engineering, Lehigh University, Bethlehem, PA 18015, USA
[19] Department of Chemistry and Institute of Molecular Engineering, University of Chicago, Chicago, IL 60637, USA
[20] Department of Materials Science and Engineering, Rutgers University, Piscataway, NJ 08854, USA
[21] Department of Electrical and Computer Engineering, Rutgers University, Piscataway, NJ 08854, USA
[22] Electrical Engineering and Computer Sciences, University of California at Berkeley, Berkeley, CA 94720, USA
[23] Materials Sciences Division, Lawrence Berkeley National Laboratory, Berkeley, CA 94720, USA
[24] Department of Materials Science and Engineering, Northwestern University, Evanston, IL 60208, USA
[25] Department of Chemistry, Northwestern University, Evanston, IL 60208, USA
[26] Center for Atomically Thin Multifunctional Coatings (ATOMIC), The Pennsylvania State University, University Park, PA 16802, USA
[27] Zhong Lin and Amber McCreary contributed equally to this work.

E-mail: mut11@psu.edu

Keywords: 2D materials, transition metal dichalcogenides, review

Abstract

The rise of two-dimensional (2D) materials research took place following the isolation of graphene in 2004. These new 2D materials include transition metal dichalcogenides, mono-elemental 2D sheets, and several carbide- and nitride-based materials. The number of publications related to these emerging materials has been drastically increasing over the last five years. Thus, through this comprehensive review, we aim to discuss the most recent groundbreaking discoveries as well as emerging opportunities and remaining challenges. This review starts out by delving into the improved methods of producing these new 2D materials via controlled exfoliation, metal organic chemical vapor deposition, and wet chemical means. We look into recent studies of doping as well as the optical properties of 2D materials and their heterostructures. Recent advances towards applications of these materials in 2D electronics are also reviewed, and include the tunnel MOSFET and ways to reduce the contact resistance for fabricating high-quality devices. Finally, several unique and innovative applications recently explored are discussed as well as perspectives of this exciting and fast moving field.

Nomenclature

1D	One-dimensional
2D	Two-dimensional
2DES	Two-dimensional electronic system
3D	Three-dimensional
AFM	Atomic force microscopy
Ag	Silver
Al_2O_3	Aluminum oxide
ALD	Atomic layer deposition
ARPES	Angle-resolved photoemission spectroscopy
Au	Gold
Bi	Bismuth
CBM	Conduction band minimum
CMOS	Complementary metal-oxide-semiconductor
CPGE	Circular photogalvanic effect
Cr	Chromium
CS_2	Carbon disulfide
$CsClO_4$	Cesium perchlorate
Cu	Copper
CVD	Chemical vapor deposition
DEME-TFSI	N,N-diethyl-N-methyl-N-(2-methoxyethyl) ammonium bis(trifluoromethylsulfonyl)imide
DFT	Density functional theory
DGU	Density gradient ultracentrifugation
DNA	Deoxyribonucleic acid
DOS	Density of states
D_{it}	Interface trap density
EBSD	Electron backscatter diffraction
EDL	Electric double layers
EDLTs	electric double layer transistors
EL	Electroluminescence
FET	Field effect transistor
FT-STS	Fourier transform scanning tunneling spectroscopy
GaN	Gallium nitride
GaSe	Gallium selenide
Ge	Germanium
GeSe	Germanium selenide
H_2S	Hydrogen sulfide
hBN	Hexagonal boron nitride
HfO_2	Hafnium oxide
HfS_2	Hafnium disulfide
HMDS	Hexamethyldisilazane
HOPG	Highly oriented pyrolytic graphite
HRSTEM	High resolution scanning transmission electron microscopy
HRTEM	High resolution transmission electron microscopy
HV	High vacuum
I_D	Source–drain current
IL	Ionic liquids
InAs	Indium arsenide
Ir	Iridium
LEED	Low energy electron diffraction
Mn	Manganese
Mo	Molybdenum
$MoCl_5$	Molybdenum(V) chloride
$Mo(CO)_6$	Molybdenum hexacarbonyl
MOCVD	Metalorganic chemical vapor deposition
MoS_2	Molybdenum disulfide
$MoSe_2$	Molybdenum diselenide
MOSFET	Metal-oxide-semiconductor field-effect transistor
$MoTe_2$	Molybdenum ditelluride
Na_2MoO_4	Sodium molybdate
Nb	Niobium
Ni	Nickel
O_2	Oxygen
Pb	Lead
PEO	Polyethylene oxide
PL	Photoluminescence
QY	Quantum yield
Re	Rhenium
RNA	Ribonucleic acid
S	Sulfur
Sb	Antimony
Sc	Scandium

Se	Selenium
SEM	Scanning electron microscopy
Si	Silicon
SiO_2	Silicon dioxide
Sn	Tin
SnS_2	Tin disulfide
SnSe	Tin selenide
$SnSe_2$	Tin diselenide
SPE	Solid polymer electrolytes
SPM	Scanning probe microscopy
STEM	Scanning transmission electron microscopy
STM	Scanning tunneling microscopy
STMDs	Semiconducting transition metal dichalcogenides
STS	Scanning tunneling spectroscopy
Te	Tellurium
TEM	Transmission electron microscopy
TERS	Tip-enhanced Raman scattering
TFETs	Tunneling field effect transistors
TFSI	Bis(trifluoromethane) sulfonamide
Ti	Titanium
TiO_2	Titanium oxide
TiOPc	Titanyl phthalocyanine
TiS_2	Titanium disulfide
TMDs	Transition metal dichalcogenides
UHV	Ultra-high vacuum
UV	Ultraviolet
V	Vanadium
VBM	Valence band maximum
vdW	van der Waals
V_G	Backgate voltage
VO_2	Vanadium oxide
W	Tungsten
$W(CO)_6$	Tungsten hexacarbonyl
WS_2	Tungsten disulfide
WSe_2	Tungsten diselenide
XPS	X-ray photoelectron spectroscopy
XRD	X-ray diffraction
ZrS_2	Zirconium disulfide

1. Introduction

The exfoliation of two-dimensional (2D) graphite, now known as graphene [1], has triggered world-wide research interest concerning atomically thin materials over the last decade. Although graphene was the first to be realized, many other materials exist in layered form, with interlayer interactions governed by van der Waals (vdW) forces. With appropriate methods, these materials can be thinned to a few layers and even monolayers, and are extensively studied today [2]. One group of such materials is the transition metal dichalcogenides (TMDs). Unlike graphene, which consists of an individual atom thick layer, TMDs follow a MX_2 structure, in which M is a transition metal (Mo, W, Re, Nb, etc) and X is a chalcogen atom (S, Se, or Te). Depending on the combination of M and X, the resulting material can vary from semiconducting to metallic and even superconducting [3]. Additionally, as the number of layers is reduced from the bulk crystal, the band structures of many TMDs distinctively change, resulting in a unique sensitivity of the TMD properties to thickness [4, 5]. Moreover, the semiconducting TMDs (STMDs) exhibit complementary properties to insulating and semi-metallic layered materials such as hBN and graphene [6]. Other layered materials besides graphene, TMDs, and hBN include mono-elemental 2D semiconductors (phosphorene, silicene, germanene, borophene), mono-chalcogenides (i.e. GaSe, SnSe), and MXenes (M = Ti, Nb, V, Ta, etc; X = C and N). Heterostructures of two or more of these atomically thin materials with a large library of bandgaps and electron affinities can be created to modulate and achieve a wide range of properties suitable for electronic and photonic applications [7–9]. Additional and unique degrees of freedom come from the ability to create stacked vdW heterostructures of different compositions, layer ordering and thickness, and interlayer orientation. However, these possibilities are in their infancy and the field of controlled heterostructures is just arising.

The excellent properties shown by 2D TMDs and their heterostructures, such as efficient light harvesting [10], sensitive photo-detection [11], and low-threshold lasing [12] make them promising materials for the next generation electronics and optoelectronics [2, 10–15]. The versatile properties of 2D TMDs can be tuned by band structure engineering to achieve, for example, band gap values matching the solar spectrum [16–19], suppress deep level defects [20], or to modulate the free carrier type and density [21–24] for field effect transistors (FETs) and p−n junctions—all being the essential elements for integrated electronics and optoelectronics. In addition, these materials can withstand large amounts of strain without degradation, and thus are excellent candidates for their use in

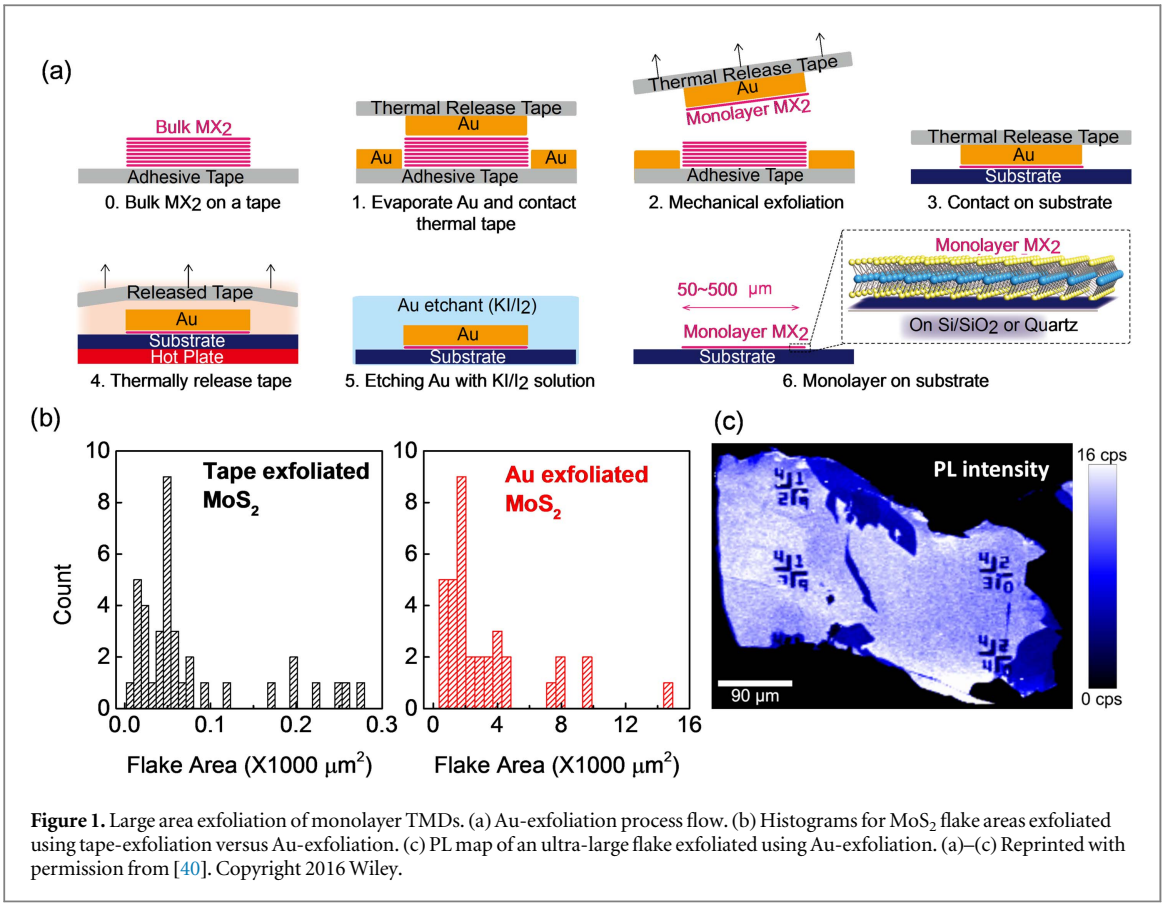

Figure 1. Large area exfoliation of monolayer TMDs. (a) Au-exfoliation process flow. (b) Histograms for MoS_2 flake areas exfoliated using tape-exfoliation versus Au-exfoliation. (c) PL map of an ultra-large flake exfoliated using Au-exfoliation. (a)–(c) Reprinted with permission from [40]. Copyright 2016 Wiley.

applications such as flexible, wearable electronics, and flexible smart phones or tablets [25–28].

Due to the fast pace of the 2D materials field, this review aims to highlight only the *most recent*, significant breakthroughs in 2D materials beyond graphene, being mindful of its potential significant emissions due to the global nature of this research. Specifically, we present advances in the areas of material synthesis, optical properties, doping, defect engineering, heterostructures, and applications of these materials such as 2D electronics and optoelectronics. We also provide perspectives and future outlooks. Summaries of earlier work are not provided herein, but can be found in other reviews [29–39].

2. Improved methods of material production

2.1. Large area exfoliation of TMD monolayers

Mechanical exfoliation (or '*Scotch Tape*' exfoliation) previously used for graphene [1] is one of the main techniques used to obtain TMD monolayers. The process relies on the probability of cleaving the bulk TMD crystal so that all layers except one remain adhered to the tape and only a monolayer is transferred onto the desired substrate. The size of monolayers obtained by standard tape-exfoliation is relatively small (~5 μm), their yield is poor, and the process is not selective towards the number of layers. The recently developed gold (Au)-mediated exfoliation method by the Javey group (figure 1(a)) enables selective exfoliation of ultra-large TMD monolayers (~500 μm) [40]. The Au-exfoliation process relies on the bonding of gold (thermally evaporated gold film; 100–150 nm thick) to the chalcogen atoms [41], which is stronger than that of the vdW bonds between the layers, thus allowing for the selective exfoliation of the topmost layer of a TMD source. Au-exfoliation achieves monolayers several orders larger in area when compared to tape-exfoliation (figure 1(b)), which is a major facilitator for research of these materials. This large size allows for the use of standard characterization techniques like x-ray diffraction (XRD), x-ray photoelectron spectroscopy (XPS), and angle-resolved photoemission spectroscopy (ARPES). The ultra-large Au-exfoliated monolayers possess similar optoelectronic quality as tape-exfoliated flakes as demonstrated by the photoluminescence (PL) maps (figure 1(c)).

2.2. Synthesis of large area TMD films via metalorganic chemical vapor deposition (MOCVD)

While chemical vapor deposition (CVD) provides a relatively simple route for synthesizing 2D materials, these methods do not always provide precise control over the grown materials and can often result in inhomogeneous films. Recently, however, homogeneous, wafer-scale films of MoS_2 and WS_2 have been demonstrated by Park's group through the use of MOCVD (figure 2(a)) [42]. Layer by layer growth of four-inch films of MoS_2 and WS_2 were achieved by

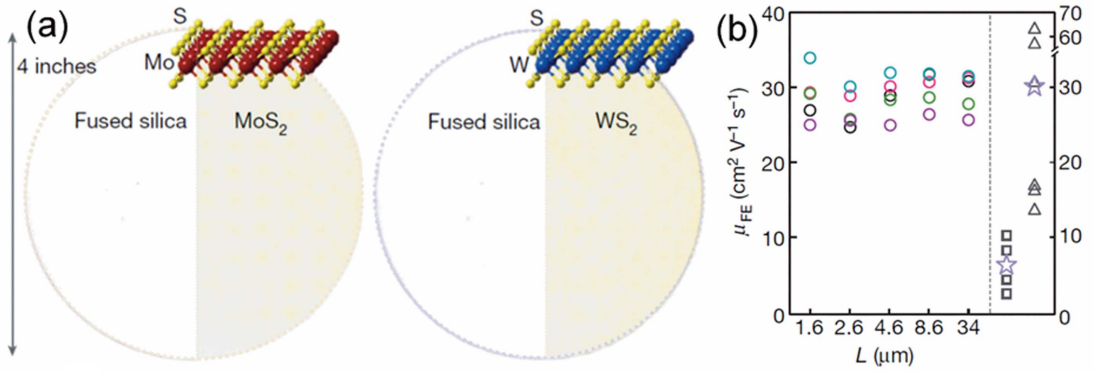

Figure 2. Synthesis of large area TMD films via MOCVD. (a) Photographs of MoS_2 and WS_2 monolayers grown on fused silica. The insets show their atomic structures. (b) Room temperature field effect mobility (circle) measurements of MoS_2 FETs fabricated with different channel length *L*. Values for CVD-grown (squares) and exfoliated (triangles) MoS_2 are included for comparison, where their median values are indicated by stars. (a) and (b) Reprinted with permission from [42]. Copyright 2015 Macmillan Publishers Ltd.

maintaining low partial pressures ($\sim 10^{-4}$ Torr) of the metalorganic precursors $Mo(CO)_6$, and $W(CO)_6$. The resulting films also displayed electrical properties comparable to those of mechanically exfoliated layers, with MoS_2 and WS_2 mobilities as high as 30 $cm^2\,V^{-1}\,s^{-1}$ and 18 $cm^2\,V^{-1}\,s^{-1}$ at room temperature, respectively (see figure 2(b)). Therefore, these studies have demonstrated the scalability when synthesizing high-quality, large-area 2D TMDs, thus opening the door to their industrial fabrication (wafer-size scale) and device assembly.

2.3. Colloidal synthesis of 2D metal chalcogenides

Solution (wet chemical) methods offer synthesis procedures that occur at much lower temperatures when compared to CVD or MOCVD. They are being developed for the synthesis of colloidal quantum dots, noble metal nanoparticles, and other classes of nanostructured materials [43]. Experimental parameters such as temperature, chemical reagents, and concentrations can often be modified to tune the shape, size, and uniformity of the solution-grown nanostructures. However, methods to produce colloidal TMDs in high yield with rigorous control over shape, size, and uniformity, as well as layer thickness that defines their characteristic size-dependent properties, do not yet exist. Ideal solution routes to TMD nanostructure formation should be scalable, high-yielding, and phase-controllable, thus permitting the formation of TMDs and TMD superlattices with controlled morphologies and thicknesses. Towards that goal, recent progress has been made in understanding how 2D TMD systems nucleate and grow in solution, identifying empirical guidelines for controlling their morphology and crystal structure, and setting the stage for the formation of colloidal nanosheet superstructures.

2D TMDs that nucleate and grow directly from soluble reagents in solution offer material characteristics that are complementary to those of their substrate-grown analogs discussed above [44, 45]. Over the past few years, $MoSe_2$ and MoS_2 have been among the most studied colloidal TMD systems. Solution-grown TMDs have a tendency to form agglomerated, and/or flower-like nanostructures that minimize the overall surface energy [46]. For the colloidal synthesis of $MoSe_2$ nanoflowers, it has been shown that as the reaction progresses, small $MoSe_2$ nanoflower-shaped particles first form, and continue growing by an outward radial growth of few-layer $MoSe_2$ nanosheets (figures 3(a)–(d)) [47]. The diameters of the uniform colloidal $MoSe_2$ nanoflowers could be tuned from 50–250 nm. Raman spectra of the $MoSe_2$ nanoflowers exhibited a reversible and dynamic variation of the out-of-plane vibration mode position (A_{1g}) when employing different laser powers, which was attributed to laser-induced interlayer decoupling by thermal modulation.

The key to synthesizing nanosheets of monolayer and few-layer TMDs in colloidal solutions is to identify conditions that facilitate anisotropic growth while preventing agglomeration. Working towards this goal, the formations of ZrS_2, TiS_2, and HfS_2 have recently been realized, where it was found that continuous influx of H_2S from the slow *in situ* decomposition of 1-dodecanethiol promoted lateral growth of monolayer nanosheets while a burst influx of H_2S from the rapid decomposition of CS_2 produced multi-layer nanodisks [48]. For $MoSe_2$ and WSe_2, it has been shown that judicious choice of capping ligands is needed to modulate edge-site binding affinities leading to tunability of nanosheet thickness [49].

Previous studies of the formation of SnSe nanosheets, similar to those described above for analyzing the formation of $MoSe_2$ nanoflowers, revealed that these metal monochalcogenides first grow laterally in solution and then vertically, with thicknesses tunable based on the reagent concentration [50]. Such growth processes can be considered as lateral and vertical homo-growth modes, since the same material is

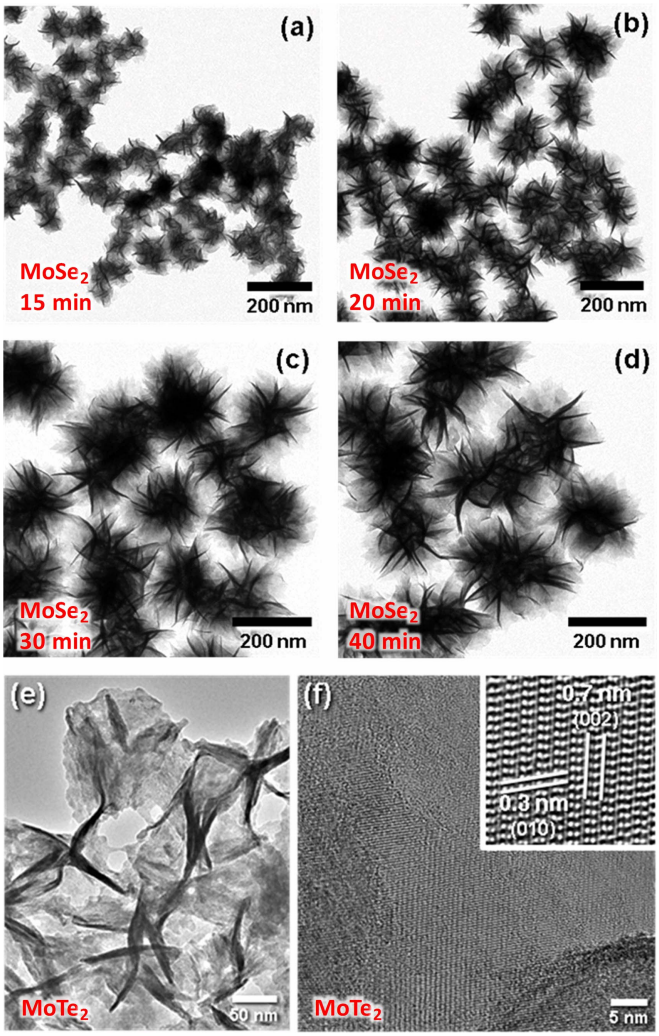

Figure 3. Colloidal synthesis of TMDs. TEM images characterizing the formation of colloidal $MoSe_2$ nanoflowers during the course of the reaction, taken at (a) 15 min, (b) 20 min, (c) 30 min, and (d) 40 min time points. (a)–(d) Reprinted with permission from [47]. Copyright 2015 American Chemical Society. (e) Low- and (f) high-magnification TEM images of 1T′–$MoTe_2$ nanostructures comprised of curled polycrystalline nanosheets. (e) and (f) Reprinted with permission from [58]. Copyright 2016 Wiley.

involved in both steps. By exploiting these distinct lateral and vertical growth modes, it may be possible to achieve analogous heterostructures, such as SnSe nanosheets growing directly on the surface of crystallographically related GeSe nanosheets.

In addition to controlling morphology, thickness, and vertical stacking, solution methods can also facilitate the formation of metastable TMD polymorphs that are typically challenging. In this context, colloidal nanostructures of the 2H- and 1T-polymorphs of WS_2 have been obtained in solution by including or excluding hexamethyldisilazane (HMDS), a putative coordinating ligand, respectively [51]. Interestingly, these subtle synthetic differences that produced different polymorphs also led to different morphologies (nanosheets and nanoflowers), which was attributed to differences in electrostatic stabilization of the two types of colloidal particles.

Among TMDs, $MoTe_2$ has emerged as a particularly interesting system for studying and achieving phase engineering. The stable 2H–$MoTe_2$ polymorph is semiconducting while the metastable 1T′–$MoTe_2$ polymorph is semimetallic; the 2H- and 1T′-phases are separated by only a small energy difference [52]. Calculations predict that the 2H–1T′ phase transition of $MoTe_2$ is more accessible under lattice strain than disulfide and diselenide systems, and adsorption of molecules and atoms on the surfaces of $MoTe_2$ monolayers can potentially induce the 2H–1T′ structural transition [53–55]. While defect creation via annealing or laser irradiation has been employed to access the metastable 1T′ polymorph, the small energy difference between 1T′- and 2H–$MoTe_2$ makes it challenging to selectively target one polymorph [56, 57]. Direct low-temperature solution synthesis of the metastable 1T′–$MoTe_2$ polymorph was achieved by injecting an oleic acid solution of $MoCl_5$ dropwise into trioctylphosphine, trioctylphosphine-telluride, oleylamine, and HMDS at 300 °C [58]. The 1T′–$MoTe_2$ nanostructures appeared as uniform nanoflowers (figure 3(e)) comprised of polycrystalline, few-layer nanosheets that exhibited a ~1% lateral compression

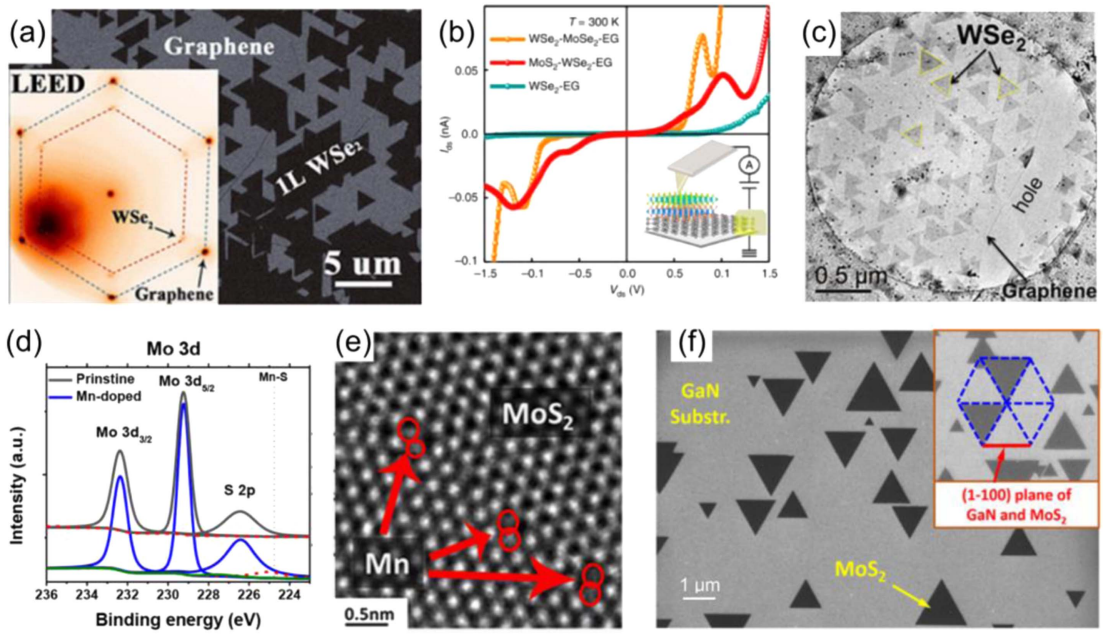

Figure 4. Effects of the substrate. (a) SEM image of WSe_2 on epitaxial graphene and LEED pattern of WSe_2/graphene, showing the close azimuthal alignment. Reprinted with permission from [71]. Copyright 2014 American Chemical Society. (b) Conductive AFM image of vdW heterostructures on graphene, showing the sharp negative differential resistance behavior. Reprinted with permission from [77]. Copyright 2015 Macmillan Publishers Ltd. (c) Low-resolution TEM image of WSe_2 directly grown on graphene/TEM grid, showing a clean film without polymer residues resulting from transfer process. Reprinted with permission from [63]. Copyright 2015 American Chemical Society. (d) XPS spectrum of pristine and Mn-doped MoS_2 grown on graphene. It is clear that the Mn-S binding is detected when the doping is on graphene. Reprinted with permission from [78]. Copyright 2015 American Chemical Society. (e) HRSTEM image of a Mn-doped MoS_2 monolayer on suspended graphene. Mn atoms are identified in the Mo site, showing direct evidence of substitutional doping. Reprinted with permission from [78]. Copyright 2015 American Chemical Society. (f) SEM image of MoS_2 on GaN, where ~100% of the MoS_2 triangular domains are aligned to the symmetry equivalent orientations. The EBSD image (inset) indicates that the MoS_2 on GaN is aligned to the $(1\bar{1}00)$ plane. Reprinted with permission from [64]. Copyright 2016 American Chemical Society.

relative to bulk 1T′–$MoTe_2$. Density functional theory (DFT) calculations suggested that grain boundary pinning in the polycrystalline structure, which contains ~10 nm 1T′–$MoTe_2$ domains (figure 3(f)), effectively suppressed its transformation back to the more stable 2H-polymorph and stabilized the 1T′ phase in the $MoTe_2$ nanostructures.

3. Doping and heterostructures of 2D materials

3.1. Substrate impacts and importance for doping 2D materials

The synthesis of any film, regardless of its dimensions, typically requires a substrate. In the case of 2D materials, insulating substrates such as sapphire and SiO_2 are often preferred [59, 60]. Conducting substrates such as Au and graphene are used for electrocatalysts [61], stacking of vdW heterostructures [62], and advanced atomic characterization [63]. Semiconducting substrates such as GaN [64], VO_2 [65], and other functional oxide substrates [66] are also becoming important due to their unusual properties that can be realized by combining novel substrates with 2D materials. Therefore, the substrate becomes a new tuning parameter in the CVD synthesis of 2D TMDs. Both two- and three-dimensional (3D) substrates and their relation to doping of 2D materials is discussed in this section.

The concept of 2D substrates has existed for decades [67, 68] and has been revitalized in recent years. Most recently, graphene has been utilized as a substrate for the growth of MoS_2 [69], WS_2 [70], WSe_2 [71], and GaSe [72], while sulfide-based chalcogenides can serve as substrates for nitride epitaxy [73]. For graphene-based substrates, MoS_2 and WSe_2 monolayers are well aligned in the symmetry equivalent orientation (figure 4(a)) even though MoS_2/graphene and WSe_2/graphene exhibit >20% lattice mismatch [74–76]. The low energy electron diffraction (LEED) pattern also confirms the close azimuthal alignment between WSe_2 and graphene (figure 4(a) inset). Conducting AFM characterization of graphene-based vdW heterostructures reveals sharp negative differential resistance due to the presence of pristine interfaces that can be achieved in such structures (figure 4(b)) [77]. The direct growth of TMDs on suspended graphene also provides a good template for high-resolution transmission electron microscopy (HRTEM) to visualize the atomic structure of TMDs with minimal residues from the TEM sample preparation (figure 4(c)). Additionally, the first successful manganese doping of monolayer MoS_2 via powder vaporization was achieved only when graphene was used as the

substrate [78]. In this context, the XPS spectra (figure 4(d)) and scanning TEM (STEM) image (figure 4(e)) clearly indicate the substitutional doping of Mn at the Mo sites. It is believed that the inert surface of graphene provides better doping efficacy. It is noteworthy that 2D substrates, such as graphene, possess unique advantages for chalcogenide-based growth in structural, electronic, and electrical aspects. Therefore, further experiments should be carried out along this direction with the aim of increasing the crystalline domain sizes for device fabrication of different vdW solids.

It has been proposed that a defective 3D surface (sapphire, SiO_2) is responsible for the polycrystalline nature of CVD-grown TMDs [42, 79]. On the other hand, 3D substrates with lattices similar to TMDs can be good candidates for epitaxial growth of TMDs, regardless of the lattice mismatch. Considering the lattice constant and band gap of various 2D and 3D materials [73, 80], one would not expect to use sapphire as a preferred substrate given the >30% lattice mismatch. However, epitaxial growth of MoS_2 has been demonstrated on sapphire with >90% of the MoS_2 domains being aligned to symmetry-equivalent orientations [59]. Similarly, growth of WSe_2 on annealed sapphire also yielded a preferred orientation [81]. To probe the relationship between TMD orientation and sapphire, DFT calculations were conducted. It has been suggested that the adsorption energy at 0° and 60° exhibits a well-defined minima and maxima while it is flat for other orientations [59]. In addition, other theoretical evidence showed that the MoS_2/sapphire vdW binding energy is the lowest at 0° and 60° due to strain minimization of MoS_2 in these orientations [79]. While sapphire can provide an excellent substrate for single crystal 2D growth, 3D substrates in the nitride family have also been considered. Gallium nitride exhibits a similar lattice constant to MoS_2 (<1%), which lends itself to being an excellent 'active' substrate for epitaxy of 2D layered materials. MoS_2 growth on GaN was recently reported where it was demonstrated that ~100% of the MoS_2 domains are aligned on GaN substrates, indicating a lattice-matched substrate can be critical to the epitaxial growth of TMDs on 3D substrates (figure 4(f)) [64].

3.2. Isoelectronic doping and alloying of 2D monolayers and heterostructures

Due to the reduced dimension of 2D TMDs, isoelectronic doping is one of the most effective ways to engineer their band structure and tailor their properties for desired applications. For isoelectronic doping, the dopant atoms are electronically similar to those of the host. Isoelectronic dopants tend to more easily form alloys, impede the generation and multiplication of dislocations, and reduce the formation of amphoteric native defects [82]. Although isoelectronic dopants provide no extra electrons or holes, it is possible that their different electronegativity can introduce trapping potentials in the lattice to modulate the free carrier density and net conductivity behavior. So far, two types of 2D TMD isoelectronic alloys have been synthesized by substituting either isoelectronic chalcogens, e.g., $MoS_{2(1-x)}Se_{2x}$ [16–18], or transition metals, e.g., $Mo_xW_{1-x}S_2$, $Mo_{1-x}W_xSe_2$ [83–87]. These isoelectronic alloys show a continuous variation of band gap energy, resulting in PL with tunable emission wavelength in a wide spectral range [16–18, 83, 84]. It is well known that the electronic properties of TMDs are determined by the localization behavior of the d-orbitals of the transition metals [88]. The strong spin–orbit coupling of the d-orbitals can lead to large valence band splitting of several hundreds of meV [89], which can be exploited in the metal alloys (e.g., $Mo_{1-x}W_xSe_2$) to tune the degree of spin or valley polarization. This makes 2D TMD metal alloys especially attractive for band structure engineering and tuning of properties.

Theoretical calculations provide valuable rules for the choice of metal atoms and the design of 2D TMD metal alloys [90], which are specifically described as: (1) $|a_1 - a_2|/\max(a_1,a_2) < 0.034$, (2) $\Delta d_{M-X} < 0.1$ Å, and (3) $(E_{g1} > 0) \vee (E_{g2} > 0)$ (where a_1 and a_2 are the lattice constants of the two TMD materials, E_{g1} and E_{g2} are their band gaps, and Δd_{M-X} is the difference in the metal−chalcogen bond). Rules (1) and (2) require good matching between the lattice constants and metal−chalcogen bond distances, while rule (3) requires that at least one compound should be a semiconductor because the mixture of two metallic TMDs is not expected to display a finite band gap. The compound pairs selected theoretically based on the above three rules are plotted in figure 5(a), in which the pairs in the blue and red shaded areas are the most likely to be realized due to their smallest lattice mismatch. The pairs in the blue shaded region show the largest difference in band gap energies and are populated with Mo−V and W−V, representing TMD-based alloys between semiconducting MoX_2/WX_2 and metallic VX_2 (X = S, Se, Te). Alloying between MoX_2/WX_2 with electron deficient group-V metals like vanadium and niobium generally leads to degenerate p-doping with metallic behavior.

In contrast, the red shaded region in figure 5(a) features isoelectronic Mo−W pair, resulting in semiconductor−semiconductor MX_2−WX_2 alloys with good lattice matching and moderate band gap differences. In addition to abiding by these selection rules, the formation energies for $Mo_{1-x}W_xX_2$ alloys are negative due to similar electronic structures and increased attractive Coulomb interaction (caused by different atomic orbital energy and electronegativity of Mo and W) between MoX_2 and WX_2 [90, 91]. Thus, $Mo_{1-x}W_xX_2$ alloys are energetically favorable to be formed. Indeed, 2D $Mo_xW_{1-x}X_2$ alloys with tunable band gaps have been widely fabricated recently by

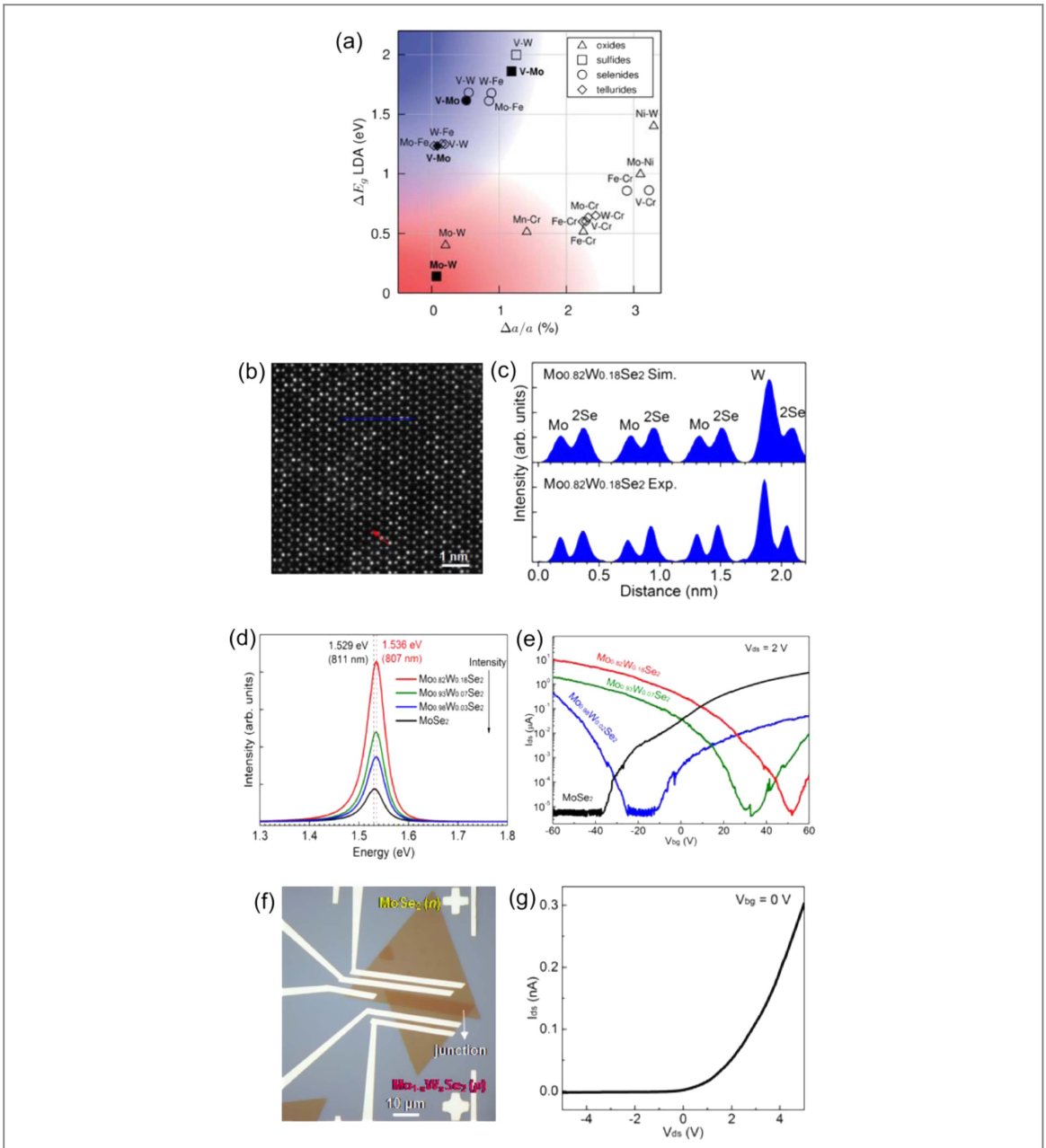

Figure 5. Isoelectronic doping and alloying of 2D TMDs. (a) Lattice constant matching and band gap difference for metal−metal pairs of 2H-TMDs based on theoretical calculations. Reprinted with permission from [90]. Copyright 2014 Royal Society of Chemistry. (b) Atomic resolution annular dark field-STEM image of isoelectronic monolayer $Mo_{0.82}W_{0.18}Se_2$. The brightest dots are W substituted Mo sites. The red arrow points to a Se vacancy. (c) Intensity line profiles along solid blue line in the (b). (d) PL spectra of monolayer $MoSe_2$ (solid black curve) and $Mo_{1-x}W_xSe_2$ with different W concentrations with 532 nm laser excitation. (e) Transfer curves of FET based on monolayer $MoSe_2$ (solid black curve) and $Mo_{1-x}W_xSe_2$ with different W concentrations (solid blue, green and red curves for $x = 0.02, 0.07,$ and 0.18, respectively). (f) Optical micrograph of a monolayer $MoSe_2$ (upper flake) transferred and stacked onto a monolayer $Mo_{0.82}W_{0.18}Se_2$ (lower flake). The overlapping region of the two flakes forms a homojunction. (g) Output curve of the junction, showing good current rectification. (b)–(g) Reprinted with permission from [92]. Copyright 2016 Wiley.

mechanical exfoliation from bulk alloy crystals or direct growth using CVD [32].

The tuning of optical and electrical properties (such as the carrier type) in isoelectronic 2D TMD alloys was first demonstrated in a CVD-grown monolayer $Mo_xW_{1-x}Se_2$ system [20, 92]. As has been widely reported, monolayer $MoSe_2$ is natively n-doped [93] and WSe_2 is intrinsically p-doped [94, 95], although the characteristics may vary with substrates or contact metals [96]. Since Mo and W have different d-orbital band energies and the band edges of $MoSe_2$ and WSe_2 are mainly determined by the contributions from these d-orbitals, it is reasonable to expect that without changing the fundamental band structure, 2D TMD alloys and homo-junctions based on isoelectronic substitution in the $MoSe_2$−WSe_2 system should provide uniform alloys with tunable band edge position as well as a modulation between p- or n-type doping. In these CVD-grown $Mo_xW_{1-x}Se_2$ monolayers, the W atoms uniformly incorporate into the monolayer $MoSe_2$ lattice by substitution of Mo, forming ideal random alloys (figures 5(b) and (c)). The random, isoelectronic

substitution of W atoms for Mo atoms in the monolayers of $Mo_{1-x}W_xSe_2$ effectively suppressed the Se vacancy concentration by 50% and deep levels compared to those in pristine $MoSe_2$ monolayers [20]. The resultant decrease of defect-mediated non-radiative recombination in the $Mo_{1-x}W_xSe_2$ monolayers yielded much enhanced PL (figure 5(d)) and extended the carrier lifetime by a factor of three compared to pristine $MoSe_2$ monolayers grown under similar conditions [20]. In addition to the enhancement of optical properties, the isoelectronic doping of W into $MoSe_2$ switches the dominant conduction type of the monolayer flakes, suppressing n-type conduction in monolayer $MoSe_2$ and enhancing p-type conduction with increasing W concentration. The p-type conduction becomes dominant with only ~18% of W substitution (figure 5(e)). In contrast to the above mentioned metal −semiconductor alloying that results in degenerate doping, the p-type doping in the monolayer $Mo_xW_{1-x}Se_2$ is non-degenerate. Monolayers of p-type $Mo_{1-x}W_xSe_2$ and n-type $MoSe_2$ were vertically stacked to form vdW p−n homo-junctions (figure 5(f)), showing gate-tunable current rectification (figure 5(g)) as well as long-persistent photoconductivity [92, 97]. Such tunable n- and p-type conduction realized within an isoelectronic monolayer alloy is highly encouraging as an important strategy to compensate doping with electron or hole donors to synthetically adjust the functionality of 2D TMD systems for many electronic and optoelectronic applications.

3.3. Electrolyte gating of 2D materials

Electrolyte gating has been used for nearly a decade to explore transport through 2D materials in the regime of high carrier density. Sheet carrier densities in the range of 10^{13}–10^{14} cm^{-2} have been induced by electrolytes in a variety of 2D materials, including but not limited to graphene [98–100], SnS_2 [101], MoS_2 [102, 103], WSe_2 [21, 104–106], black phosphorus [107], $MoTe_2$ [108, 109], and $SnSe_2$ [110]. These large doping densities arise from electrostatic interactions between ions in an electrolyte and induced image charge in a 2D crystal. In an electrolyte-gated 2D crystal FET, the gate dielectric is replaced by an electrolyte—a material with mobile cations and anions. Two electric double layers (EDLs), or Debye layers, form: one at the electrolyte-semiconductor interface, and the other at the electrolyte-gate interface. This approach is equivalent to moving the gate to within ~1 nm of the semiconductor interface, providing excellent gate control and ultrahigh capacitance density (2–20 $\mu F\ cm^{-2}$) [98–100, 102, 103, 109].

Electrolyte gating has been used to control transport in a variety of semiconducting materials [111, 112], but it is especially useful for 2D materials for several reasons. First, substitutional doping of 2D materials is less developed than electrostatic doping, although recent progress has been demonstrated for nitrogen doping of MoS_2 with little effect on the electronic properties of the 2D material [113]. Second, ion doping is a straightforward technique that does not require special equipment for deposition. Third, unlike substitutional doping, which is permanent, ion doping is reconfigurable and therefore the device can be configured as p- or n-type simply by reversing the polarity of the bias. Fourth, ion doping lowers contact resistance at the source and drain by thinning the Schottky barriers to charge injection [103, 105, 106]. Ionic liquids (IL) and solid polymer electrolytes (SPEs) are the most commonly used electrolytes for gating 2D materials. ILs are liquid salts while SPEs contain a salt dissolved in a polymer [114], typically polyethylene oxide (PEO).

Recently, electrolyte gating has been used as a tool to unlock exciting new physics in 2D materials. For example, an IL, DEME-TFSI, has been used to demonstrate spin polarization [21] and photogalvanic current [104] in WSe_2 FETs. This IL has also been used to create p–i–n junctions in monolayer and multi-layer WSe_2 that gives rise to current-induced circularly polarized electroluminescence (EL) [115]. The ability to reversibly create p–i–n and n–i–p junctions using electrolytes has been demonstrated on MoS_2 [116] and $MoTe_2$ [109]. In the four terminal $MoTe_2$ FET shown in figures 6(a)–(d), the inner two contacts are biased with opposite polarities, thereby accumulating anions and cations near the contacts, creating a p–i–n junction. When the temperature of the device is decreased below the glass transition temperature of the electrolyte (T_g = 243 K for PEO:$CsClO_4$), ion mobility is arrested and the ions are effectively 'locked' into the p–i–n configuration. This approach exploits the temperature-dependent ionic conductivity of the electrolyte. The bias can then be removed and the output characteristics show rectifying behavior between contacts 2–3 and 1–4 with an ideality factor of 2.3 (figure 6(f)).

In addition, there have been recent reports of superconductivity in electrolyte-gated TMDs such as MoS_2 [108, 117], 2H–$MoTe_2$ [108], 2H–$MoSe_2$ [108] and 2H–WS_2 [108]. However, as discussed by Shi and co-workers [108], a crossover from purely electrostatic gating to electrochemical gating is required to observe superconductivity in $MoTe_2$, $MoSe_2$, and WS_2. At an electrolyte V_G of 12 V—well exceeding the electrochemical window of the electrolyte—charge will be exchanged between the electrolyte and the semiconductor channel and metal contacts. Moreover, ions can be expected to intercalate between the layers of the 2D crystals [110]—a mechanism that is well studied by the battery community. It should be noted that intercalation and electrochemistry will alter the chemical identity of the TMD (i.e., ions are not simply inducing charge in the 2D crystal, they are bonding with the 2D crystal).

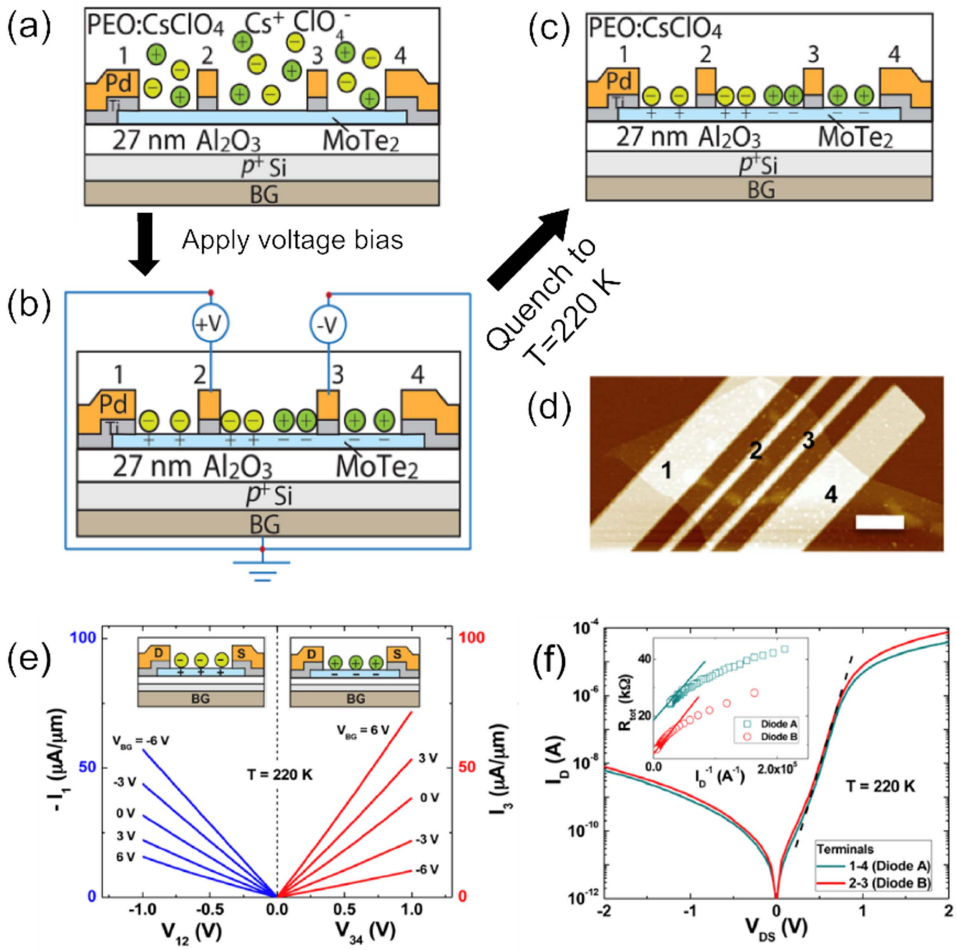

Figure 6. Electrolyte-gated FET schematic. Unipolar doping and p–i–n junction formation in $MoTe_2$ FETs using PEO:$CsClO_4$ solid polymer electrolyte at 220 K. (a)–(c) Mechanism for p–i–n junction formation using ions by applying V_{DS}. Ions are 'locked' into place by cooling the device to 220 K. (d) AFM scan of the device before depositing PEO:$CsClO_4$. Scale bar: 1 μm. (e) Common-source characteristics between terminals (i) 1–2 and 3–4. (f) Semi-log plot of the p–i–n junction, where the dashed line indicates the ideality factor. Inset: total differential resistance (R_{tot}) as a function of I_D^{-1}. (a)–(f) Reprinted with permission from [109]. Copyright 2015 American Chemical Society.

3.4. Imaging and spectroscopy of vdW heterostructures

In addition to the synthesis of individual and multi-layers of 2D materials, various methods have been developed to create their heterostructures. Successful fabrication techniques of vdW heterostructures have been carried out by sequentially assembling the 2D materials. A wide variety of layered materials have been used to create such heterostructures: TMDs, graphene, h-BN, and even topological insulators. While the basic techniques needed for this vdW assembly have been used for several years, recent advances allow for further control of the resulting structures, including the rotational degree of freedom [118]. Another degree of freedom that is beginning to be explored is the interlayer separation, which can significantly affect the interaction between the layers in these heterostructures [119].

Beyond the developments in creating these vdW heterostructures, measurement techniques at the atomic scale are necessary to characterize them, considering their electronic properties sensitively depend on parameters such as the rotation angle between layers. In general, determining this rotation angle is only possible with an atomically resolved measurement technique. Scanning probe microscopy (SPM) is especially well suited for determining angle rotations because it provides not only topographic information about the devices, but also electronic information. For example, consider a heterostructure consisting of two graphene layers. If the two layers are stacked with zero-degree rotation, then standard bilayer Bernal-stacked graphene is recovered. The density of states (DOS) of such a device is shown in figure 7(a) where the charge neutrality point (white dashed line) moves linearly with gate voltage because of the constant DOS. Beyond the DOS, the lack of a moiré pattern and the presence of a triangular lattice in the topography also confirm Bernal stacking. However, if a small twist angle is introduced between the layers, the linear graphene dispersion is preserved at low energy, but new van Hove singularities are created

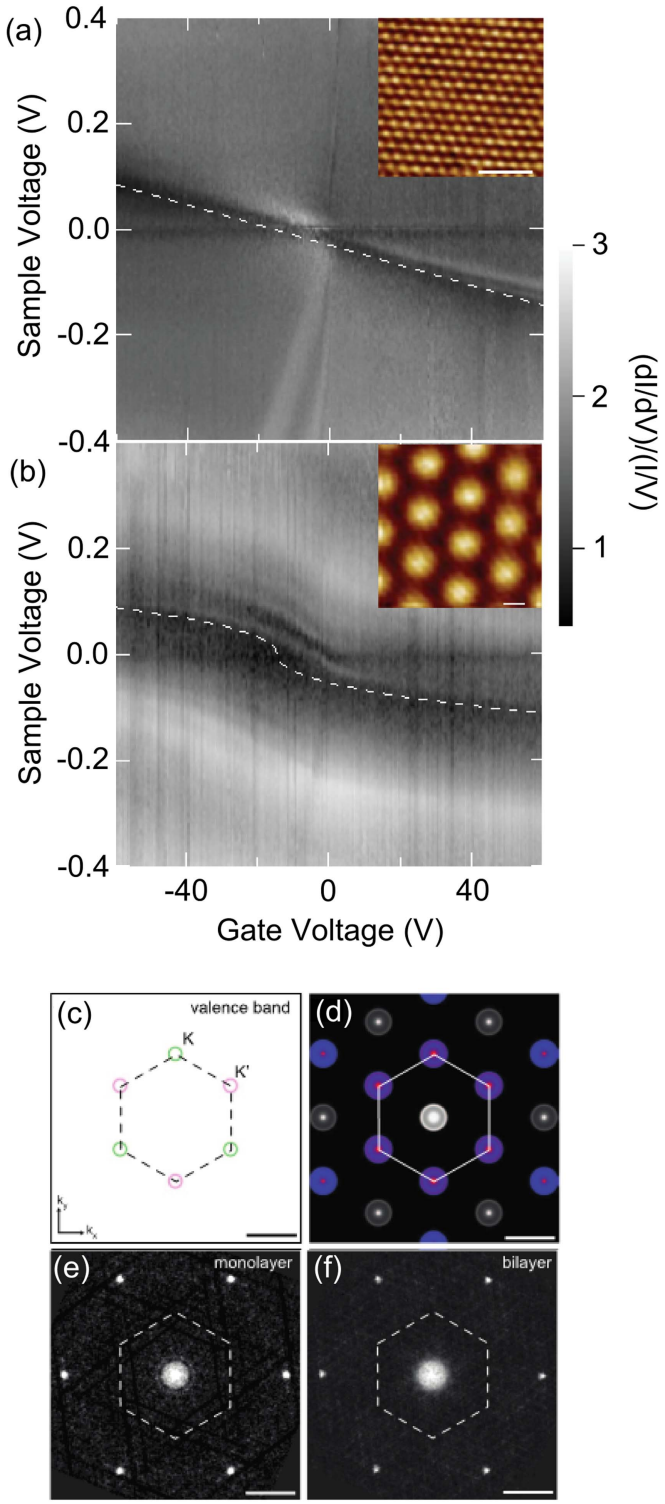

Figure 7. Imaging and spectroscopy on vdW heterostructures. (a) DOS as a function of energy and gate voltage for a Bernal stacked bilayer graphene device. The white dashed line tracks the charge neutrality point. The inset shows the corresponding topography of the device. The scale bar is 1 nm. Reprinted with permission from [118]. Copyright 2016 American Chemical Society. (b) DOS as a function of energy and V_G for a bilayer graphene device with a twist angle of ~2°. The inset shows the corresponding topography of the device which shows a moiré pattern with a wavelength of 7 nm. The scale bar is 3 nm. (c) General schematic of the low energy states in the valence band of WSe_2 with states at both K and K′. Green denotes spin-up bands and pink denotes spin-down bands. (d) Simulated joint DOS for the K-point bands in (c). Scattering resonances in white are always allowed while colored features are only possible without spin texture on the bands. (e) Experimental FT-STS for monolayer WSe_2 showing only the white resonances are present, indicating the spin polarization of the bands. (f) Experimental FT-STS for bilayer WSe_2 showing once again that only the white resonances occur. This is due to spin-valley-layer coupling in bilayer WSe_2. (c)–(f) Reprinted with permission from [123]. Copyright 2015 American Physical Society.

at an energy determined by the twist angle of the device [120]. Figure 7(b) shows such a bilayer graphene device with a ∼2° rotation between the layers. For a 2° rotation, the charge neutrality point moves with the square root of the gate voltage due to the linearly increasing DOS at higher energy. There are also new van Hove singularities created by the interaction between the graphene layers. When this structure is stacked on hBN, the competing interactions between the layers can cause many novel effects to emerge [121].

In these vdW heterostructures, STM can also provide information about quantities beyond the local DOS. Using Fourier transform scanning tunneling spectroscopy (FT-STS), momentum-resolved information about the heterostructure can be obtained by studying the energy dependence of the local DOS and Fourier transforming the result to obtain information in momentum space. This technique gives the allowed scattering wave vectors for the heterostructure. For example, in bilayer graphene, FT-STS can be used to map the changes in the band structure as a function of increasing electric field, which causes the bands to become broader and a band gap to open [122]. For heterostructures with TMDs, FT-STS also provides information about the spin texture of the different bands. Figures 7(c)–(f) shows typical results for WSe_2-based heterostructures [123]. In monolayer WSe_2, the spin-valley coupling forbids transitions from the *K* to K′ point without a spin flip. Therefore, these resonances are absent in the momentum resolved FT-STS images (figure 7(e)). In bilayer WSe_2, the spin degeneracy of the bands is restored at the K and K′ point. However, the layer polarization causes spin up electrons at K to reside on one layer and spin down on the other. The situation is reversed at the K′ point and therefore transitions between K and K′ are forbidden due to the spin-valley-layer coupling (figure 7(f)).

4. Optical properties of 2D materials

4.1. Impact of defects on photoluminescence quantum yield

Before 2D materials can be fully realized in devices, defects must be minimized. Defects are particularly important in a monolayer semiconductor where the carrier transport and generation/recombination is confined to a 2D plane. There are various techniques for characterizing defects in a semiconductor. One attractive technique is the PL quantum yield (QY), which is a fast and non-destructive method to quantify the performance of a semiconductor. QY is a quantity describing the ratio of emitted photons over absorbed photons. In a perfect semiconductor without any trap states, the only recombination mechanism at the low carrier concentration regime is radiative recombination, thus the internal QY approaches 100%. As defects and traps states are introduced, the non-radiative recombination rate increases, resulting in the reduction of the QY. It is also important to note the distinction between internal and external quantum yield. Environmental factors, such as the refractive index of the medium and multiple reflections of incident or emitted photons can strongly modulate the external QY by changing the fraction of light which can escape the sample, and it is not related to the material quality [124, 125].

Nominally, the internal QY of many 2D materials is quite poor, with typical values for MoS_2 in the range of 0.1%–1% and WS_2 showing the highest reported values (5%–20%) [4, 126]. Several recent studies have demonstrated that through the use of chemical surface treatment, defects in 2D material systems can be effectively passivated [127, 128]. In one of these studies [127], treatment in the organic superacid bis(trifluoromethane)sulfonimide (TFSI) was used to passivate the surface of MoS_2 (figure 8). Samples treated by TFSI show two orders of magnitude enhancement in the luminescence efficiency, with a final value near 100% [127]. This demonstrates that optoelectronically perfect monolayers can be obtained through chemical treatment of the surface. The treatment was shown to result in no change of the spectral shape and can result in uniform enhancement of the monolayer, as shown in figure 8(a). Due to the large exciton binding energies in TMDs, the recombination behavior differs substantially from III to V semiconductors. Specifically, Shockley–Reed–Hall recombination (non-radiative recombination of a free carrier with a defect site) is not observed under low-pumping conditions (corresponding to low concentration of optically generated carriers). The dramatic enhancement of the PL intensity also results in a corresponding increase in the minority carrier lifetime. As-exfoliated 2D materials have typically been characterized by extremely short lifetimes on the order of tens to hundreds of picoseconds, as shown in figure 8(f). After superacid treatment, a radiative lifetime of 10.8 ns was measured at low pump-fluence (figure 8(g)).

This superacid treatment technique has more recently been shown to also passivate WS_2 [129] as well as ultra-large area MoS_2 samples prepared by gold-mediated exfoliation [40], resulting in a QY near 100% in both cases. However, the TFSI treatment technique is ineffective for selenide based TMDs, including $MoSe_2$ and WSe_2, and other passivation schemes need to be identified [129]. Superacid treatment of synthetic MoS_2 monolayers prepared by CVD has also been demonstrated (figure 8(b)), with a final QY value of ∼30% for samples grown under optimal conditions [130].

These results present an important practical advance by demonstrating a route towards realization of high quality TMD monolayers processed over large areas through a simple chemical treatment. It is well known that defects can significantly degrade the performance of minority carrier devices. In addition to

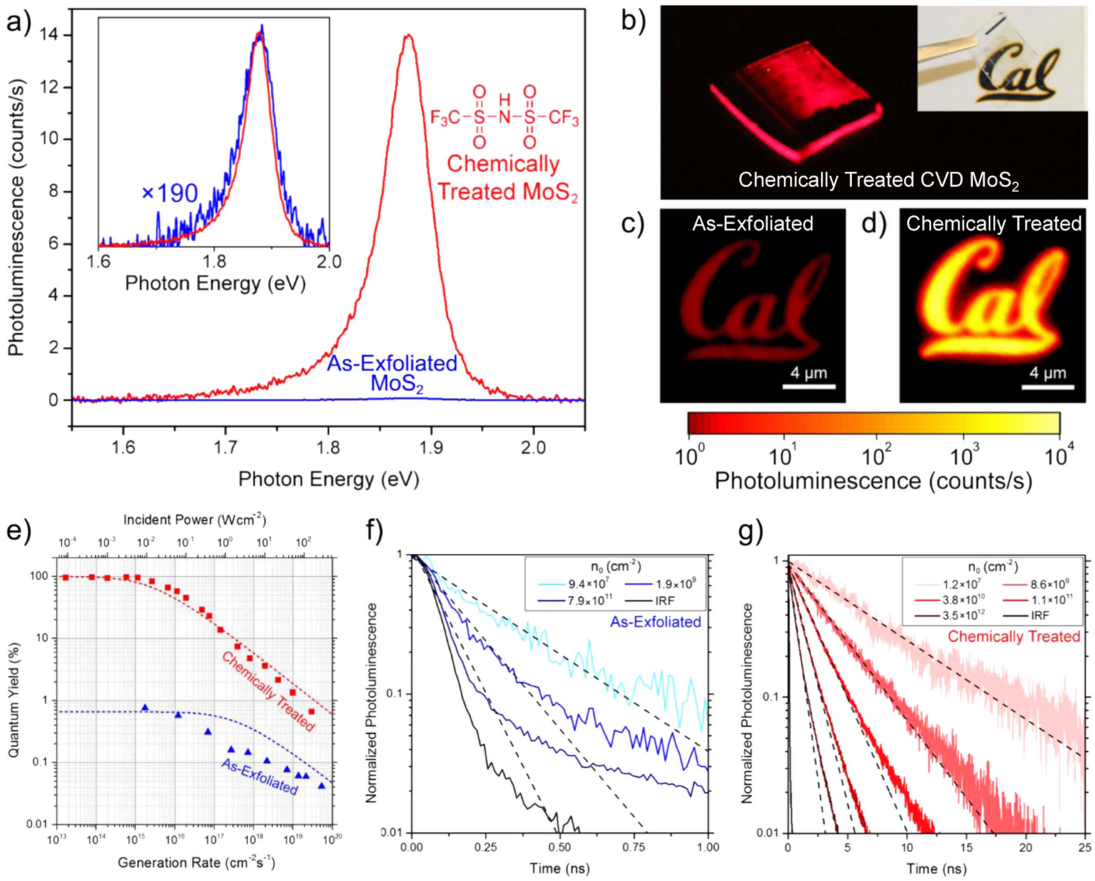

Figure 8. Defect passivation. (a) PL spectra of exfoliated MoS_2 measured at a low incident laser power density (1×10^{-2} W cm^{-2}) before and after superacid treatment; inset shows normalized spectra. Reprinted with permission from [127]. Copyright 2015 AAAS. (b) Photograph of PL from a superacid treated CVD-grown MoS_2 film excited by a UV LED, note that the emission from the edges of the sample occurs due to light trapping within the high-refractive index substrate. Reprinted with permission from [130]. Copyright 2016 American Chemical Society. PL image of an exfoliated MoS_2 sample etched into a shape of the Berkeley logo before (c) and after (d) superacid treatment. (e) Pump-power dependence of the of the PL quantum yield measured before and after superacid treatment. Radiative decay of an as-exfoliated (f) and chemically treated (g) MoS_2 sample measured at multiple initial carrier densities. (c)–(g) Reprinted with permission from [127]. Copyright 2015 AAAS.

this however, defects can also contribute to the interface trap density (D_{it}) in MOSFETs which results in a reduced subthreshold swing as well as limit off-state current in TFETs via trap-assisted tunneling. This is particularly crucial in monolayer TMDs, where there is no distinction between a 'surface' and a 'bulk' defect. Reducing the number of defects, including S vacancies, is thus vital to obtaining high performance TMD devices. Although the results of this work show a dramatic enhancement in the PL QY, the impact on device performance still needs to be evaluated.

4.2. Tuning many-body interactions in 2D semiconductors

Properties of 2D STMDs are strongly influenced by the efficient Coulomb interaction between charge carriers [131]. As a result, the optical response of 2D TMDs is dominated by pronounced resonances from Coulomb-bound electron–hole pairs, or excitons [132, 133]. In addition, the quasiparticle band gap, corresponding to the continuum of unbound electrons and holes and thus particularly relevant for carrier transport, is offset to higher energies in comparison to the bulk by the increase of the so-called self-energy contribution [134, 135], which scales with the strength of the Coulomb interaction. Because of the weak dielectric screening and strong confinement in monolayer TMDs, both the exciton binding energy and the self-energy shift of the quasiparticle band gap are found to be on the order of many 100s of meV [136–140]. In close analogy to the physics of quantum well systems, it is thus possible to modify the properties of 2D materials by deliberate tuning of the many-body interactions [141].

Both excitons and the quasiparticle band gap are highly sensitive to changes in the free carrier concentration (figure 9(a)). These changes can be introduced by optical or electrical injection as well as by chemical doping or local engineering of the band structure. Optical techniques, in particular, typically allow for a large transient increase in the excited carrier population by using intense laser pulses, combined with the ability to monitor the subsequent response of the system on ultra-short timescales. Large

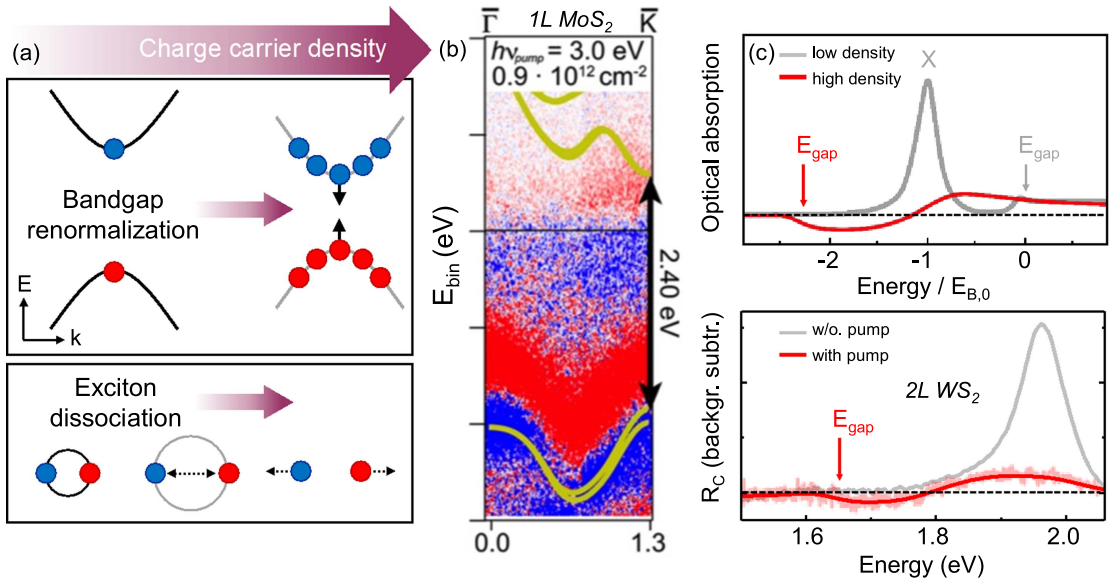

Figure 9. Many-body interactions. (a) Schematic representation of the photo-induced band gap renormalization (upper panel) and exciton dissociation (lower panel). (b) Differential photoemission spectrum of a monolayer MoS_2 plotted in color-scale (red: positive, blue: negative) in momentum space along the $\Gamma - K$ direction after the excitation of the material using a 1.3 mJ cm^{-2} optical pulse with a photon energy of 3.0 eV, directly demonstrating photo-induced renormalization of the band gap. Reprinted with permission from [143]. Copyright 2016 American Chemical Society. (c) Calculated (upper panel) optical absorption spectra of a 2D semiconductor in the spectral region of the band gap for low and high free carrier densities. Corresponding optical response (lower panel, after background subtraction) of a WS_2 bilayer after excitation with 0.8 mJ cm^{-2} optical pulse and photon energy of 2.4 eV. The extracted renormalization of the band gap is on the order of 500 meV; complete absence of the exciton resonance in the high-density spectra is further indicative for the complete dissociation of the excitons. Reprinted with permission from [142]. Copyright 2015 Macmillan Publishers Ltd.

photo-induced renormalization of the band gap in TMD mono- and few-layers has been recently demonstrated using both optical pump–probe [142] and time- and angle-resolved photoemission spectroscopy [143]. The latter technique, in particular, allows for direct imaging of the energy- and momentum-resolved electronic band structure combined with very high temporal resolution. A typical result of this experiment [143] is presented in figure 9(b), where differential photoemission spectrum of a graphene-supported monolayer MoS_2 is plotted in color-scale (red: positive, blue: negative) along $\Gamma - K$ direction in momentum space after the excitation of the material by a 1.3 mJ cm^{-2} laser pulse with a photon energy of 3.0 eV, corresponding to above band gap excitation conditions. The spectrum shows a photo-induced shift in the electronic band structure, corresponding to the overall decrease of the quasiparticle band gap on the order of 200 meV (calculated zero-density band structure is shown by yellow lines for comparison). The maximum transient band gap renormalization is found to be as large as 400 meV, depending on the excitation conditions, and is followed by a fast decay within a few picoseconds [143].

Similar conclusions are drawn by monitoring the optical response of WS_2 mono- and few-layers on fused silica substrates after strong photoexcitation [142]. The upper panel of figure 9(c) shows predicted optical absorption spectra of a 2D semiconductor for low and high free carrier densities, adopted from calculations in [141] for quantum well systems. Optical response of a WS_2 bilayer after the excitation with 0.8 mJ cm^{-2} optical pulse and 2.4 eV photon energy is presented in the lower panel of figure 9(c) (from [142], after subtraction of a linear background). In the low-density regime, the absorption is dominated by the exciton ground state with weaker signatures from excited states merging into the onset of the quasi-particle continuum at higher energies. In contrast to that, the exciton resonance disappears from the spectrum completely at sufficiently high carrier densities due to the exciton dissociation. In addition, a spectrally broad region with negative differential absorption emerges at lower energies. The latter is a signature of the population inversion, allowing for the extraction of the absolute band gap position from the onset of the feature. Thus, an overall band gap renormalization on the order of 500 meV is obtained from the experiment. The subsequent decay of the photo-induced changes and the initial recovery of the exciton resonance occurs on a time-scale of a few picoseconds, similar to the observations from the time-resolved photoemission. It is attributed to the ultra-fast recombination of the charge carries via radiative decay and Auger recombination.

The reported values for band gap renormalization as large as many 100s of meV are understood as the direct consequence of a strong Coulomb interaction, scaling with the zero-density exciton binding energy $E_{B,0}$ (figure 9(c)). Experimentally obtained

renormalization energies reported in [142, 143] also compare well with quantitative theoretical predictions for TMD monolayers [144]. The possibility to induce transient changes of the band gap is further combined with the ability to modulate the exciton binding energy both optically and electrically [145] from the initial values of 100s of meV down to zero.

4.3. Nano-optics of local excitonic phenomena in 2D layered semiconductors

The tightly bound exciton complexes of monolayer STMDs have made a rich collection of 2D excitonic phenomena accessible for nanoscale optoelectronic applications. While the excitonic phenomena in these materials is reminiscent of that in traditional 2D semiconductor quantum wells, reduced dielectric screening of the Coulombic interactions between excited state electrons and holes yields much larger binding energies that are sufficient to stabilize the bound states at room temperature and ambient conditions. With Bohr radii that are on order of a nanometer [146], these excitations are nanoscale entities and are locally influenced on nanometer length scales by strain [147], electrostatic fields [148], molecular adsorbates [149, 150], and structural defects such as grain boundaries [60]. In addition to being potential sources of disorder, these effects can be utilized to control and manipulate local optoelectronic functionality. Thus, developing a thorough understanding of nanoscale excitonic properties is key to enabling unprecedented exciton-based devices in these materials.

Conventional optical techniques are inherently limited by the diffraction limit (a few hundred nanometers across the visible spectrum) and are unable to directly resolve excitonic phenomena at critical optoelectronic length scales (i.e., the exciton diffusion length, inter-defect spacing, etc). Nanoscale plasmonic antennas offer the means to bridge this crucial resolution gap by confining optical fields and amplifying light–matter interactions in sub-diffraction nanoscale volumes that are commonly referred to as 'hot spots.' Combining such antennas with SPM techniques is the basis of nano-optical imaging (and spectroscopy), where such hot spots are scanned over a sample and mediate optical excitation and/or collection at spatial resolutions that can be over 10× better than that of the conventional diffraction limit [151]. Emphasis has thus far been placed on unraveling the local effects of grain boundaries [152–154], strain [154], nanoscale variations of the interplay between various exciton states [152, 154–156], and possible charge transfer between a metallic nano-optical probe and the 2D semiconductor [155]. Strikingly, a few of these studies have also managed to perform nanoscale tip-enhanced Raman scattering (TERS) to correlate local strain and structure to observed optoelectronic variations [154, 155].

One nano-optical imaging technique utilizes the adaptation of the so-called 'Campanile' nano-optical probe [157] to image exciton relaxation in monolayer MoS_2 [152, 158], as summarized in figure 10. The unique structure of the Campanile probe simultaneously confines optical excitation and collection of the luminescence to a nanoscale gap at the apex of an optical fiber probe, effectively eliminating any far-field background while retaining the spectral information of the collected emission. In addition, the confined optical fields of the Campanile probe are polarized predominantly in the plane of the sample, parallel to the in-plane transition dipole moments of the direct band gap excitons. Using the Campanile probe to image local variations of the intensity and energy of the excitonic PL, it was found that CVD-grown monolayer MoS_2 has a peripheral 300 nm wide edge (figure 10(b)) that is distinct from the interior and exhibits spectral signatures analogous to those of disordered semiconductor systems such as quantum dot solids and conjugated polymers (figure 10(c)). Notably, a similar edge region was found in CVD-grown monolayer WSe_2 [154]. The synthetic origins of such edge regions may stem from the precise nature in how the growth process is terminated and their existence provides new insight into possible origins of poor carrier mobility in some samples as well as edge-related photophysics and catalytic activity. Within the interior region, in contrast to the disordered edge, nanoscale variations were observed between the relative populations of excitons and trions (singly charged excitons), which provide initial evidence of spatial fluctuations of the local carrier density in analogy to 'charge puddles' in graphene [159]. It was also found that the quenching extends to distances that average ∼130 nm from the grain boundary, as shown in figures 10(d) and (e). These measured distances are not resolution-limited and thus offer an initial quantification of the spatial extent of excited state quenching by the grain boundary, which is significantly larger than its corresponding structural size [60] and likely enhanced by a combination of factors, such as exciton diffusion [160, 161] and local strain. However, the precise origins and nature behind this quenching effect are still active topics of research. In CVD-grown monolayer WSe_2 samples, the spatial extent of exciton quenching was found to be smaller (∼25 nm) but commensurate with initial estimates of the exciton diffusion length derived from carrier mobility [154]. Furthermore, in other CVD-grown MoS_2 monolayers, line defects and grain boundaries were found to exhibit less PL due to physical damage and missing material [153]. Thus far, only exciton quenching has been investigated with nano-optical imaging techniques, yet grain boundaries (and edges) can also locally enhance the PL by surprising amounts via mechanisms that are also not yet fully understood [60].

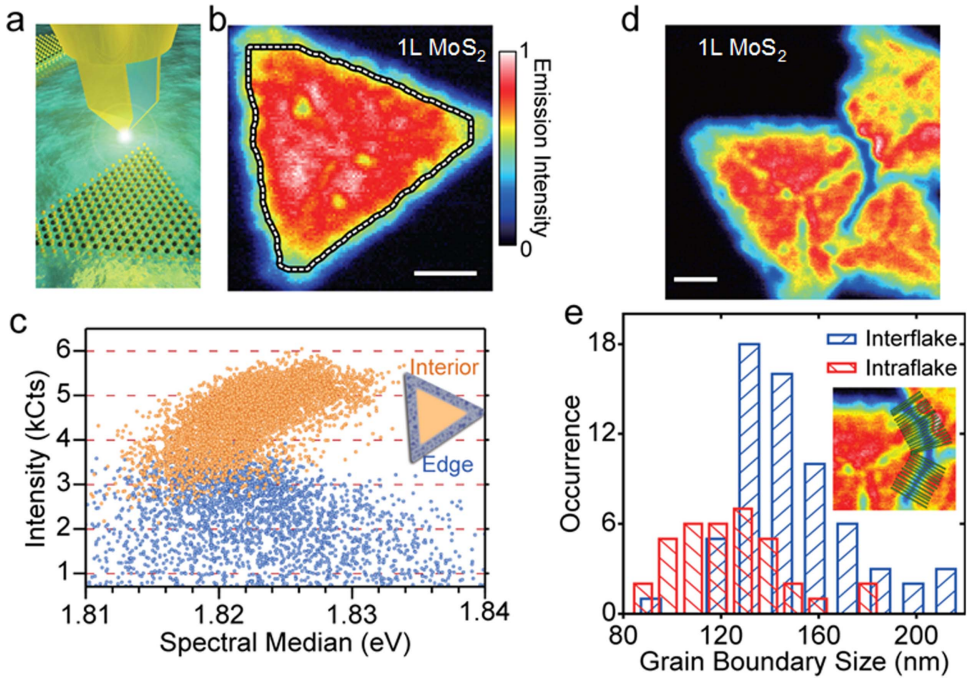

Figure 10. Nano-optical imaging and spectroscopy. (a) Schematic visualization of the nano-optical imaging and spectroscopy technique. (b) Nano-PL map of excitonic PL intensity of a single flake of monolayer MoS_2 with the approximate boundary between the interior and 300 nm wide disordered edge region marked by the dashed line. Scale bar, 1 μm. (c) The distinct behavior between the edge and interior regions of the correlation between the PL intensity and energy uncovered the existence of the edge region and demonstrate the value of retaining the spectral information in nano-optical imaging techniques. (d) Nano-PL map of the exciton quenching at grain boundaries in monolayer MoS_2. Scale bar, 1 μm. (e) The size of the quenching regions were quantified at various parts of the grain boundaries (inset) to obtain the average spatial extent of ~130 nm for the quenching effect. (a)–(e) Reprinted with permission from [152]. Copyright 2015 Macmillan Publishers Ltd.

4.4. Generation and electric control of spin-coupled valley current in WSe_2

Generation and manipulation of a spin current is one of the most critical steps in developing semiconductor spintronic applications [162–164]. Due to the large separation of the two inequivalent valleys in ***k***-space and the resulting suppression of intervalley scattering, the valley index can be used in analogy to the spin in spintronics, opening a new research direction on spin-valley locking and 'valleytronics' [165–167]. Such a valley polarization achieved via valley-selective circular dichroism has been demonstrated theoretically and experimentally in TMDs that lack inversion symmetry (in monolayer cases or under an electric field) [21, 165, 166, 168–173]. However, a spin/valley current caused by such a valley polarization has yet to be observed and its electric-field control has not been studied.

Normally, in a 2D electronic system (2DES) with spin degeneracy lifted, illumination with circularly polarized light can result in a non-uniform distribution of photo-excited carriers in ***k***-space following optical selection rules and energy/momentum conservation, leading to a spin current [174–176]. Referred to as the circular photogalvanic effect (CPGE) [177–180], the fingerprint of such a spin photocurrent is the dependence on the helicity of the light. The absorption of circularly polarized light results in optical spin orientation by transferring the angular momentum of photons to electrons. Thus, the non-equilibrium spin polarization of electrons forms a spin current with the electron motion in the 2DES plane, which is of practical significance for spin current control in TMDs.

Recently, a spin-coupled valley photocurrent was demonstrated in WSe_2, where the direction and magnitude depended on the degree of circular polarization of the incident light and could be continuously controlled by an external electric field [181]. Single crystal flakes of WSe_2 were fabricated into EDLTs which have the capability to generate a large interfacial electric field to control electronic phases of solids [99, 182–187] and modulate the spin texture in 2DESs [21, 188, 189]. Figure 11(a) is a schematic diagram of a WSe_2 EDLT gated with ionic gel [190]. Owing to the band bending caused by the chemical potential realignment between the gel and the WSe_2, there is an electron accumulation with low carrier density at the gel/WSe_2 interface (figure 11(a)). This large local interface electric field applied perpendicularly to the 2D plane can effectively modify interfacial band bending and the degree of inversion asymmetry. CPGE measurements induced by circularly polarized light on WSe_2 were used to detect a non-uniform distribution of photo-excited carriers and the generated spin current in WSe_2, with the configuration shown in figure 11(a). The energy of the laser used (1.17 eV, 1064 nm) is below the indirect band gap of WSe_2; thus,

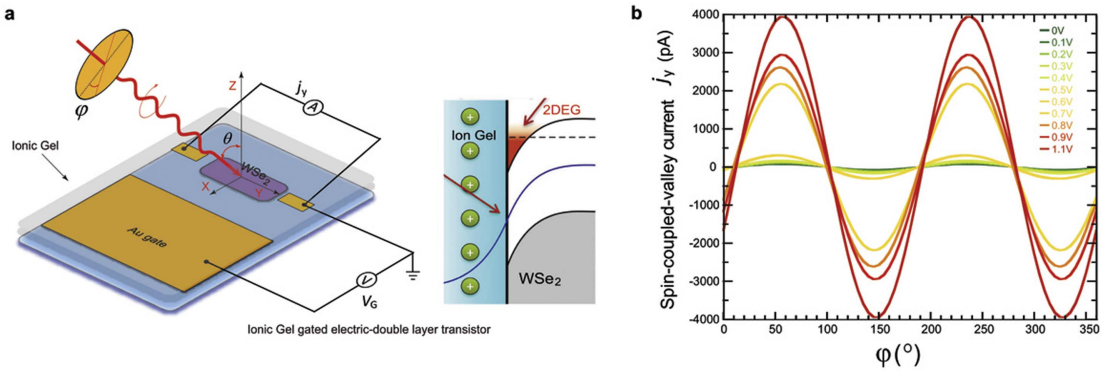

Figure 11. Spin-coupled valley current in WSe_2. (a) Schematic diagram (left panel) and surface band alignment (right panel) of WSe_2 an EDLT with ion gel as the gate dielectric. (b) The electric field modulation of the photogalvanic current j_{CPGE} in WSe_2 transistors at various gate voltages. φ is the angle of the quarter wave plate, reflecting the helicity of the circularly polarized light. (a and b) Reprinted with permission from [181]. Copyright 2014 Macmillan Publishers Ltd.

the photocurrent generated originated from the surface accumulation layer and not from bulk electron–hole excitations.

The CPGE phenomenon and the spin photocurrent are highly sensitive to subtle details of the electronic band structure in the 2D systems with lifted spin degeneracy, and thus even a small band splitting may result in measurable effects. Therefore, the modification of the degree of inversion asymmetry with an external perpendicular electric field provides a simple way to control the CPGE photocurrent. Figure 11(b) shows the light polarization dependent photocurrent obtained in a WSe_2 EDLT at various external biases (V_G = 0–1.1 V). The magnitude of the electric current for all biases was related to the radiation helicity and the photogalvanic current j_{CPGE} (red curves) followed $\sin(2\varphi)$. Importantly, j_{CPGE} dramatically increased with V_G from tens of pA to thousands of pA, unambiguously indicating an electric modulation of the CPGE photocurrent.

The photocurrents generated by optical pumping discussed above were realized at room temperature with the CPGE in accumulation layers on bulk WSe_2 surfaces [181]. Considering that all of the phenomena happens at the surface accumulation layer of WSe_2, which is where the surface inversion symmetry occurs, similar CPGE phenomenon has also been observed in monolayer MoS_2 [191].

4.5. Ultrafast structural response in 2D materials

While the optoelectronic properties of mono- to few-layer TMDs have received extensive interest over the last decade, these optoelectronic techniques can also be used to probe structural properties and resulting functionality of 2D materials, which is far less studied. This functionality intrinsically involves the material's dynamic structural evolution, extending across a range of length- and time-scales from local vibrations (both in-plane and interlayer) as probed in the frequency domain by Raman scattering approaches [192, 193] or in the time-domain by pump–probe spectroscopy [194–196], to longer length-scale structural deformations. From the earliest days of research into graphene, speculation arose regarding the role of the Mermin–Wagner theorem [197, 198] in determining its mechanical properties, potentially associated with dynamic rippling and buckling responses [199–201]. These mechanical deformations in turn can strongly influence corresponding transport properties [202, 203]. From a more general perspective, many important electronic and optoelectronic properties are closely intertwined with structural processes through scattering mechanisms arising from electron–phonon interactions. Numerous optical studies have investigated the ultrafast time-scale relaxation processes exhibited by photo-excited hot carriers as they couple to the lattice on picosecond and sub-picosecond time-scales [204–207].

In contrast, direct studies probing the atomic-scale response, e.g., what the atoms are doing, are just beginning to be developed. Nonlinear optical measurements probing the time-dependence of the second order susceptibility can provide information into changes in the crystallographic symmetry of monolayer TMDs, taking advantage of the breaking of inversion symmetry in the monolayer limit [208]. However, both electronic and structural degrees of freedom contribute to this susceptibility, thus making the extraction of the ultrafast atomic-scale response difficult to obtain [209]. Therefore, time-resolved x-ray or electron scattering has been utilized to directly probe the ultrafast structural response of monolayer and few-layer 2D materials. These measurements are typically carried out in a pump–probe scheme in which an optical trigger initiates some structural response with the dynamic structure visualized through measurement of a time-dependent scattering pattern. In comparison to x-rays, the electron scattering cross-section is many orders of magnitude larger. Recent studies have therefore focused on electron diffraction techniques when probing monolayer samples [210, 211].

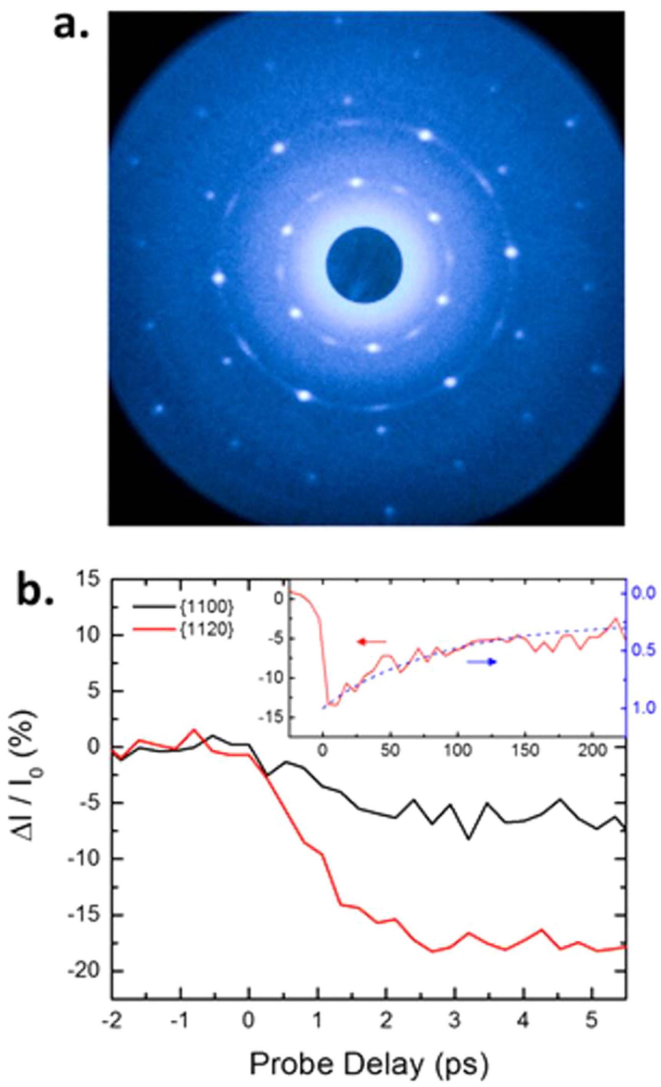

Figure 12. Ultrafast structural response. (a) Femtosecond electron diffraction snapshot from monolayer MoS_2 (2H-phase). (b) Time-resolved changes in diffracted intensity following above gap photoexcitation for two lowest order diffraction peaks. Inset shows long time dynamics. (a) and (b) Reprinted with permission from [212]. Copyright 2015 American Chemical Society.

The first pump–probe transmission electron diffraction study of the ultrafast structural response of monolayer (2H-phase) MoS_2 single domains has recently been reported [212]. In these studies, 400 nm above gap, femtosecond optical excitation was used to generate photo-excited carriers at high carrier densities ($\sim 10^{21}$/cc) with the atomic-scale response probed by recording changes in the intensities, position in reciprocal space, and size of different diffraction orders. Figure 12(a) shows typical diffraction patterns recorded, corresponding to an average of approximately 1000 shots, using MeV-scale electron bunches with 15 fC charge and pulse duration ~300 fs at 120 Hz repetition rate [213]. These measurements showed rapid decreases in the intensities of Bragg peaks (figure 12(b)) associated with an increase in the mean square displacements of the Mo and S atoms within the monolayer, as reflected in a time-dependent Debye–Waller response [214]. This corresponds to a direct measurement of electron–phonon coupling time-scales, with observed response occurring with a time-constant of ~1.7 ps. More interestingly, ultrafast changes in the position of the diffraction peaks (as measured by the momentum transfer, Q), and in the width of the diffraction peaks are also observed. In analogy with recent TEM studies of static rippling in graphene as reflected in the width of the diffraction spot [201], this response was interpreted as reflective of a dynamic rippling response in the out-of-plane direction. This effect arises from the tilting of the crystal truncation rods associated with the monolayer as it deforms, thus forming an effective cone in reciprocal space. Where this cone intersects the Ewald sphere then determines the magnitude of the broadening response. Associated with this rippling are corresponding strain fields that are also directly measured as subtle shifts in the position of the diffraction peaks, occurring on few picosecond time-scales. The ultrafast turn-on of these effects are indicative of short length-scale motions, with an upper limit determined by the

product of the in-plane sound velocity and the observed time-scale, corresponding to length-scales <10 nm in size. Also recorded in these measurements are the time-scales for cooling of the sample into the substrate from which the thermal interfacial resistances may be directly extracted.

4.6. Ultrafast charge transfer in vdW heterostructures

Interlayer charge transfer in vdW heterostructures is an important process for implementing these materials into electronic and optoelectronic devices. To study charge transfer between the two monolayer TMDs in a heterostructure, a laser pulse with a duration of ~100 fs (pump) can be tuned to the optical band gap of the first TMD (TMD1). This pulse selectively excites the TMD1 layer, which is assumed to have a smaller band gap than TMD2. Most TMD heterostructures form type-II band alignments, where the conduction band minimum (CBM) and the valence band maximum (VBM) are located in different layers [215]. If the CBM and VBM are in TMD2 and TMD1 layers, respectively, the excited electrons are expected to transfer to TMD2 while the holes remain in TMD1. If the band alignment is reversed, holes, instead of electrons, will transfer to TMD2. The charge transfer was monitored by using a probe pulse that is instead tuned to the optical band gap of TMD2 [216–219]. Either differential transmission [216, 218] or differential reflection [217, 219] of the probe was measured. Under typical conditions, these quantities are proportional to the density of carriers in TMD2. Hence, by measuring these quantities as a function of the probe delay, defined as the delay of the arriving time of the probe at the sample with respect to the pump pulse, one can monitor the build-up of the TMD2 carrier density as a result of the charge transfer process.

Time-resolved studies of interlayer charge transfer between WS_2 and MoS_2 have shown that the hole density in a WS_2 layer after excitation into MoS_2 reaches a peak on a time scale limited by the instrumental response time. A careful analysis of the time-resolved data showed that the charge transfer time is shorter than 50 fs [216]. Similarly, fast transfer times of electrons in various TMD heterostructures were reported for $MoSe_2$ to MoS_2 [217], WSe_2 to MoS_2 [218], and WSe_2 to WS_2 [219]. The charge transfer from a WS_2 monolayer to graphene was also found to be sub-100 fs [220]. These results are consistent despite different materials used to form the heterostructures, different sample temperatures (77 K [216] or room temperature [217–219]), and different sample fabrication techniques (mechanical exfoliation followed by transfer [216–218] or CVD [219]).

Although this efficient and ultrafast charge transfer appears to be experimentally established, a full understanding on its microscopic mechanism is still under development. There are two proposed mechanisms that could be responsible for the efficient charge transfer [221]. First, resonant electron transfer from CBM of TMD1 to higher energy states in the conduction band of TMD2 would allow the sampling of a large range of parallel momentum vectors. Second, the localization of the electrons in real space due to the large binding energy of the charge-transfer excitons results in a large uncertainty of the parallel momentum vectors of the electron, thus facilitating momentum matching in the transfer process. Theoretical studies have also revealed that quantum coherence at the interface enables efficient charge transfer [222]. The quantum coherence is facilitated by the delocalization of the charge-transfer exciton states, and is sufficient to overcome the Coulomb potential. Calculations performed using $MoSe_2$–MoS_2 as an example are in excellent agreement with experimental results [217], and indicate that long coherence leads to fast charge transfer. Additionally, it has been shown that the coupling between the hole states in MoS_2 and WS_2 can be significantly enhanced by the Coulomb potential resulting from initially transferred holes [223].

5. 2D electronics

5.1. Tunneling devices from TMD heterostructures

The dangling-bond-free surfaces of 2D TMDs (although practically defects exist) and sharp interfaces enable strain-free vdW heterostructures with reduced lattice matching constraints and sharp band edges. These properties of TMD heterostructures are essential for fabricating novel devices such as tunnel diodes and steep switching of tunneling FETs (TFETs).

Several works have investigated graphene-based vdW heterostructures, but the OFF-state leakage current is typically large due to the lack of an intrinsic band gap in graphene. TMDs exhibit a large band gap and have ignited significant research in the design of 2D–2D TMD heterojunction devices. The demonstration of a 2D–2D MoS_2–WSe_2 tunable gated tunnel diode (figures 13(a)–(g)) [224] highlights the merit of using TMDs. The cross-sectional TEM image (figures 13(b) and (c)) of the device shows the 2D–2D heterojunction with an atomically sharp interface between MoS_2 and WSe_2. Using the two gates, the MoS_2 and WSe_2 layers are electrostatically doped n-type and p-type respectively, thus allowing for a tunable diode. Figure 13(f) shows the electrical characteristics of the tunable diode as a function of the applied gate voltages. The same device can operate as a tunnel diode, a Zener diode with negative differential resistance, or a normal forward diode by simply changing the two gate voltages, which effectively tune the band alignment at the hetero-interface. Other recent works have also demonstrated 2D–2D heterostructure-based tunnel diodes with promising performance using CVD-grown MoS_2–WSe_2 [77] and black phosphorus-

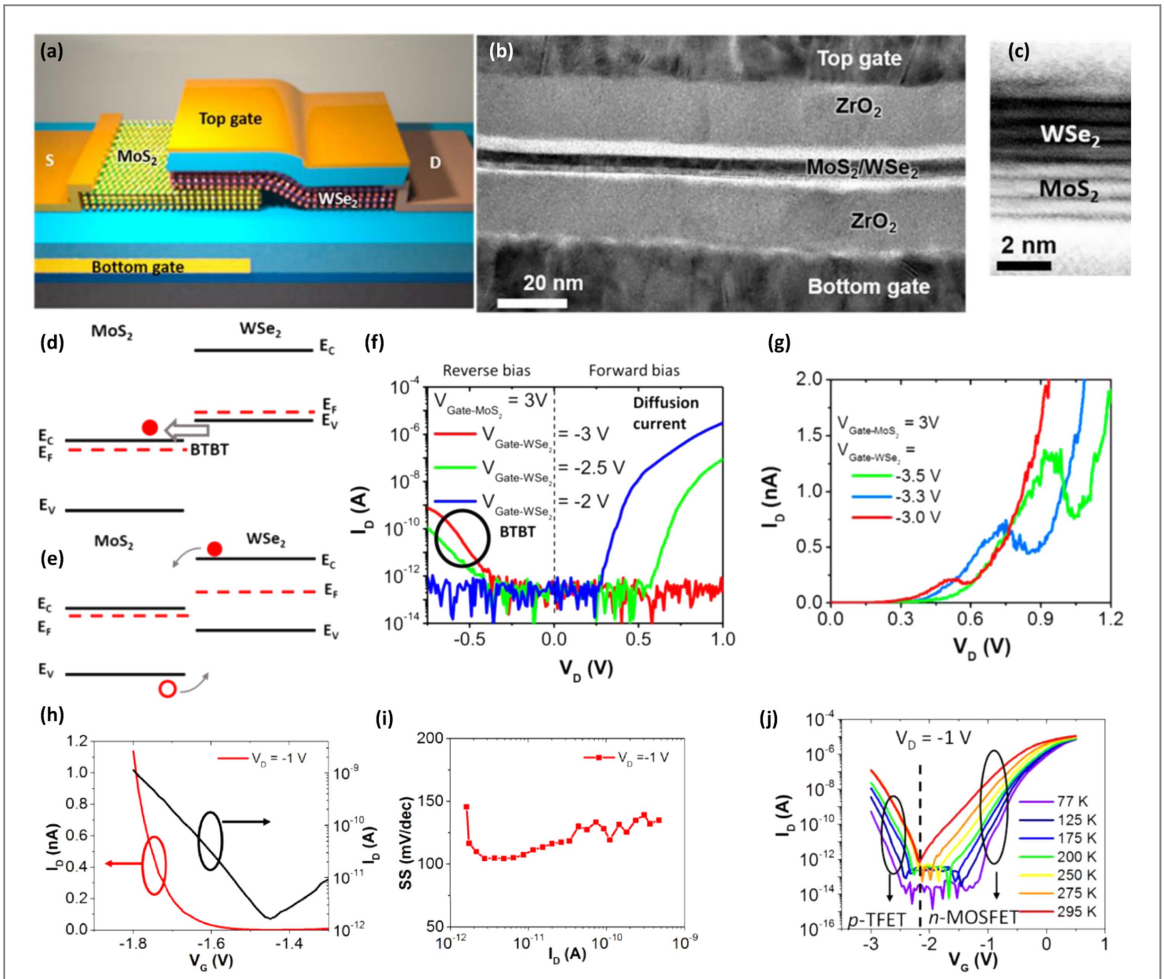

Figure 13. Tunneling transistors. (a) Schematic of vdW heterostructure MoS_2–WSe_2 tunable gated diode. (b)–(c) TEM image of device shown in (a). (d) Energy band diagram for Zener diode operation at large positive MoS_2 gate bias and large negative WSe_2 gate bias. (e) Energy band diagram for normal diode operation at positive WSe_2 gate bias. (f) I_D–V_D characteristics for the tunable diode as a function of gate biases. (g) Tunnel diode operation of the MoS_2–WSe_2 heterostructure diode showing negative differential resistance region. (a)–(g) Reprinted with permission from [224]. Copyright 2015 American Chemical Society. (h) I_D–V_G characteristics for WSe_2–$SnSe_2$ TFET. (i) Subthreshold slope for data in (h). (j) Temperature dependent I_D–V_G characteristics for WSe_2–$SnSe_2$ TFET showing the operation of the device as a MOSFET or TFET as a function of gate biases. (h)–(j) Reprinted with permission from [226]. Copyright 2016 American Institute of Physics.

$SnSe_2$ [225]. More recently, a $SnSe_2$–WSe_2 heterostructure was used to demonstrate a 2D–2D heterojunction TFET [226]. The I_D– V_G characteristics (figure 13(h)) show a minimum subthreshold slope of ~100 mV/decade (figure 13(i)). In another TFET device (figure 13(j)), the I_D– V_G characteristics show that it can be operated as a TFET or a MOSFET based on the gate biases. The temperature independence of the p-branch is indicative of band-to-band-tunneling mechanism for the TFET, whereas the temperature dependence of the n-branch depicts thermionic emission, characteristic of a MOSFET.

In addition to 2D–2D heterostructures, TMDs offer the ability to make versatile 2D–3D heterostructures. Previous works involving InAs–WSe_2 diodes with an ideality factor of ~1 demonstrate the ability to achieve high-quality interfaces between materials with distinct crystal structures [227]. Most recently, a sub-60 mV/decade TFET was demonstrated using Ge–MoS_2 heterostructures [228], further showing the uniqueness of vertical heterostructures using TMDs for novel device applications.

5.2. Passivation of phosphorene MOSFETs

Since 2D materials are sensitive to the environment, their protection from degradation must be studied before high performance devices can be realized. Significant progress has recently been made regarding the passivation of 2D materials, particularly with respect to the material phosphorene. Since 2014, there has been an explosive interest in phosphorene, a monolayer of black phosphorus, as a unique 2D material for electronics, optoelectronics, and other applications. This is mainly because phosphorene has both an intrinsic and sizable band gap (unlike graphene), as well as a high carrier mobility (unlike most STMDs) [229]. In less than two years, more than 700 papers have been published on phosphorene. Due to phosphorene's air sensitivity, the most significant breakthrough has been the successful passivation against environmental degradation such that the

Table 1. Passivated phosphorene MOSFETs.

University	Passivation	Ambient stability	Thermal stability	Reference
KIST	Al_2O_3	2 mo		[231]
Northwestern	AlO_x	2 wk		[232]
Lehigh	Al_2O_3	3 mo	−50 °C to 150 °C	[230]
UT Austin	AL_2O_3	3 mo		[233]
Michigan State	AL_2O_3	1 wk		[234]
UC Riverside	hBN	2 wk		[235]
Singapore	hBN	2 mo	−263 °C to 25 °C	[236]
HKUST	hBN	1 wk		[237]
Case Western	hBN	70 h		[238]
Manchester	hBN	Several mo		[239]

unique performance of phosphorene MOSFETs could be demonstrated [230].

Due to a permanent out-of-plane dipole moment, the phosphorene surface is hydrophilic and easily oxidized, especially in humid environments and under illumination. It was found that within approximately an hour of ambient exposure, the phosphorene surface became measurably rougher by AFM and water droplets were observable by optical microscopy. Thus, although phosphorene is sufficiently stable to allow preliminary MOSFETs to be quickly fabricated and characterized, effective surface passivation is of paramount importance in order to achieve long-term stability. Nevertheless, unpassivated MOSFETs typically exhibit carrier mobilities on the order of 10^2 cm^2 V^{-1} s^{-1}, current capacities on the order of 10^2 mA mm^{-1}, and ON/OFF current ratios on the order of 10^4. Their subthreshold slope was on the order of 1 V/decade with a back gate and an insulator thickness on the order of 100 nm.

To passivate the phosphorene surface, atomic-layer deposited aluminum oxide (Al_2O_3) [230–234] and exfoliated hBN [235–239] have been used to demonstrate stable phosphorene FETs under ambient conditions up to several months (see table 1). Thermal stability of top-gated phosphorene FETs was also demonstrated from −263 °C to 150 °C [230, 236], thus covering the temperature range of most applications. The wide range of temperature stability implied that the source and drain contacts were ohmic and the charge carriers did not freeze out. The ON current of an Al_2O_3-passivated phosphorene FET was stable between −50 °C and 150 °C with an activation energy on the order of 0.01 eV. The mechanical stability of Al_2O_3-passivated phosphorene MOSFETs was demonstrated with 5000 strain cycles [240], thus showing their potential in flexible electronics. In addition to Al_2O_3, phosphorene passivation with hafnium oxide (HfO_2) has been reported [241, 242]. It should be noted that besides the success stories, there have also been reports of passivation failures with Al_2O_3 and SiO_2 [243, 244]. Therefore, well established and reproducible protocols need to be developed in the near future.

The hBN/phosphorene/hBN sandwich, although uncommon in MOSFET fabrication, appeared to be of very high quality when carefully assembled [239]. The stack could then be annealed up to 500 °C (black phosphorus would transform to red phosphorus at 550 °C) for stable carrier mobility on the order of 10^3 cm^2 V^{-1} s^{-1} and ON/OFF ratio on the order of 10^5 [237]. The high mobility, approaching that of bulk black phosphorus and exceeding that of single crystalline silicon, could be attributed to the reduction of interface roughness scattering resulted by atomically flat hBN and the reduction of interface state density by the high-temperature annealing, as shown by the elimination of hysteresis. With proper passivation, top-gated phosphorene MOSFETs on a high-resistivity substrate have been shown to operate at microwave frequencies [241, 245, 246].

5.3. Phase engineering for low resistance contacts

Phase engineering is another approach that can be utilized to study 2D materials for integration to device technologies. Phase engineering, or accessing targeted polymorphs (e.g., 1T- versus 2H–MoS_2), is important because of the significant impact that differences in coordination geometry and layer-stacking sequence can have on the properties of these materials [247]. For example, 2H–MoS_2 is semiconducting while the 1T-polymorph is metallic [88, 247, 248]. Although the perfect 1T-phase is less stable than the 2H-phase, a slightly distorted 1T structure—1T′-phase is a more stable structure. Nanosheets of MoS_2 produced via chemical exfoliation are typically a mixture of 2H- and 1T′- phases [249], and these can coexist seamlessly in the same atomic plane (figure 14(a)). Considering the drastically different properties of the two phases, phase engineering has become an effective way to enhance the performance of MoS_2 nanosheets in electronics and catalytic applications. For example, a Schottky barrier formed between metal contacts and MoS_2 channels has long been a limiting factor for the transport characteristics of FETs [36, 250–252]. Recently, it was found that the 1T′-phase formed by local conversion of a 2H-nanosheet could serve as a contact superior to other metals. Owing to the sharpness of the 2H–1T′ interface, the contact

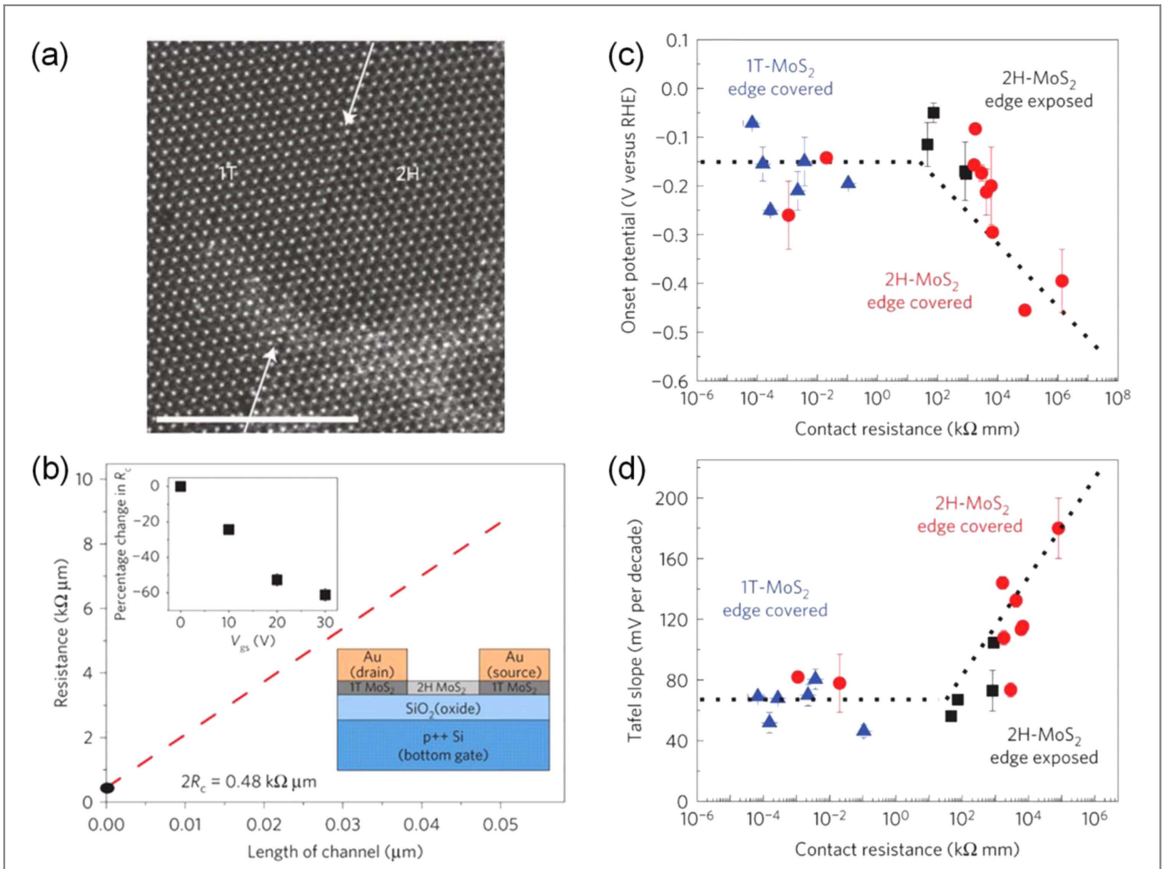

Figure 14. Phase engineering of TMDs. (a) HRTEM image showing the 1T′–2H phase boundary in monolayer MoS_2. The scale bar is 5 nm. (b) Contact resistance of 1T′ contacts at zero and (inset) non-zero gate bias. (a) and (b) Reprinted with permission from [253]. Copyright 2014 Macmillan Publishers Ltd (c) Onset potential and (d) Tafel slope of MoS_2-based electrochemical microcells as a function of contact resistance. (c) and (d) Reprinted with permission from [255]. Copyright 2016 Macmillan Publishers Ltd.

resistance is dramatically reduced (figure 14(b)). Utilizing the metallic 1T′-phase as contacts also benefits the devices' reproducibility [253].

Contact resistance also plays a key role in MoS_2-based catalytic applications. Previously, the basal plane of 2H–MoS_2 has been viewed as largely inert towards hydrogen evolution reactions whereas edges and the 1T′-phase were thought to be more catalytically active [254]. In a recent work by Chhowalla's group, it was demonstrated that the 2H basal plane does contain active sites, possibly at defects such as sulfur vacancies, but does not act as an effective catalyst unless the contact resistance can be sufficiently reduced to facilitate charge injection. When phase-engineered 1T′–2H low-resistance contacts are used, the intrinsic catalytic performance of the 2H-phase can be accessed and it is found to be comparable to that of the 1T′-phase or the domain edges (figures 14(c) and (d)) [255].

5.4. Impacts of dielectrics and contacts on 2D electronics

Modulation of properties due to environmental effects must be considered when it comes to nanoelectronic devices with atomically thin channels, where the entire material is simply a surface. Mobility enhancement is observed for ultra-thin channels encapsulated in high-k dielectrics [256, 257] while mobility degradation is observed in graphene FETs due to the presence of process residues [258, 259]. This section focuses on reviewing two key integration challenges for 2D materials: (1) depositing ultra-thin, uniform high-k dielectric gate insulators and (2) realizing low-resistance contacts.

Atomic layer deposition (ALD) allows a precise thickness control of ultra-thin metal oxide films via self-limiting growth cycles achieved by alternating metal and oxygen precursor exposures. Since the precursor reaction chemistry is well established, the initial nucleation step, which requires reactions with the substrate, is key to achieving uniform and homogeneous films. Unfortunately, the lack of dangling bonds on the basal plane of vdW solids limits these reactions with the surface. In recent years, there has been considerable progress made to achieve scalable and uniform high-k dielectrics on TMDs. Recent studies have demonstrated 3 nm pin-hole free ALD of both Al_2O_3 and HfO_2 carried out at 200 °C on MoS_2, achieved by pretreating the sample with UV–ozone [260, 261]. The MoS_2 surface was exposed to atmospheric pressure of O_2 while being illuminated by a mercury lamp positioned <1 cm from the sample surface. This resulted in the adsorption of oxygen species on the MoS_2 surface via S–O bonding without any evidence of Mo–S

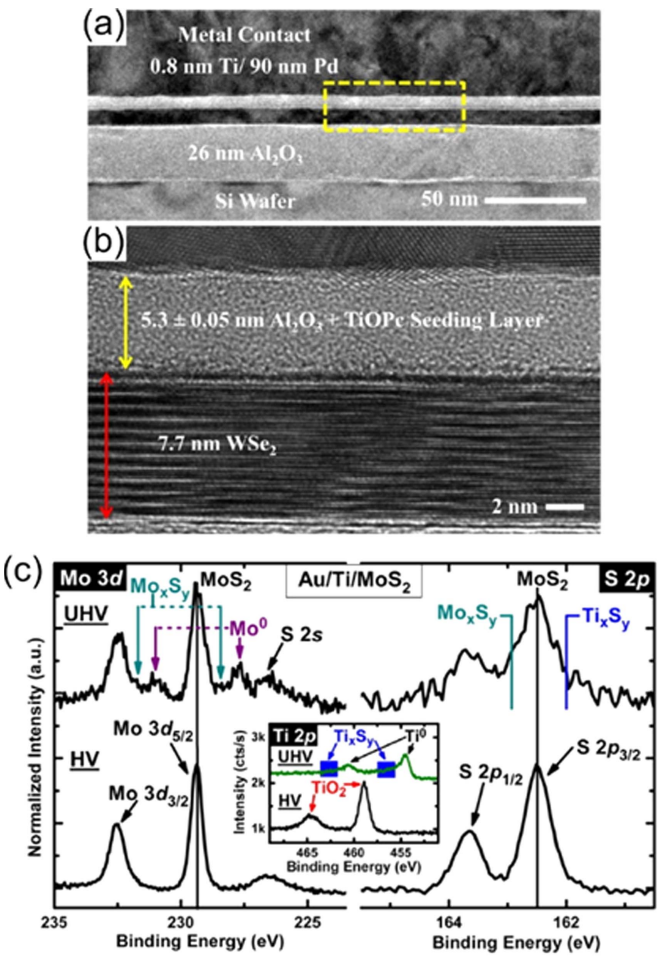

Figure 15. Dielectrics and contacts on 2D TMDs. (a) Low magnification and (b) high magnification cross-sectional TEM images of Pd/Ti/Al_2O_3/TiOPc/WSe_2/Al_2O_3/Si. The TEM images indicate that using a seeding layer of TiOPc results in full coverage of WSe_2 channel with uniform and pinhole-free Al_2O_3 oxide. (a) and (b) Reprinted with permission from [262]. Copyright 2016 American Chemical Society. (c) Mo 3d, S 2p, and Ti 2p (inset) core-level spectra for Au/Ti/MoS_2 stacks generated in HV and UHV. Both are formed by sequential depositions without breaking vacuum. After the deposition of the final Au layer, both samples are exposed to air for 20 min prior to XPS analysis. The Ti deposited in HV deposits as TiO_2 and does not react with the MoS_2. The Ti deposited in UHV deposits as metallic Ti and reacts with the MoS_2. Reprinted with permission from [271]. Copyright 2016 American Chemical Society.

bond scission. The oxygen remained stable on the surface up to 200 °C, which determines the maximum ALD temperature. While the UV–ozone process shows promise for MoS_2-based applications, it does not appear to be readily transferable to other TMD materials. Both $MoSe_2$ and WSe_2 substrates showed evidence of metal oxidation during the UV–ozone pretreatment [261]. An alternative approach to achieving conformal Al_2O_3 utilizes a titanyl phthalocyanine (TiOPc) seed-layer prior to ALD [262]. In this context, TiOPc was deposited on WSe_2 using organic molecular beam epitaxy, which permitted the conformal deposition of 10 nm Al_2O_3 at 120 °C. Afterwards, FETs were demonstrated with an equivalent oxide thickness of 3.0 nm and a leakage current of 0.046 pA μm^{-2}. The HRTEM of the resultant structure is shown in figures 15(a) and (b). Similar to the UV–ozone method, the maximum ALD temperature is predicted to be 200 °C due to the desorption of TiOPc from WSe_2 at that temperature. This process has the advantage of potentially being transferable to all TMDs; however, the authors noted that the desorption temperature from WSe_2 was 100 °C lower than from highly ordered pyrolytic graphite, suggesting that the maximum ALD temperature may be strongly dependent on the TMD substrate.

The realization of low resistance contacts is the second integration challenge for 2D materials. As discussed in section 5.3, a measurable Schottky barrier is observed for all elemental metals in contact with MoS_2 and the Fermi level appears to be pinned below the conduction band of MoS_2 [263]. It has been proposed that, upon metal interactions with the S, gap states are induced in the Mo d-orbital by the weakening of the S–Mo interlayer bonding [264]. Additionally, a metal work function modification could be induced by an interface dipole formed during charge redistribution and S vacancies have been predicted to introduce transition states in the upper half of the gap [265]. A practical consideration in the formation of contacts to

TMDs is the details of the interface reactions. It has been known for some time that many metals react with MoS_2 to form metal sulfides, MoS_x, and even Mo metal at the interface [266–268]. A recent review of the thermodynamic predictions for metal–MoS_2 interfaces shows that a large number of metals may react with MoS_2 [269]. Complicating the matter further, it has also been noted that the processing conditions can play a role in determining the contact resistance. The contact resistance of Au contacts deposited in ultra-high vacuum(UHV, 10^{-9} Torr) has been shown to be lower than that of Au contacts deposited in high vacuum (HV, 10^{-6} Torr) [270]. However, Ti contacts deposited in HV have been shown to result in higher contact resistance than Ni contacts deposited in UHV. Additionally, it has been demonstrated that in the case of Ti depositions, the presence of oxygen during HV deposition can result in the deposition of TiO_2 rather than Ti metal (figure 15(c)) [271]. It can be inferred that this interface yields a lower contact resistance than Ti deposited in UHV. This is supported by the demonstration that Ti deposited in UHV reacts with the MoS_2, thus resulting in the formation of TiS_x, MoS_x, and possible Mo metal at the interface. Such an interface will have markedly different charge transport characteristics than those predicted assuming a vdW or weak Ti–S bonding with no Mo–S bond scission [272, 273].

Beyond elemental metallic contacts, several novel approaches are being adopted such as using patterned graphene ribbons to provide edge contacts to TMDs grown between the contacts by MOCVD [274] as well as phase transitions from the semiconducting 2H to the metallic 1T-polytypes as discussed in the previous section [253]. It has also been recently demonstrated that encapsulating TMDs in hBN is a successful method to significantly reduce contact resistance [275, 276].

6. Further applications

6.1. Scalable processing and applications of 2D nanomaterial heterostructures

Advances in scalable nano-manufacturing of 2D materials are required to exploit their potential in real-world technology. Towards this end, researchers have begun exploring methods for improving the uniformity of solution-processed graphene and related 2D materials with an eye towards realizing dispersions and inks that can be deposited into large area thin-films [277]. In particular, as shown in figure 16, density gradient ultracentrifugation allows for the solution-based isolation of graphene [278], hBN [279], montmorillonite [280], and TMDs [281] with homogeneous thickness down to the atomically thin limit. Similarly, phosphorene has been isolated in organic solvents [282] or deoxygenated aqueous surfactant solutions [283, 284] with the resulting phosphorene nanosheets showing FET mobilities and ON/OFF ratios that are comparable to micromechanically exfoliated flakes. By adding cellulosic polymer stabilizers to these dispersions, the rheological properties can be tuned by orders of magnitude, thereby enabling 2D material inks that are compatible with a range of additive manufacturing methods including inkjet [285], gravure [286], screen [287], 3D printing [288], and photonic annealing [289].

Through sequential controlled deposition, these 2D materials can be stacked into heterostructures that have shown promise in several applications, including photodiodes [290], anti-ambipolar transistors [291], gate-tunable memristors [292], and heterojunction photovoltaics [293]. Unlike bulk semiconductors, the atomically thin nature of 2D materials implies incomplete screening of perpendicularly applied electric fields. Consequently, a gate potential can modulate the carrier concentration in multiple 2D nanomaterials concurrently when they are stacked into vertical heterostructures. In this manner, nearly any two-terminal, passive electronic device can be converted into a three-terminal, gate-tunable electronic device when it is constructed from a 2D nanomaterial heterostructure. For example, figures 16(c)–(e) shows a gate-tunable p–n heterojunction diode fabricated from a MoS_2/pentacene heterostructure [293]. The rectification ratio in the resulting diode characteristic can be tuned by orders of magnitude by varying the gate potential. Furthermore, the transfer characteristics of this device show strong anti-ambipolarity since the p-side and n-side of the heterojunction can be fully depleted at positive and negative gate voltage, respectively. Since MoS_2/pentacene forms a type II heterojunction, it further shows a strong photovoltaic response, which can also be tuned via the applied gate potential. In another example, figures 16(f)–(h) introduce a gate-tunable memristor based on polycrystalline CVD monolayer MoS_2 [292]. In this case, a lateral electric field leads to bistable switching that has been attributed to defect motion in non-stoichiometric CVD MoS_2. Since this memristor is fabricated from monolayer MoS_2, its charge transport characteristics are strongly influenced by an applied gate potential. Specifically, the gate voltage controls the switching characteristics, thereby allowing gate tunability over the memristive response with possible implications for non-volatile memory and/or neuromorphic computing applications.

6.2. Nanosculpting and bio-applications of 2D materials

6.2.1. Utilizing electron beams for nanosculpting 2D materials

The significant interest in 2D materials for applications also goes beyond electronic devices. Since the construction of the electron microscope in the first half of the twentieth century, electron beams have

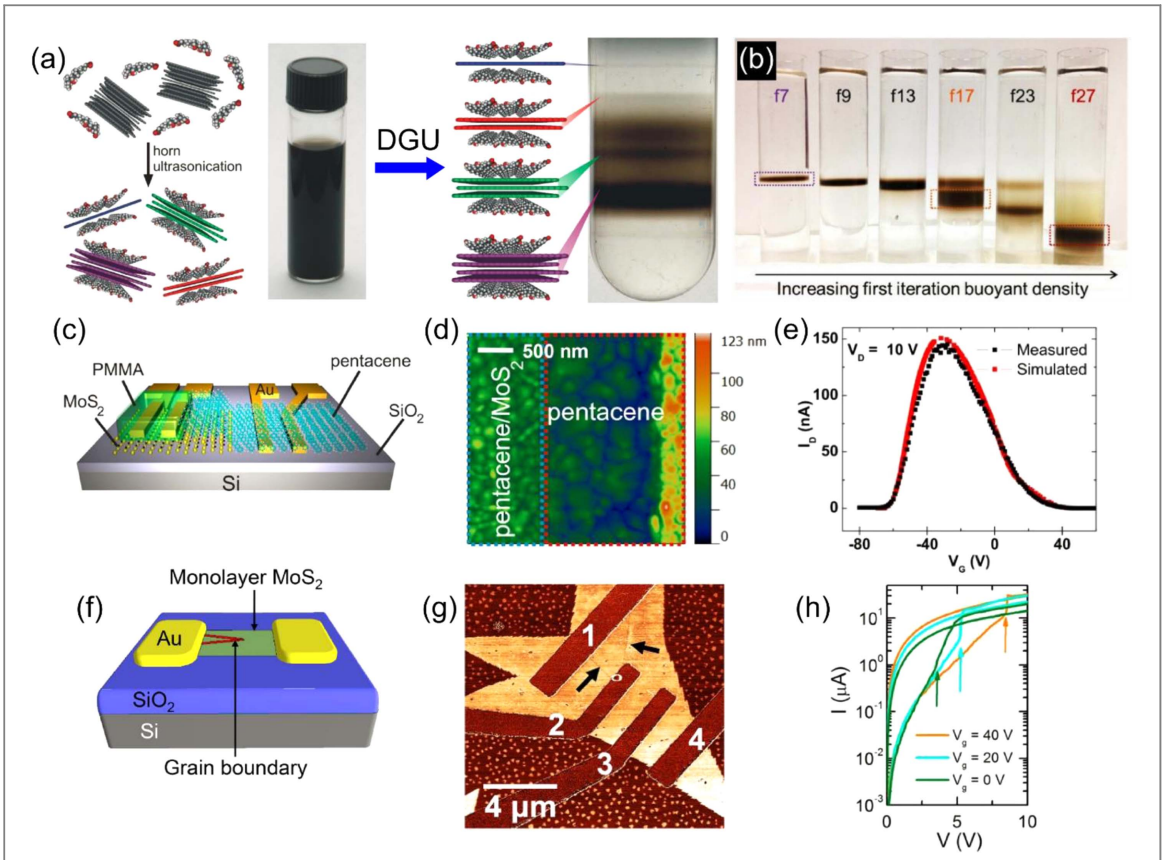

Figure 16. Scalable processing and applications of TMDs. (a) Isopycnic DGU allows aqueous surfactant dispersions of few-layer graphene to be separated by thickness with atomic precision. Reprinted with permission from [278]. Copyright 2009 American Chemical Society. (b) Isopycnic DGU separation of MoS_2 and by layer number. Reprinted with permission from [281]. Copyright 2014 Macmillan Publishers Ltd. (c) Schematic and (d) AFM image of a gate-tunable pentacene/MoS_2 p–n heterojunction diode. (e) Transfer curve of a gate-tunable pentacene/MoS_2 p–n heterojunction showing an asymmetric anti-ambipolar characteristic. (c)–(e) Reprinted with permission from [293]. Copyright 2016 American Chemical Society. (f) Schematic and (g) AFM image of a gate-tunable MoS_2 memristor. The polycrystalline single-layer MoS_2 is grown by CVD (grain boundaries are indicated with arrows). (h) Current–voltage curve showing bistable switching. The switching voltage is tuned by the gate potential. (f)–(h) Reprinted with permission from [292]. Copyright 2015 Macmillan Publishers Ltd.

constituted unique and powerful tools for probing and shaping materials with atomic resolution [39, 294]. In parallel, electron beams have been used well beyond material investigation and towards making atomically controlled devices on a chip (figure 17). Some examples include the early realization of solid-state nanopores for DNA analysis [295] and more recently, nanoribbons with desired lattice orientations [296–298] for one-dimensional conductor and interconnect applications, and nanoribbon-nanopore devices for biomolecular detection (figure 17(d)) [299–302].

In conjunction with recent advances in aberration corrected electron microscopy to study structure and defects [32, 294], many recent experiments have pushed the limits of device sizes to atomic scale in 2D materials beyond graphene (MoS_2, WS_2, $MoTe_2$, black phosphorous, etc) to expand their function and precision while addressing fundamental questions about structure and properties at nanometer and atomic scales. *In situ* TEM experiments have featured the fabrication of nanoribbons from novel 2D materials down to sub-nm widths. Notable examples include the TEM-beam carving of graphene nanoribbons [296, 303], graphene transistors (figure 17(a)) [304], phosphorene nanoribbons (figures 17(b) and (c)) [298], carbon chains [305], and simultaneous *in situ* electrical and structural investigations of such structures.

6.2.2. Applications of nanopores and nanoribbons in 2D materials for single biomolecule analysis

Ex situ TEM experiments using TEM-made structures include the ultrafast, all-electronic detection and analysis of biomolecules by driving them through tiny holes—or nanopores (figures 17(e) and (f))—in thin membranes. These experiments include the efforts towards mapping a human genome under 10 min. As molecules are driven through the nanopores in solution, they block the ion current flow, thus typically resulting in current reductions from which a molecule's physical and chemical properties are inferred. DNA, proteins, microRNA, and other biomolecules can be analyzed in this way. The temporal and spatial resolution, as well as sensitivity in these experiments, have been gradually improved over the last few years thanks to advanced materials, device designs, and new

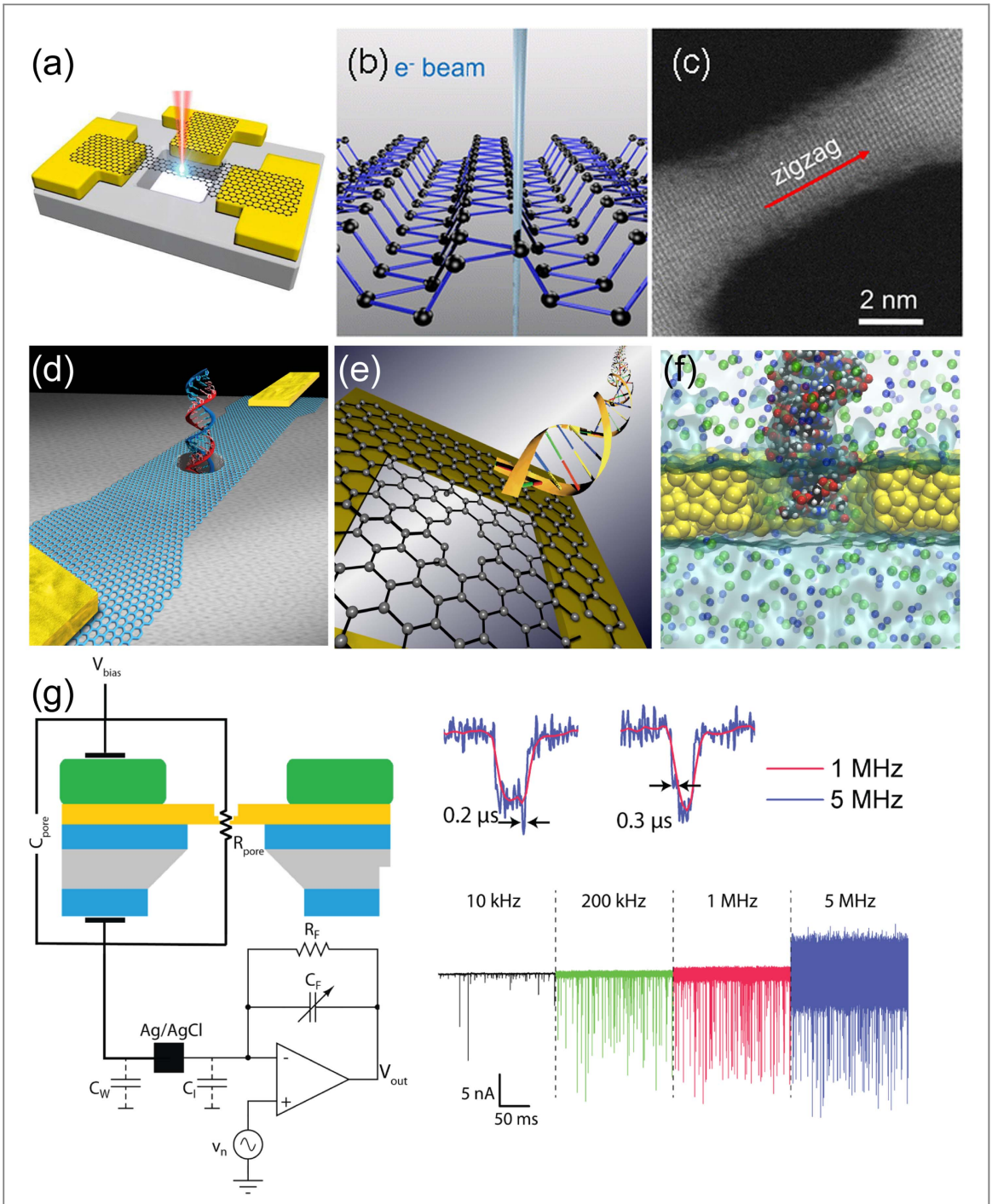

Figure 17. Nanosculpting of 2D materials and applications in biomolecule detection. (a) Illustration of the use of a focused electron beam of a TEM to fabricate a three-electrode geometry from a continuous 2D material where the third electrode operates as side gate in a FET configuration. Reprinted with permission from [304]. Copyright 2016 American Chemical Society. (b) and (c) Schematic illustration of a STEM beam nanosculpting of a few-layer black phosphorous membrane into a zigzag nanoribbon. Black phosphorous nanoribbons with desired crystal orientations can be narrowed and thinned in this way with sub-nanometer precision. (b) and (c) Reprinted with permission from [298]. Copyright 2016 American Chemical Society. (d) Illustration of 2D nanoribbon-nanopore devices envisioned for DNA sequencing. (e) and (f) Illustration of DNA translocation though a 2D nanopore and (e) another nanopore of comparable thickness in a single nm thin silicon membrane. (f) Reprinted with permission from [318]. Copyright 2015 American Chemical Society. (g) Recent realization of DNA translocation measurements with 100 ns time resolution. Reprinted with permission from [307]. Copyright 2016 American Chemical Society.

electronics. One important motivation for the development of solid-state nanopores (figures 17(d)–(g)) is the potential to tailor their size and composition to optimize sensitivity and interactions with particular analytes. Notable examples of recent solid-state nanopore chips advancements include examples of lowering the chip capacitance (and therefore the electronic noise) below 1 pF [306] as well as operating nanopores at bandwidths as high as 10 MHz towards realizing extremely fast detection (figure 17(g)) [307].

2D nanopores have also been envisioned as promising candidates to sequence DNA molecules by

recording the variations in ionic current as the molecules thread through the nanopore. Thinner nanopores lead to larger ionic currents due to decreased nanopore resistance. In addition, when nanopores are thin, only a small section of the molecule resides in the nanopore at a given time, thus making thin pores sensitive to small sections of the translocating molecule, as needed, for example, for DNA sequencing applications to be able to read a small number or individual DNA bases. Single- or few-atoms-thick nanopores in freestanding 2D atomically thin membranes are therefore expected to yield optimal signals that will fingerprint specific nanoparticles as they move through the nanopore.

Graphene, MoS_2, and boron nitride nanopores have been made using highly focused electron beams in the TEM and used for DNA detection [308–313]. Additionally, membrane electroporation [314, 315] has been successfully used to make nanopores in graphene [316] and MoS_2 [317] and DNA translocation have been demonstrated, opening possibilities towards inexpensive nanopore fabrication. Very recently, nanopores have been also made in other 2D materials such as phosphorene [298]. Interestingly, phosphorene nanopores were recently found to expand under electron illumination from circular to elliptical shape, preferentially along the zigzag direction.

7. Perspectives and future work

7.1. Colloidal synthesis

As can be seen from the examples given in section 2.3, significant progress has been made recently in the solution chemical synthesis of 2D metal chalcogenide nanostructures with desired structures and morphologies, offering an increasingly interesting complement to traditional gas-phase, exfoliation, and substrate-bound synthetic platforms for accessing single- and few-layer TMD materials. While TMDs naturally accommodate 2D nanosheet growth, controlling this growth and overcoming the tendency toward aggregation and nanoflower formation—e.g., forming discrete nanosheets versus multi-pronged cores that lead to multi-site nanosheet growth—requires a deeper understanding of the reaction chemistry and of the early stages of nucleation and growth. Harnessing this solution chemistry and using it to produce morphology- and size-controlled nanostructures, as well as vertically stacked heterostructures, of a diverse group of TMD systems will enable the rational construction of new 2D materials that can be made directly in high yield and in solution-dispersible form.

7.2. Doping

The various doping strategies that have already been employed to engineer the band structure and tune the properties of 2D materials have proven effective and versatile. As the need for multifunctional 2D electronics and optoelectronics keeps increasing, the further development and understanding/controlling doping by electromagnetic fields, substitutional doping and alloying within the 2D crystal lattice, and surface doping by physisorption or chemisorption will only increase as a rapidly emerging area for 2D materials. Moreover, the current doping strategies for 2D materials have already shown both advantages and disadvantages, and therefore combinations of these present potential pathways to compensate the drawbacks to further broaden the functionality of 2D materials. For substitutional lattice doping, many dopant atoms that are theoretically predicted to introduce promising electrical and magnetic properties have not been fully studied experimentally [113]. Novel synthetic pathways to overcome energy barriers must be explored to confront this challenge. Furthermore, understanding how to harness the beneficial opportunity provided by the heterogeneity introduced into pristine 2D lattices by substitutional doping or alloy formation is another research focus for the future. For example, how substitutional doping or alloying reduces or increases the levels and types of intrinsic defects in 2D lattices is still unclear. Can the energetics of alloy formation be understood to induce a switch from random alloy formation to long-range ordered superstructures and to heterojunctions with total phase separation? Such issues that couple theoretical predictions to guide experimental synthesis in realizable 2D systems, along with developments in characterization and assessment of functionality, provide a rich and fertile platform for future studies for many years to come.

Although straightforward and effective, ion doping has some critical pitfalls to avoid. For example, to avoid electrochemistry, where the ions exchange charge with the 2D crystal or the metal contacts, the gate bias must be restricted to the electrochemical window of the electrolyte. Within this window, the interactions between the ions and the induced image charge are purely electrostatic. Another example is water absorption, which will decrease the size of the electrochemical window and decrease the gate coupling [319]. Lastly, ion diffusion is orders of magnitude slower than electrons/holes and therefore slow sweep rates (e.g., 20 mV s^{-1} must be used to minimize hysteresis when using the ions as an electrolytic gate [109].

In less than a decade, the 2D crystal community has progressed from using ions for reconfigurable, unipolar doping of 2D crystals with ultra-high doping densities, to creating p–i–n junctions, to using these junctions to demonstrate current-induced EL. One of the major questions moving forward is whether electrolyte gating is simply an experimental tool for exploring new regimes of transport in 2D crystals or if it can be implemented in beyond complementary metal-oxide-semiconductor (CMOS) architectures.

Ions are typically avoided in device manufacturing; however, the emergence of ion-based resistive random access memories and the diffusion barriers used to contain Cu in CMOS manufacturing suggest that ion containment can be managed. Very large scale integration will require air-stable, solid-state, ultra-thin ion conductors that can be deposited uniformly and can withstand back-end-of-line processing temperatures. These requirements present an exciting challenge for the 2D crystal community moving forward.

7.3. Heterostructures

Regarding heterostructures, the possibilities are practically endless for what can be created by combining different 2D materials. In particular, there are many opportunities for enabling new functionality in graphene-based devices by controlling the coupling to other substrates. For example, using a substrate with strong spin–orbit coupling may be able to introduce a quantum spin-Hall state in graphene without magnetic fields [320]. The challenge will be identifying the proper combinations of materials and developing the measurement techniques to access the unique states that will be created. The substrate is critical to tune the properties of CVD-synthesized 2D TMDs, but many challenges to understanding the substrate-2D interaction and its impact on the device performance still remain unsolved.

7.4. Optical properties of STMDs

2D STMDs are likely to play significant roles in next-generation and model nanoscale optoelectronic devices. With the ability to directly probe light–matter interactions at critical characteristic length scales, nano-optical imaging and spectroscopy can provide valuable insight into underlying excitonic properties that can be used to both improve synthetic techniques and deterministically control nanoscale optoelectronic phenomena. From imaging and quantifying the effects of dopants, defects, edges, and heterostructure interfaces, to continuing to unravel the vexing local photophysics surrounding grain boundaries, to exploring complex many-body physics at nanoscale dimensions, and to developing chiral nano-optical probes for nanoscale valleytronics, many exciting possible nano-optical studies of these 2D materials exist. Aside from electron energy loss spectroscopy [321], which necessitates electron transparency and irradiation with an electron beam, nano-optics currently provides the only means to directly probe nanoscale excitonic phenomena and could ultimately prove as valuable to understanding excitons in 2D transition metal semiconductors as STM has been for understanding the nanoscale electronic properties of graphene.

With respect to the open questions regarding many-body interactions in 2D TMDs, obtaining the phase-diagram for the photoexcited free carrier ratio to Coulomb-bound excitons remains highly relevant. Of particular importance is the related issue of exciton formation, with recently reported ultra-fast sub-picosecond timescales in TMD monolayers [322]. In addition, the predicted strong renormalization of the bands across the Brillouin zone [144, 323], e.g., at the Σ and Q points, is intriguing and promising with respect to the possibility of an excitation-induced direct-to-indirect band gap transition, with consequences for optics and transport. Finally, tuning of the electronic band structure via static screening of the environment [324], using strong light–matter interaction in 2D TMDs for photonics and optoelectronics [325], as well as exploring correlated electronic phenomena, such as the Bose–Einstein condensation [326], in 2D layers and heterostructures provide a variety of venues, among many others, for future research of many-body physics in atomically thin materials.

Ultrafast structural response measurements open up new means of probing dynamic structural responses in monolayer and few-layer samples. Novel future opportunities exist here for applying single-shot studies to extract the mechanistic pathways associated with switching dynamics (e.g., 2H–1T or vice versa [327]) and for investigation of exciton-phonon interactions and associated charge transfer dynamics in monolayer TMDs, multi-layers, and more complex vertical heterostructures under a variety of triggers. Time-resolved x-ray studies complementary to the electron scattering measurements described above may be further capable of providing novel information concerning the structural response, probing both in-plane and out-of-plane degrees of freedom and their coupling.

7.5. Nanoelectronics

While significant progress has been made over the past several years in the design and fabrication of various TMD and heterostructure devices, challenges still remain and further studies are required for simultaneous demonstration of high ON-currents and low subthreshold swings. Further work on the two key integration challenges for 2D materials still remain: depositing ultra-thin, uniform high-k dielectric gate insulators and realizing low-resistance contacts. Moving forward, it is clear that scalable functionalization processes for TMDs are still required in order to achieve high-quality high-k dielectric layer via ALD. Since the 2D materials will likely be in contact with insulators, metals, and other semiconductors, it is vital to develop an understanding of how the layer interactions modify the properties of the materials when compared to those in an idealized isolated state. In terms of understanding the fundamental physics that would explain charge transport in metal-TMD contacts, the realities of the interface chemistry must be considered when comparing experimental results with theoretical models.

Despite the encouraging progress on understanding interlayer charge transfer, the biggest challenge in developing a sophisticated model is probably the lack of experimental techniques to accurately determine the charge transfer rate. Time resolved measurements reported thus far were performed with a time resolution of longer than 100 fs, which only allowed subtraction of the upper limit of the transfer time and hindered systematic investigations on how the transfer time is influenced by the experimental conditions and sample structures. Using shorter pulses could improve the time resolution; however, their inevitably wider bandwidth could compromise the layer selectivity of the pump and probe processes. In this regard, it might be beneficial to design vertical heterostructures to intentionally slow down the charge transfer process so that it can be time resolved. Such studies, combined with theoretical efforts, could help develop and refine models on interlayer charge transfer.

The performance and stability of phosphorene MOSFETs demonstrated to date imply that they may enable thin-film and flexible electronics to operate in the gigahertz range instead of the present megahertz range [245]. To this end, stability under both normal and accelerated operation conditions needs to be demonstrated [246], not just in storage. Additionally, reduction of the interface state density down to the 10^{11} cm^{-2} range needs to be quantified. The development of more effective doping and contacting techniques are also extremely crucial. In the long run, the biggest challenge that needs to be overcome is material synthesis for depositing phosphorene over a large area with high uniformity and reproducibility. Considering the intrinsic merits of phosphorene and the intense interest in it, rapid advancement on all fronts can be expected to continue. Eventually, phosphorene may compete with other 2D and 3D semiconductor materials in atomically thin MOSFETs for ultra-high-speed and ultra-low-power operations.

7.6. Applications and integration of 2D materials

While significant progress has been made in the scalable processing and applications of 2D nanomaterial heterostructures, several challenges remain for this field. In particular, at the atomically thin limit, most (if not all) of the atoms in the nanomaterial are at the surface, and thus the properties of 2D nanomaterials are highly sensitive to surface chemistry, underlying substrate, neighboring materials, and interfaces [328, 329]. With reduced degrees of freedom compared to bulk materials, 2D nanomaterials are also more strongly influenced by point and extended defects (e.g., vacancies, substitutional impurities, and grain boundaries) [330]. Consequently, growth and assembly methods that minimize or control defect structures [69, 331] are likely to have significant impact on the performance, reproducibility, and reliability of 2D nanomaterial heterostructure applications, particularly for vertical heterostructures where defects introduce leakage current pathways that limit the thinness of the constituent 2D nanomaterials [332]. Another emerging frontier is to directly synthesize novel 2D nanomaterials, especially in cases for which there is no bulk layered material available for exfoliation. A recent example is the growth of 2D boron (e.g., borophene) on Ag(111) substrates in ultrahigh vacuum [333]. Since these synthetic 2D nanomaterials are typically stabilized by the growth substrate, careful consideration will be required when developing transfer schemes and heterostructures with other materials. The broad and growing phase space for 2D nanomaterial heterostructures also presents significant design challenges, which may be addressable with computational materials science approaches including those being developed by the Materials Genome Initiative. By addressing these challenges and developing successful integration strategies, 2D nanomaterial heterostructures will not only yield interesting prototype devices, but will also be well-positioned for incorporation into sophisticated circuits and systems.

There are several notable challenges going forward before 2D solid-state nanopores are to be developed into a commercial platform. While the field of traditional silicon-based nanopores has matured over more than ten years, when it comes to new 2D materials, each one of them may present some materials-specific challenge to be surmounted. Such challenges may include the material transferring process from the growth substrate to suitable nanopore chips, or alternatively, the development of methods for materials growth over apertures for membrane applications [334]. Other examples may include issues related to nanopore wetting properties and the surface chemistry of the new material.

Acknowledgements

This review article was constructed based on the workshop 'Graphene and Beyond: From Atoms to Applications', hosted by the Center for 2-Dimensional and Layered Materials on 9–10 May 2016 at Penn State with sponsorship from FEI, HORIBA scientific, and Kurt J Lesker Company. Support was also provided by the Penn State Materials Research Institute and Center for Nanoscale Science. JAR and MT also acknowledge Rosemary Bittel for logistical support. The authors acknowledge the following funding agencies: AFOSR, DARPA, NSF, ONR, DOE, DTRA, STARnet, ARO, and Emmy Noether Programme.

References

[1] Novoselov K S, Geim A K, Morozov S V, Jiang D, Zhang Y, Dubonos S V, Grigorieva I V and Firsov A A 2004 Electric field effect in atomically thin carbon films *Science* **306** 666

[2] Butler S Z *et al* 2013 Progress, challenges, and opportunities in two-dimensional materials beyond graphene *ACS Nano* **7** 2898

[3] Wang Q H, Kalantar-Zadeh K, Kis A, Coleman J N and Strano M S 2012 Electronics and optoelectronics of two-dimensional transition metal dichalcogenides *Nat. Nanotechnol.* **7** 699

[4] Mak K F, Lee C, Hone J, Shan J and Heinz T F 2010 Atomically thin MoS_2: a new direct-gap semiconductor *Phys. Rev. Lett.* **105** 136805

[5] Splendiani A, Sun L, Zhang Y, Li T, Kim J, Chim C-Y, Galli G and Wang F 2010 Emerging photoluminescence in monolayer MoS_2 *Nano Lett.* **10** 1271

[6] Dean C R *et al* 2010 Boron nitride substrates for high-quality graphene electronics *Nat. Nanotechnol.* **5** 722

[7] Geim A K and Grigorieva I V 2013 Van der Waals heterostructures *Nature* **499** 419

[8] Terrones H, López-Urías F and Terrones M 2013 Novel hetero-layered materials with tunable direct band gaps by sandwiching different metal disulfides and diselenides *Sci. Rep.* **3** 1549

[9] Zhao P, Desai S, Tosun M, Roy T, Fang H, Sachid A, Amani M, Hu C and Javey A 2015 2D layered materials: from materials properties to device applications *2015 IEEE Int. Electron Devices Meeting (IEDM) (7–9 December 2015)* 27.3.1

[10] Bernardi M, Palummo M and Grossman J C 2013 Extraordinary sunlight absorption and one nanometer thick photovoltaics using two-dimensional monolayer materials *Nano Lett.* **13** 3664

[11] Lopez-Sanchez O, Lembke D, Kayci M, Radenovic A and Kis A 2013 Ultrasensitive photodetectors based on monolayer MoS_2 *Nat. Nanotechnol.* **8** 497

[12] Wu S *et al* 2015 Monolayer semiconductor nanocavity lasers with ultralow thresholds *Nature* **520** 69

[13] Radisavljevic B, Radenovic A, Brivio J, Giacometti I V and Kis A 2011 Single-layer MoS_2 transistors *Nat. Nanotechnol.* **6** 147

[14] Li X *et al* 2016 Two-dimensional GaSe/$MoSe_2$ misfit bilayer heterojunctions by van der Waals epitaxy *Sci. Adv.* **2** e1501882

[15] Mahjouri-Samani M *et al* 2015 Patterned arrays of lateral heterojunctions within monolayer two-dimensional semiconductors *Nat. Commun.* **6** 7749

[16] Gong Y *et al* 2014 Band gap engineering and layer-by-layer mapping of selenium-doped molybdenum disulfide *Nano Lett.* **14** 442

[17] Li H, Duan X, Wu X, Zhuang X, Zhou H, Zhang Q, Zhu X, Hu W, Ren P and Guo P 2014 Growth of alloy $MoS_{2x}Se_{2(1-x)}$ nanosheets with fully tunable chemical compositions and optical properties *J. Am. Chem. Soc.* **136** 3756

[18] Mann J *et al* 2014 2-dimensional transition metal dichalcogenides with tunable direct band gaps: $MoS_{2(1-x)}Se_{2x}$ monolayers *Adv. Mater.* **26** 1399

[19] Zhuang H L and Hennig R G 2013 Single-layer group-III monochalcogenide photocatalysts for water splitting *Chem. Mater.* **25** 3232

[20] Li X *et al* 2016 Suppression of defects and deep levels using isoelectronic tungsten substitution in monolayer MoSe2 *Adv. Funct. Mater.* (in press) (doi:10.1002/adfm.201603850)

[21] Yuan H T *et al* 2013 Zeeman-type spin splitting controlled by an electric field *Nat. Phys.* **9** 563

[22] Suh J *et al* 2014 Doping against the native propensity of MoS_2: degenerate hole doping by cation substitution *Nano Lett.* **14** 6976

[23] Jin Y, Keum D H, An S J, Kim J, Lee H S and Lee Y H 2015 A Van Der Waals homojunction: ideal p–n diode behavior in $MoSe_2$ *Adv. Mater.* **27** 5534

[24] Li H-M, Lee D, Qu D, Liu X, Ryu J, Seabaugh A and Yoo W J 2015 Ultimate thin vertical p–n junction composed of two-dimensional layered molybdenum disulfide *Nat. Commun.* **6** 6564

[25] Conley H J, Wang B, Ziegler J I, Haglund R F Jr, Pantelides S T and Bolotin K I 2013 Bandgap engineering of strained monolayer and bilayer MoS_2 *Nano Lett.* **13** 3626

[26] He K, Poole C, Mak K F and Shan J 2013 Experimental demonstration of continuous electronic structure tuning via strain in atomically thin MoS_2 *Nano Lett.* **13** 2931

[27] McCreary A *et al* 2016 Effects of uniaxial and biaxial strain on few-layered terrace structures of MoS_2 grown by vapor transport *ACS Nano* **10** 3186

[28] Akinwande D, Petrone N and Hone J 2014 Two-dimensional flexible nanoelectronics *Nat. Commun.* **5** 5678

[29] Wang H, Yuan H, Hong S S, Li Y and Cui Y 2015 Physical and chemical tuning of two-dimensional transition metal dichalcogenides *Chem. Soc. Rev.* **44** 2664

[30] Rao C and Maitra U 2015 Inorganic graphene analogs *Ann. Rev. Mater. Res.* **45** 29

[31] Lotsch B V 2015 Vertical 2D heterostructures *Ann. Rev. Mater. Res.* **45** 85

[32] Lin Z, Carvalho B R, Kahn E, Lv R, Rao R, Terrones H, Pimenta M A and Terrones M 2016 Defect engineering of two-dimensional transition metal dichalcogenides *2D Mater.* **3** 022002

[33] Kim S J, Choi K, Lee B, Kim Y and Hong B H 2015 Materials for flexible, stretchable electronics: graphene and 2D materials *Ann. Rev. Mater. Res.* **45** 63

[34] Kannan P K, Late D J, Morgan H and Rout C S 2015 Recent developments in 2D layered inorganic nanomaterials for sensing *Nanoscale* **7** 13293

[35] Jariwala D, Sangwan V K, Lauhon L J, Marks T J and Hersam M C 2014 Emerging device applications for semiconducting two-dimensional transition metal dichalcogenides *ACS Nano* **8** 1102

[36] Fiori G, Bonaccorso F, Iannaccone G, Palacios T, Neumaier D, Seabaugh A, Banerjee S K and Colombo L 2014 Electronics based on two-dimensional materials *Nat. Nanotechnol.* **9** 768

[37] Das S, Robinson J A, Dubey M, Terrones H and Terrones M 2015 Beyond graphene: progress in novel two-dimensional materials and van der Waals solids *Ann. Rev. Mater. Res.* **45** 1

[38] Chen Y, Tan C, Zhang H and Wang L 2015 Two-dimensional graphene analogues for biomedical applications *Chem. Soc. Rev.* **44** 2681

[39] Bhimanapati G R *et al* 2015 Recent advances in two-dimensional materials beyond graphene *ACS Nano* **9** 11509

[40] Desai S B *et al* 2016 Gold-mediated exfoliation of ultralarge optoelectronically-perfect monolayers *Adv. Mater.* **28** 4053

[41] Zhou Y, Kiriya D, Haller E E, Ager J W III, Javey A and Chrzan D C 2016 Compliant substrate epitaxy: Au on MoS_2 *Phys. Rev.* B **93** 054106

[42] Kang K, Xie S, Huang L, Han Y, Huang P Y, Mak K F, Kim C-J, Muller D and Park J 2015 High-mobility three-atom-thick semiconducting films with wafer-scale homogeneity *Nature* **520** 656

[43] Talapin D V, Lee J-S, Kovalenko M V and Shevchenko E V 2009 Prospects of colloidal nanocrystals for electronic and optoelectronic applications *Chem. Rev.* **110** 389

[44] Zhang X and Xie Y 2013 Recent advances in free-standing two-dimensional crystals with atomic thickness: design, assembly and transfer strategies *Chem. Soc. Rev.* **42** 8187

[45] Han J H, Lee S and Cheon J 2013 Synthesis and structural transformations of colloidal 2D layered metal chalcogenide nanocrystals *Chem. Soc. Rev.* **42** 2581

[46] Wang L, Song C, Shi Y, Dang L, Jin Y, Jiang H, Lu Q and Gao F 2016 Generalized low-temperature fabrication of scalable multi-type two-dimensional nanosheets with a green soft template *Chem. Eur. J.* **22** 5575

[47] Sun D, Feng S, Terrones M and Schaak R E 2015 Formation and interlayer decoupling of colloidal $MoSe_2$ nanoflowers *Chem. Mater.* **27** 3167

[48] Yoo D, Kim M, Jeong S, Han J and Cheon J 2014 Chemical synthetic strategy for single-layer transition-metal chalcogenides *J. Am. Chem. Soc.* **136** 14670

[49] Jung W, Lee S, Yoo D, Jeong S, Miro P, Kuc A, Heine T and Cheon J 2015 Colloidal synthesis of single-layer MSe_2 (M = Mo, W) nanosheets via anisotropic solution-phase growth approach *J. Am. Chem. Soc.* **137** 7266

[50] Vaughn D D, In S-I and Schaak R E 2011 A precursor-limited nanoparticle coalescence pathway for tuning the thickness of laterally-uniform colloidal nanosheets: the case of SnSe *ACS Nano* **5** 8852

[51] Mahler B, Hoepfner V, Liao K and Ozin G A 2014 Colloidal synthesis of 1T–WS_2 and 2H–WS_2 nanosheets: applications for photocatalytic hydrogen evolution *J. Am. Chem. Soc.* **136** 14121

[52] Keum D H *et al* 2015 Bandgap opening in few-layered monoclinic $MoTe_2$ *Nat. Phys.* **11** 482

[53] Duerloo K-A N, Li Y and Reed E J 2014 Structural phase transitions in two-dimensional Mo-and W-dichalcogenide monolayers *Nat. Commun.* **5** 4214

[54] Zhou Y and Reed E J 2015 Structural phase stability control of monolayer $MoTe_2$ with adsorbed atoms and molecules *J. Phys. Chem.* C **119** 21674

[55] Song S, Keum D H, Cho S, Perello D, Kim Y and Lee Y H 2015 Room temperature semiconductor–metal transition of $MoTe_2$ thin films engineered by strain *Nano Lett.* **16** 188

[56] Cho S *et al* 2015 Phase patterning for ohmic homojunction contact in $MoTe_2$ *Science* **349** 625

[57] Park J C, Yun S J, Kim H, Park J-H, Chae S H, An S-J, Kim J-G, Kim S M, Kim K K and Lee Y H 2015 Phase-engineered synthesis of centimeter-scale 1T′-and 2H–molybdenum ditelluride thin films *ACS Nano* **9** 6548

[58] Sun Y F *et al* 2016 Low-temperature solution synthesis of few-layer 1T'-$MoTe_2$ nanostructures exhibiting lattice compression *Angew. Chem,. Int. Ed.* **55** 2830

[59] Dumcenco D *et al* 2015 Large-area epitaxial monolayer MoS_2 *ACS Nano* **9** 4611

[60] van der Zande A M, Huang P Y, Chenet D A, Berkelbach T C, You Y, Lee G-H, Heinz T F, Reichman D R, Muller D A and Hone J C 2013 Grains and grain boundaries in highly crystalline monolayer molybdenum disulphide *Nat. Mater.* **12** 554

[61] Shi J *et al* 2014 Controllable growth and transfer of monolayer MoS_2 on Au foils and its potential application in hydrogen evolution reaction *ACS Nano* **8** 10196

[62] Lin Y C *et al* 2014 Direct synthesis of van der Waals solids *ACS Nano* **8** 3715

[63] Azizi A *et al* 2015 Freestanding van der Waals heterostructures of graphene and transition metal dichalcogenides *ACS Nano* **9** 4882

[64] Ruzmetov D *et al* 2016 Vertical 2D/3D semiconductor heterostructures based on epitaxial molybdenum disulfide and gallium nitride *ACS Nano* **10** 3580

[65] Hou J *et al* 2016 Modulating photoluminescence of monolayer molybdenum disulfide by metal-insulator phase transition in active substrates *Small* **12** 3976

[66] Li Y, Qi Z, Liu M, Wang Y, Cheng X, Zhang G and Sheng L 2014 Photoluminescence of monolayer MoS_2 on $LaAlO_3$ and $SrTiO_3$ substrates *Nanoscale* **6** 15248

[67] Koma A and Yoshimura K 1986 Ultrasharp interfaces grown with Van der Waals epitaxy *Surf. Sci.* **174** 556

[68] Yamada A, Ho K, Maruyama T and Akimoto K 1999 Molecular beam epitaxy of GaN on a substrate of MoS_2 layered compound *Appl. Phys.* A **69** 89

[69] Liu X, Balla I, Bergeron H, Campbell G P, Bedzyk M J and Hersam M C 2015 Rotationally commensurate growth of MoS_2 on epitaxial graphene *ACS Nano* **10** 1067

[70] Giusca C E *et al* 2016 Excitonic effects in tungsten disulphide monolayers on two-layer graphene *ACS Nano* **10** 7840

[71] Lin Y C *et al* 2014 Atomically thin heterostructures based on single-layer tungsten diselenide and graphene *Nano Lett.* **14** 6936

[72] Li X *et al* 2015 Van der Waals epitaxial growth of two-dimensional single-crystalline GaSe domains on graphene *ACS Nano* **9** 8078

[73] Gupta P *et al* 2016 Layered transition metal dichalcogenides: promising near-lattice-matched substrates for GaN growth *Sci. Rep.* **6** 23708

[74] Gray D, McCaughan A and Mookerji B 2009 Crystal structure of graphite, graphene and silicon *Lecture* (Cambridge: Massachusetts Institute of Technology)

[75] Cao T *et al* 2012 Valley-selective circular dichroism of monolayer molybdenum disulphide *Nat. Commun.* **3** 887

[76] Banerjee K, Liu W and Kang J 2013 High-performance field-effect-transistors on monolayer-WSe_2 *Meeting Abstracts* (The Electrochemical Society) 2182

[77] Lin Y C *et al* 2015 Atomically thin resonant tunnel diodes built from synthetic van der Waals heterostructures *Nat. Commun.* **6** 7311

[78] Zhang K H *et al* 2015 Manganese doping of monolayer MoS_2: the substrate is critical *Nano Lett.* **15** 6586

[79] Ji Q, Kan M, Zhang Y, Guo Y, Ma D, Shi J, Sun Q, Chen Q, Zhang Y and Liu Z 2014 Unravelling orientation distribution and merging behavior of monolayer MoS_2 domains on sapphire *Nano Lett.* **15** 198

[80] Al Balushi Z Y *et al* 2016 Two-dimensional gallium nitride realized via graphene encapsulation *Nat. Mater.* **15** 1166

[81] Chen L, Liu B, Ge M, Ma Y, Abbas A N and Zhou C 2015 Step-edge-guided nucleation and growth of aligned WSe_2 on sapphire via a layer-over-layer growth mode *ACS Nano* **9** 8368

[82] Liu W and Chen N 1995 Decrease of dislocations in GaAs by isoelectronic doping of liquid phase epitaxial layers *J. Cryst. Growth* **154** 19

[83] Song J G *et al* 2015 Controllable synthesis of molybdenum tungsten disulfide alloy for vertically composition-controlled multilayer *Nat. Commun.* **6** 7817

[84] Zheng S, Sun L, Yin T, Dubrovkin A M, Liu F, Liu Z, Shen Z X and Fan H J 2015 Monolayers of $W_xMo_{1-x}S_2$ alloy heterostructure with in-plane composition variations *Appl. Phys. Lett.* **106** 063113

[85] Dumcenco D O, Kobayashi H, Liu Z, Huang Y-S and Suenaga K 2013 Visualization and quantification of transition metal atomic mixing in $Mo_{1-x}W_xS_2$ single layers *Nat. Commun.* **4** 1351

[86] Yoshida S, Kobayashi Y, Sakurada R, Mori S, Miyata Y, Mogi H, Koyama T, Takeuchi O and Shigekawa H 2015 Microscopic basis for the band engineering of $Mo_{1-x}W_xS_2$-based heterojunction *Sci. Rep.* **5** 14808

[87] Lin Z, Thee M T, Elías A L, Feng S, Zhou C, Fujisawa K, Perea-López N, Carozo V, Terrones H and Terrones M 2014 Facile synthesis of MoS_2 and $Mo_xW_{1-x}S_2$ triangular monolayers *APL Mater.* **2** 092514

[88] Chhowalla M, Shin H S, Eda G, Li L-J, Loh K P and Zhang H 2013 The chemistry of two-dimensional layered transition metal dichalcogenide nanosheets *Nat. Chem.* **5** 263

[89] Wang G *et al* 2015 Spin–orbit engineering in transition metal dichalcogenide alloy monolayers *Nat. Commun.* **6** 10110

[90] Kutana A, Penev E S and Yakobson B I 2014 Engineering electronic properties of layered transition-metal dichalcogenide compounds through alloying *Nanoscale* **6** 5820

[91] Huang B, Yoon M, Sumpter B G, Wei S-H and Liu F 2015 Alloy engineering of defect properties in semiconductors: suppression of deep levels in transition-metal dichalcogenides *Phys. Rev. Lett.* **115** 126806

[92] Li X *et al* 2016 Isoelectronic tungsten doping in monolayer $MoSe_2$ for carrier type modulation *Adv. Mater.* **28** 8240

[93] Wang X *et al* 2014 Chemical vapor deposition growth of crystalline monolayer $MoSe_2$ *ACS Nano* **8** 5125

[94] Zhou H *et al* 2015 Large area growth and electrical properties of p-type WSe_2 atomic layers *Nano Lett.* **15** 709

[95] Cheng R, Li D, Zhou H, Wang C, Yin A, Jiang S, Liu Y, Chen Y, Huang Y and Duan X 2014 Electroluminescence and photocurrent generation from atomically sharp WSe_2/MoS_2 heterojunction p–n diodes *Nano Lett.* **14** 5590

[96] Liu W, Kang J, Sarkar D, Khatami Y, Jena D and Banerjee K 2013 Role of metal contacts in designing high-performance monolayer n-type WSe_2 field effect transistors *Nano Lett.* **13** 1983

[97] Li X, Lin M-W, Puretzky A A, Basile L, Wang K, Idrobo J C, Rouleau C M, Geohegan D B and Xiao K 2016 Persistent photoconductivity in two-dimensional $Mo_{1-x}W_xSe_2$–$MoSe_2$ van der Waals heterojunctions *J. Mater. Res.* **31** 923
[98] Das A *et al* 2008 Monitoring dopants by Raman scattering in an electrochemically top-gated graphene transistor *Nat. Nanotechnol.* **3** 210
[99] Efetov D K and Kim P 2010 Controlling electron–phonon interactions in graphene at ultrahigh carrier densities *Phys. Rev. Lett.* **105** 256805
[100] Ye J, Craciun M F, Koshino M, Russo S, Inoue S, Yuan H, Shimotani H, Morpurgo A F and Iwasa Y 2011 Accessing the transport properties of graphene and its multilayers at high carrier density *Proc. Natl Acad. Sci. USA* **108** 13002
[101] Yuan H, Toh M, Morimoto K, Tan W, Wei F, Shimotani H, Kloc C and Iwasa Y 2011 Liquid-gated electric-double-layer transistor on layered metal dichalcogenide, SnS_2 *Appl. Phys. Lett.* **98** 012102
[102] Pu J, Yomogida Y, Liu K-K, Li L-J, Iwasa Y and Takenobu T 2012 Highly flexible MoS_2 thin-film transistors with ion gel dielectrics *Nano Lett.* **12** 4013
[103] Perera M M, Lin M-W, Chuang H-J, Chamlagain B P, Wang C, Tan X, Cheng M M-C, Tománek D and Zhou Z 2013 Improved carrier mobility in few-layer MoS_2 field-effect transistors with ionic-liquid gating *ACS Nano* **7** 4449
[104] Yuan H *et al* 2014 Generation and electric control of spin-valley-coupled circular photogalvanic current in WSe_2 *Nat. Nanotechnol.* **9** 851
[105] Allain A and Kis A 2014 Electron and hole mobilities in single-layer WSe_2 *ACS Nano* **8** 7180
[106] Fathipour S, Pandey P, Fullerton-Shirey S K and Seabaugh A 2016 Electric-double-layer doping of WSe_2 field-effect transistors using polyethylene-oxide cesium perchlorate *J. Appl. Phys.* (accepted)
[107] Saito Y and Iwasa Y 2015 Ambipolar insulator-to-metal transition in black phosphorus by ionic-liquid gating *ACS Nano* **9** 3192
[108] Shi W, Ye J, Zhang Y, Suzuki R, Yoshida M, Miyazaki J, Inoue N, Saito Y and Iwasa Y 2015 Superconductivity series in transition metal dichalcogenides by ionic gating *Sci. Rep.* **5** 12534
[109] Xu H L, Fathipour S, Kinder E W, Seabaugh A C and Fullerton-Shirey S K 2015 Reconfigurable ion gating of 2H–$MoTe_2$ field-effect transistors using poly(ethylene oxide)-$CsClO_4$ solid polymer electrolyte *ACS Nano* **9** 4900
[110] Pei T, Bao L, Wang G, Ma R, Yang H, Li J, Gu C, Pantelides S, Du S and Gao H-J 2016 Few-layer $SnSe_2$ transistors with high on/off ratios *Appl. Phys. Lett.* **108** 053506
[111] Kim S H, Hong K, Xie W, Lee K H, Zhang S, Lodge T P and Frisbie C D 2013 Electrolyte-gated transistors for organic and printed electronics *Adv. Mater.* **25** 1822
[112] Ye J, Zhang Y, Kasahara Y and Iwasa Y 2013 Interface transport properties in ion-gated nano-sheets *Eur. Phys. J. Spec. Top.* **222** 1185
[113] Azcatl A *et al* 2016 Covalent nitrogen doping and compressive strain in MoS_2 by remote N_2 plasma exposure *Nano Lett.* **16** 5437
[114] Do C, Lunkenheimer P, Diddens D, Götz M, Weiß M, Loidl A, Sun X-G, Allgaier J and Ohl M 2013 Li^+ transport in poly (ethylene oxide) based electrolytes: neutron scattering, dielectric spectroscopy, and molecular dynamics simulations *Phys. Rev. Lett.* **111** 018301
[115] Zhang Y, Oka T, Suzuki R, Ye J and Iwasa Y 2014 Electrically switchable chiral light-emitting transistor *Science* **344** 725
[116] Zhang Y, Ye J, Yomogida Y, Takenobu T and Iwasa Y 2013 Formation of a stable p–n junction in a liquid-gated MoS_2 ambipolar transistor *Nano Lett.* **13** 3023
[117] Costanzo D, Jo S, Berger H and Morpurgo A F 2016 Gate-induced superconductivity in atomically thin MoS_2 crystals *Nat. Nanotechnol.* **11** 339
[118] Kim K *et al* 2016 van der Waals Heterostructures with high accuracy rotational alignment *Nano Lett.* **16** 1989
[119] Yankowitz M, Watanabe K, Taniguchi T, San-Jose P and LeRoy B J 2016 Pressure-induced commensurate stacking of graphene on boron nitride *Nat. Commun.* **7** 13168
[120] Dos Santos J L, Peres N and Neto A C 2007 Graphene bilayer with a twist: electronic structure *Phys. Rev. Lett.* **99** 256802
[121] Wong D *et al* 2015 Local spectroscopy of moire-induced electronic structure in gate-tunable twisted bilayer graphene *Phys. Rev.* B **92** 155409
[122] Yankowitz M, Wang J I J, Li S C, Birdwell A G, Chen Y A, Watanabe K, Taniguchi T, Quek S Y, Jarillo-Herrero P and LeRoy B J 2014 Band structure mapping of bilayer graphene via quasiparticle scattering *APL Mater.* **2** 092503
[123] Yankowitz M, McKenzie D and LeRoy B J 2015 Local spectroscopic characterization of spin and layer polarization in WSe_2 *Phys. Rev. Lett.* **115** 136803
[124] Lien D H *et al* 2015 Engineering light outcoupling in 2D materials *Nano Lett.* **15** 1356
[125] Schnitzer I, Yablonovitch E, Caneau C and Gmitter T 1993 Ultrahigh spontaneous emission quantum efficiency, 99.7% internally and 72% externally, from AlGaAs/GaAs/AlGaAs double heterostructures *Appl. Phys. Lett.* **62** 131
[126] Eva A and Conte S 2016 Exciton and charge carrier dynamics in few-layer WS_2 *Nanoscale* **8** 5428
[127] Amani M *et al* 2015 Near-unity photoluminescence quantum yield in MoS_2 *Science* **350** 1065
[128] Han H V *et al* 2016 Photoluminescence enhancement and structure repairing of monolayer $MoSe_2$ by hydrohalic acid treatment *ACS Nano* **10** 1454
[129] Amani M, Taheri P, Addou R, Ahn G H, Kiriya D, Lien D-H, Ager J W III, Wallace R M and Javey A 2016 Recombination kinetics and effects of superacid treatment in sulfur-and selenium-based transition metal dichalcogenides *Nano Lett.* **16** 2786
[130] Amani M *et al* 2016 High luminescence efficiency in MoS_2 grown by chemical vapor deposition *ACS Nano* **10** 6535
[131] Yu H, Cui X, Xu X and Yao W 2015 Valley excitons in two-dimensional semiconductors *Natl Sci. Rev.* **0** 1
[132] Ramasubramaniam A 2012 Large excitonic effects in monolayers of molybdenum and tungsten dichalcogenides *Phys. Rev.* B **86** 115409
[133] Li Y, Chernikov A, Zhang X, Rigosi A, Hill H M, van der Zande A M, Chenet D A, Shih E-M, Hone J and Heinz T F 2014 Measurement of the optical dielectric function of monolayer transition-metal dichalcogenides: MoS_2, $MoSe_2$, WS_2, and WSe_2 *Phys. Rev.* B **90** 205422
[134] Cheiwchanchamnangij T and Lambrecht W R 2012 Quasiparticle band structure calculation of monolayer, bilayer, and bulk MoS_2 *Phys. Rev.* B **85** 205302
[135] Qiu D Y, Felipe H and Louie S G 2013 Optical spectrum of MoS_2: many-body effects and diversity of exciton states *Phys. Rev. Lett.* **111** 216805
[136] Zhang C, Johnson A, Hsu C-L, Li L-J and Shih C-K 2014 Direct imaging of band profile in single layer MoS_2 on graphite: quasiparticle energy gap, metallic edge states, and edge band bending *Nano Lett.* **14** 2443
[137] He K, Kumar N, Zhao L, Wang Z, Mak K F, Zhao H and Shan J 2014 Tightly bound excitons in monolayer WSe_2 *Phys. Rev. Lett.* **113** 026803
[138] Chernikov A, Berkelbach T C, Hill H M, Rigosi A, Li Y, Aslan O B, Reichman D R, Hybertsen M S and Heinz T F 2014 Exciton binding energy and nonhydrogenic Rydberg series in monolayer WS_2 *Phys. Rev. Lett.* **113** 076802
[139] Ye Z, Cao T, O'Brien K, Zhu H, Yin X, Wang Y, Louie S G and Zhang X 2014 Probing excitonic dark states in single-layer tungsten disulphide *Nature* **513** 214
[140] Ugeda M M *et al* 2014 Giant bandgap renormalization and excitonic effects in a monolayer transition metal dichalcogenide semiconductor *Nat. Mater.* **13** 1091
[141] Haug H and Koch S W 2004 *Quantum Theory of the Optical and Electronic Properties of Semiconductors* vol 5 (Singapore: World Scientific)
[142] Chernikov A, Ruppert C, Hill H M, Rigosi A F and Heinz T F 2015 Population inversion and giant bandgap

renormalization in atomically thin WS_2 layers *Nat. Photon.* **9** 466
[143] Ulstrup S *et al* 2016 Ultrafast band structure control of a two-dimensional heterostructure *ACS Nano* **10** 6315
[144] Steinhoff A, Rosner M, Jahnke F, Wehling T O and Gies C 2014 Influence of excited carriers on the optical and electronic properties of MoS_2 *Nano Lett.* **14** 3743
[145] Chernikov A, van der Zande A M, Hill H M, Rigosi A F, Velauthapillai A, Hone J and Heinz T F 2015 Electrical tuning of exciton binding energies in monolayer WS_2 *Phys. Rev. Lett.* **115** 126802
[146] Yu Y *et al* 2015 Exciton-dominated dielectric function of atomically thin MoS_2 films *Sci. Rep.* **5** 16996
[147] Liu Z *et al* 2014 Strain and structure heterogeneity in MoS_2 atomic layers grown by chemical vapour deposition *Nat. Commun.* **5** 5246
[148] Mak K F, He K, Lee C, Lee G H, Hone J, Heinz T F and Shan J 2013 Tightly bound trions in monolayer MoS_2 *Nat. Mater.* **12** 207
[149] Peimyoo N, Yang W, Shang J, Shen X, Wang Y and Yu T 2014 Chemically driven tunable light emission of charged and neutral excitons in monolayer WS_2 *ACS Nano* **8** 11320
[150] Tongay S *et al* 2013 Defects activated photoluminescence in two-dimensional semiconductors: interplay between bound, charged, and free excitons *Sci. Rep.* **3** 2657
[151] Atkin J M, Berweger S, Jones A C and Raschke M B 2012 Nano-optical imaging and spectroscopy of order, phases, and domains in complex solids *Adv. Phys.* **61** 745
[152] Bao W *et al* 2015 Visualizing nanoscale excitonic relaxation properties of disordered edges and grain boundaries in monolayer molybdenum disulfide *Nat. Commun.* **6** 7993
[153] Lee Y, Park S, Kim H, Han G H, Lee Y H and Kim J 2015 Characterization of the structural defects in CVD-grown monolayered MoS_2 using near-field photoluminescence imaging *Nanoscale* **7** 11909
[154] Park K-D, Khatib O, Kravtsov V, Clark G, Xu X and Raschke M B 2016 Hybrid tip-enhanced nanospectroscopy and nanoimaging of monolayer WSe_2 with local strain control *Nano Lett.* **16** 2621
[155] Su W, Kumar N, Mignuzzi S, Crain J and Roy D 2016 Nanoscale mapping of excitonic processes in single-layer MoS_2 using tip-enhanced photoluminescence microscopy *Nanoscale* **8** 10564
[156] Nozaki J, Mori S, Miyata Y, Maniwa Y and Yanagi K 2016 Local optical absorption spectra of MoS_2 monolayers obtained using scanning near-field optical microscopy measurements *Japan. J. Appl. Phys.* **55** 038003
[157] Bao W *et al* 2012 Mapping local charge recombination heterogeneity by multidimensional nanospectroscopic imaging *Science* **338** 1317
[158] Ogletree D F *et al* 2015 Revealing optical properties of reduced-dimensionality materials at relevant length scales *Adv. Mater.* **27** 5693
[159] Zhang Y B, Brar V W, Girit C, Zettl A and Crommie M F 2009 Origin of spatial charge inhomogeneity in graphene *Nat. Phys.* **5** 722
[160] Cui Q, Ceballos F, Kumar N and Zhao H 2014 Transient absorption microscopy of monolayer and bulk WSe_2 *ACS Nano* **8** 2970
[161] Wang R, Ruzicka B A, Kumar N, Bellus M Z, Chiu H-Y and Zhao H 2012 Ultrafast and spatially resolved studies of charge carriers in atomically thin molybdenum disulfide *Phys. Rev.* B **86** 045406
[162] Murakami S, Nagaosa N and Zhang S C 2003 Dissipationless quantum spin current at room temperature *Science* **301** 1348
[163] Awschalom D D and Flatte M E 2007 Challenges for semiconductor spintronics *Nat. Phys.* **3** 153
[164] Zutic I, Fabian J and Das Sarma S 2004 Spintronics: fundamentals and applications *Rev. Mod. Phys.* **76** 323
[165] Xiao D, Liu G B, Feng W X, Xu X D and Yao W 2012 Coupled spin and valley physics in monolayers of MoS_2 and other group-VI dichalcogenides *Phys. Rev. Lett.* **108** 196802
[166] Yao W, Xiao D and Niu Q 2008 Valley-dependent optoelectronics from inversion symmetry breaking *Phys. Rev.* B **77** 235406
[167] Rycerz A, Tworzydlo J and Beenakker C W J 2007 Valley filter and valley valve in graphene *Nat. Phys.* **3** 172
[168] Xiao D, Yao W and Niu Q 2007 Valley-contrasting physics in graphene: magnetic moment and topological transport *Phys. Rev. Lett.* **99** 236809
[169] Mak K F, He K L, Shan J and Heinz T F 2012 Control of valley polarization in monolayer MoS_2 by optical helicity *Nat. Nanotechnol.* **7** 494
[170] Zeng H L, Dai J F, Yao W, Xiao D and Cui X D 2012 Valley polarization in MoS_2 monolayers by optical pumping *Nat. Nanotechnol.* **7** 490
[171] Cao T, Wang G, Han W P, Ye H Q, Zhu C R, Shi J R, Niu Q, Tan P H, Wang E, Liu B L and Feng J 2012 Valley-selective circular dichroism of monolayer molybdenum disulphide *Nat. Commun.* **3** 887
[172] Jones A M *et al* 2013 Optical generation of excitonic valley coherence in monolayer WSe_2 *Nat. Nanotechnol.* **8** 634
[173] Ross J S *et al* 2013 Electrical control of neutral and charged excitons in a monolayer semiconductor *Nat. Commun.* **4** 1474
[174] Ganichev S D, Ivchenko E L, Bel'kov V V, Tarasenko S A, Sollinger M, Weiss D, Wegscheider W and Prettl W 2002 Spin-galvanic effect *Nature* **417** 153
[175] Kikkawa J M and Awschalom D D 1999 Lateral drag of spin coherence in gallium arsenide *Nature* **397** 139
[176] Ivchenko E L and Ganichev S D 2008 Spin-photogalvanics *Spin Phys. Semicond.* **157** 245
[177] Ganichev S D and Prettl W 2003 Spin photocurrents in quantum wells *J. Phys.: Condens. Matter* **15** R935
[178] McIver J W, Hsieh D, Steinberg H, Jarillo-Herrero P and Gedik N 2012 Control over topological insulator photocurrents with light polarization *Nat. Nanotechnol.* **7** 96
[179] Karch J, Tarasenko S A, Ivchenko E L, Kamann J, Olbrich P, Utz M, Kvon Z D and Ganichev S D 2011 Photoexcitation of valley-orbit currents in (111)-oriented silicon metal-oxide-semiconductor field-effect transistors *Phys. Rev.* B **83** 121312(R)
[180] Karch J, Tarasenko S A, Olbrich P, Schonberger T, Reitmaier C, Plohmann D, Kvon Z D and Ganichev S D 2010 Orbital photogalvanic effects in quantum-confined structures *J. Phys.: Condens. Matter* **22** 355307
[181] Yuan H T, Wang X Q, Lian B, Zhang H J, Fang X F, Shen B, Xu G, Xu Y, Zhang S C, Hwang H Y and Cui Y 2014 Generation and electric control of spin-valley-coupled circular photogalvanic current in WSe_2 *Nat. Nanotechnol.* **9** 851
[182] Yuan H T, Shimotani H, Tsukazaki A, Ohtomo A, Kawasaki M and Iwasa Y 2009 High-density carrier accumulation in ZnO field-effect transistors gated by electric double layers of ionic liquids *Adv. Funct. Mater.* **19** 1046
[183] Dhoot A S, Israel C, Moya X, Mathur N D and Friend R H 2009 Large electric field effect in electrolyte-gated manganites *Phys. Rev. Lett.* **102** 136402
[184] Ueno K, Nakamura S, Shimotani H, Yuan H T, Kimura N, Nojima T, Aoki H, Iwasa Y and Kawasaki M 2011 Discovery of superconductivity in $KTaO_3$ by electrostatic carrier doping *Nat. Nanotechnol.* **6** 408
[185] Bollinger A T, Dubuis G, Yoon J, Pavuna D, Misewich J and Bozovic I 2011 Superconductor-insulator transition in $La_{2-x}Sr_xCuO_4$ at the pair quantum resistance *Nature* **472** 458
[186] Yamada Y, Ueno K, Fukumura T, Yuan H T, Shimotani H, Iwasa Y, Gu L, Tsukimoto S, Ikuhara Y and Kawasaki M 2011 Electrically induced ferromagnetism at room temperature in cobalt-doped titanium dioxide *Science* **332** 1065
[187] Jeong J, Aetukuri N, Graf T, Schladt T D, Samant M G and Parkin S S P 2013 Suppression of metal-insulator transition in VO_2 by electric field-induced oxygen vacancy formation *Science* **339** 1402

[188] Yin C M et al 2013 Tunable surface electron spin splitting with electric double-layer transistors based on InN Nano Lett. 13 2024
[189] Shibata K, Yuan H T, Iwasa Y and Hirakawa K 2013 Large modulation of zero-dimensional electronic states in quantum dots by electric-double-layer gating Nat. Commun. 4 2664
[190] Cho J H, Lee J, Xia Y, Kim B, He Y Y, Renn M J, Lodge T P and Frisbie C D 2008 Printable ion-gel gate dielectrics for low-voltage polymer thin-film transistors on plastic Nat. Mater. 7 900
[191] Eginligil M, Cao B C, Wang Z L, Shen X N, Cong C X, Shang J Z, Soci C and Yu T 2015 Dichroic spin-valley photocurrent in monolayer molybdenum disulphide Nat. Commun. 6 7636
[192] Ferrari A C et al 2006 Raman spectrum of graphene and graphene layers Phys. Rev. Lett. 97 187401
[193] Zhao Y et al 2013 Interlayer breathing and shear modes in few-trilayer MoS_2 and WSe_2 Nano Lett. 13 1007
[194] Boschetto D, Malard L, Lui C H, Mak K F, Li Z, Yan H and Heinz T F 2013 Real-time observation of interlayer vibrations in bilayer and few-layer graphene Nano Lett. 13 4620
[195] Jeong T Y et al 2016 Coherent lattice vibrations in mono- and few-layer WSe_2 ACS Nano 10 5560
[196] Ge S, Liu X, Qiao X, Wang Q, Xu Z, Qiu J, Tan P-H, Zhao J and Sun D 2014 Coherent longitudinal acoustic phonon approaching THz frequency in multilayer molybdenum disulphide Sci. Rep. 4 5722
[197] Mermin N D 1968 Crystalline order in two dimensions Phys. Rev. 176 250
[198] Landau L and Lifshitz E 1980 Statistical Physics, Part 1 vol 5 (Oxford: Pergamon)
[199] Katsnelson M and Novoselov K 2007 Graphene: new bridge between condensed matter physics and quantum electrodynamics Solid State Commun. 143 3
[200] Fasolino A, Los J and Katsnelson M I 2007 Intrinsic ripples in graphene Nat. Mater. 6 858
[201] Meyer J C, Geim A K, Katsnelson M I, Novoselov K S, Booth T J and Roth S 2007 The structure of suspended graphene sheets Nature 446 60
[202] Locatelli A, Knox K R, Cvetko D, Mentes T O, Nino M A, Wang S, Yilmaz M B, Kim P, Osgood R M and Morgante A 2010 Corrugation in exfoliated graphene: an electron microscopy and diffraction study ACS Nano 4 4879
[203] Katsnelson M and Geim A 2008 Electron scattering on microscopic corrugations in graphene Phil. Trans. R. Soc. A 366 195
[204] Shi H, Yan R, Bertolazzi S, Brivio J, Gao B, Kis A, Jena D, Xing H G and Huang L 2013 Exciton dynamics in suspended monolayer and few-layer MoS_2 2D crystals ACS Nano 7 1072
[205] Strait J H, Nene P and Rana F 2014 High intrinsic mobility and ultrafast carrier dynamics in multilayer metal-dichalcogenide MoS_2 Phys. Rev. B 90 245402
[206] Tielrooij K, Song J, Jensen S A, Centeno A, Pesquera A, Elorza A Z, Bonn M, Levitov L and Koppens F 2013 Photoexcitation cascade and multiple hot-carrier generation in graphene Nat. Phys. 9 248
[207] Nie Z, Long R, Sun L, Huang C-C, Zhang J, Xiong Q, Hewak D W, Shen Z, Prezhdo O V and Loh Z-H 2014 Ultrafast carrier thermalization and cooling dynamics in few-layer MoS_2 ACS Nano 8 10931
[208] Li Y, Rao Y, Mak K F, You Y, Wang S, Dean C R and Heinz T F 2013 Probing symmetry properties of few-layer MoS_2 and h-BN by optical second-harmonic generation Nano Lett. 13 3329
[209] Mannebach E M et al 2014 Ultrafast electronic and structural response of monolayer MoS_2 under intense photoexcitation conditions ACS Nano 8 10734
[210] Badali D S, Gengler R Y and Miller R 2016 Ultrafast electron diffraction optimized for studying structural dynamics in thin films and monolayers Struct. Dyn. 3 034302
[211] Gulde M, Schweda S, Storeck G, Maiti M, Yu H K, Wodtke A M, Schäfer S and Ropers C 2014 Ultrafast low-energy electron diffraction in transmission resolves polymer/graphene superstructure dynamics Science 345 200
[212] Mannebach E M et al 2015 Dynamic structural response and deformations of monolayer MoS_2 visualized by femtosecond electron diffraction Nano Lett. 15 6889
[213] Weathersby S P et al 2015 Mega-electron-volt ultrafast electron diffraction at SLAC national accelerator laboratory Rev. Sci. Instrum. 86 073702
[214] Lindenberg A M et al 2005 Atomic-scale visualization of inertial dynamics Science 308 392
[215] Zhang W, Wang Q, Chen Y, Wang Z and Wee A T 2016 Van der Waals stacked 2D layered materials for optoelectronics 2D Mater. 3 022001
[216] Hong X, Kim J, Shi S-F, Zhang Y, Jin C, Sun Y, Tongay S, Wu J, Zhang Y and Wang F 2014 Ultrafast charge transfer in atomically thin MoS_2/WS_2 heterostructures Nat. Nanotechnol. 9 682
[217] Ceballos F, Bellus M Z, Chiu H-Y and Zhao H 2014 Ultrafast charge separation and indirect exciton formation in a MoS_2–$MoSe_2$ van der Waals heterostructure ACS Nano 8 12717
[218] Peng B, Yu G, Liu X, Liu B, Liang X, Bi L, Deng L, Sum T C and Loh K P 2016 Ultrafast charge transfer in MoS_2/WSe_2 p–n Heterojunction 2D Mater. 3 025020
[219] Wang K et al 2016 Interlayer coupling in twisted WSe_2/WS_2 bilayer heterostructures revealed by optical spectroscopy ACS Nano 10 6612
[220] He J, Kumar N, Bellus M Z, Chiu H-Y, He D, Wang Y and Zhao H 2014 Electron transfer and coupling in graphene–tungsten disulfide van der Waals heterostructures Nat. Commun. 5 5622
[221] Zhu X, Monahan N R, Gong Z, Zhu H, Williams K W and Nelson C A 2015 Charge transfer excitons at van der Waals interfaces J. Am. Chem. Soc. 137 8313
[222] Long R and Prezhdo O V 2016 Quantum coherence facilitates efficient charge separation at a MoS_2/$MoSe_2$ van der Waals junction Nano Lett. 16 1996
[223] Wang H, Bang J, Sun Y, Liang L, West D, Meunier V and Zhang S 2016 The role of collective motion in the ultrafast charge transfer in van der Waals heterostructures Nat. Commun. 7 11504
[224] Roy T, Tosun M, Cao X, Fang H, Lien D-H, Zhao P, Chen Y-Z, Chueh Y-L, Guo J and Javey A 2015 Dual-Gated MoS_2/WSe_2 van der Waals tunnel diodes and transistors ACS Nano 9 2071
[225] Yan R et al 2015 Esaki diodes in van der Waals heterojunctions with broken-gap energy band alignment Nano Lett. 15 5791
[226] Roy T, Tosun M, Hettick M, Ahn G H, Hu C and Javey A 2016 2D–2D tunneling field-effect transistors using WSe_2/$SnSe_2$ heterostructures Appl. Phys. Lett. 108 083111
[227] Chuang S, Kapadia R, Fang H, Chia Chang T, Yen W-C, Chueh Y-L and Javey A 2013 Near-ideal electrical properties of InAs/WSe_2 van der Waals heterojunction diodes Appl. Phys. Lett. 102 242101
[228] Sarkar D, Xie X, Liu W, Cao W, Kang J, Gong Y, Kraemer S, Ajayan P M and Banerjee K 2015 A subthermionic tunnel field-effect transistor with an atomically thin channel Nature 526 91
[229] Xiong K, Luo X and Hwang J C M 2015 Phosphorene FETs-promising transistors based on a few layers of phosphorus atoms 2015 IEEE MTT-S Int. Microwave Workshop Series on Advanced Materials and Proc. RF and THz Applications (IMWS-AMP) (Piscataway, NJ: IEEE) 1–3
[230] Luo X, Rahbarihagh Y, Hwang J C M, Liu H, Du Y and Ye P D 2014 Temporal and thermal stability of Al_2O_3-passivated phosphorene MOSFETs IEEE Electr. Device L 35 1314
[231] Na J, Lee Y T, Lim J A, Hwang D K, Kim G-T, Choi W K and Song Y-W 2014 Few-layer black phosphorus field-effect transistors with reduced current fluctuation ACS Nano 8 11753
[232] Wood J D, Wells S A, Jariwala D, Chen K-S, Cho E, Sangwan V K, Liu X, Lauhon L J, Marks T J and Hersam M C

2014 Effective passivation of exfoliated black phosphorus transistors against ambient degradation *Nano Lett.* **14** 6964
[233] Kim J-S, Liu Y, Zhu W, Kim S, Wu D, Tao L, Dodabalapur A, Lai K and Akinwande D 2015 Toward air-stable multilayer phosphorene thin-films and transistors *Sci. Rep.* **5** 8989
[234] Miao J, Zhang S, Cai L, Scherr M and Wang C 2015 Ultrashort channel length black phosphorus field-effect transistors *ACS Nano* **9** 9236
[235] Gillgren N, Wickramaratne D, Shi Y, Espiritu T, Yang J, Hu J, Wei J, Liu X, Mao Z and Watanabe K 2014 Gate tunable quantum oscillations in air-stable and high mobility few-layer phosphorene heterostructures *2D Mater.* **2** 011001
[236] Avsar A, Vera-Marun I J, Tan J Y, Watanabe K, Taniguchi T, Castro Neto A H and Ozyilmaz B 2015 Air-stable transport in graphene-contacted, fully encapsulated ultrathin black phosphorus-based field-effect transistors *ACS Nano* **9** 4138
[237] Chen X *et al* 2015 High-quality sandwiched black phosphorus heterostructure and its quantum oscillations *Nat. Commun.* **6** 7315
[238] Wang Z, Islam A, Yang R, Zheng X and Feng P X-L 2015 Environmental, thermal, and electrical susceptibility of black phosphorus field effect transistors *J. Vac. Sci. Technol.* B **33** 052202
[239] Cao Y *et al* 2015 Quality heterostructures from two-dimensional crystals unstable in air by their assembly in inert atmosphere *Nano Lett.* **15** 4914
[240] Zhu W, Yogeesh M N, Yang S, Aldave S H, Kim J-S, Sonde S, Tao L, Lu N and Akinwande D 2015 Flexible black phosphorus ambipolar transistors, circuits and AM demodulator *Nano Lett.* **15** 1883
[241] Wang H, Wang X, Xia F, Wang L, Jiang H, Xia Q, Chin M L, Dubey M and Han S-J 2014 Black phosphorus radio-frequency transistors *Nano Lett.* **14** 6424
[242] Haratipour N, Robbins M C and Koester S J 2015 Black phosphorus p-MOSFETs with 7 nm HfO_2 gate dielectric and low contact resistance *IEEE Electron. Device Lett.* **36** 411
[243] Li L, Engel M, Farmer D B, Han S-J and Wong H-S P 2016 High-performance p-type black phosphorus transistor with scandium contact *ACS Nano* **10** 4672
[244] Wan B, Yang B, Wang Y, Zhang J, Zeng Z, Liu Z and Wang W 2015 Enhanced stability of black phosphorus field-effect transistors with SiO_2 passivation *Nanotechnology* **26** 435702
[245] Zhu W, Park S, Yogeesh M N, McNicholas K M, Bank S R and Akinwande D 2016 Black phosphorus flexible thin film transistors at gighertz frequencies *Nano Lett.* **16** 2301
[246] Luo X, Xiong K, Hwang J C M, Du Y and Ye P D 2016 Continuous-wave and transient characteristics of phosphorene microwave transistors *2015 IEEE MTT-S Int. Microwave Symp.* (Piscataway, NJ: IEEE) 1
[247] Voiry D, Mohite A and Chhowalla M 2015 Phase engineering of transition metal dichalcogenides *Chem. Soc. Rev.* **44** 2702
[248] Fan X, Xu P, Li Y C, Zhou D, Sun Y, Nguyen M A T, Terrones M and Mallouk T E 2016 Controlled exfoliation of MoS_2 crystals into trilayer nanosheets *J. Am. Chem. Soc.* **138** 5143
[249] Eda G, Yamaguchi H, Voiry D, Fujita T, Chen M and Chhowalla M 2011 Photoluminescence from chemically exfoliated MoS_2 *Nano Lett.* **11** 5111
[250] Allain A, Kang J, Banerjee K and Kis A 2015 Electrical contacts to two-dimensional semiconductors *Nat. Mater.* **14** 1195
[251] Das S, Chen H-Y, Penumatcha A V and Appenzeller J 2012 High performance multilayer MoS_2 transistors with scandium contacts *Nano Lett.* **13** 100
[252] Chuang S, Battaglia C, Azcatl A, McDonnell S, Kang J S, Yin X, Tosun M, Kapadia R, Fang H and Wallace R M 2014 MoS_2 P-type transistors and diodes enabled by high work function MoO_x contacts *Nano Lett.* **14** 1337
[253] Kappera R, Voiry D, Yalcin S E, Branch B, Gupta G, Mohite A D and Chhowalla M 2014 Phase-engineered low-resistance contacts for ultrathin MoS_2 transistors *Nat. Mater.* **13** 1128
[254] Voiry D, Yang J and Chhowalla M 2016 Recent strategies for improving the catalytic activity of 2D TMD nanosheets toward the hydrogen evolution reaction *Adv. Mater.* **28** 6197
[255] Voiry D *et al* 2016 The role of electronic coupling between substrate and 2D MoS_2 nanosheets in electrocatalytic production of hydrogen *Nat. Mater.* **15** 1003
[256] Jena D and Konar A 2007 Enhancement of carrier mobility in semiconductor nanostructures by dielectric engineering *Phys. Rev. Lett.* **98** 136805
[257] Radisavljevic B, Radenovic A, Brivio J, Giacometti V and Kis A 2011 Single-layer MoS_2 transistors *Nat. Nanotechnol.* **6** 147
[258] Pirkle A, Chan J, Venugopal A, Hinojos D, Magnuson C W, McDonnell S, Colombo L, Vogel E M, Ruoff R S and Wallace R M 2011 The effect of chemical residues on the physical and electrical properties of chemical vapor deposited graphene transferred to SiO_2 *Appl. Phys. Lett.* **99** 122108
[259] Chan J, Venugopal A, Pirkle A, McDonnell S, Hinojos D, Magnuson C W, Ruoff R S, Colombo L, Wallace R M and Vogel E M 2012 Reducing extrinsic performance-limiting factors in graphene grown by chemical vapor deposition *ACS Nano* **6** 3224
[260] Azcatl A *et al* 2014 MoS_2 functionalization for ultra-thin atomic layer deposited dielectrics *Appl. Phys. Lett.* **104** 111601
[261] Azcatl A, Santosh K, Peng X, Lu N, McDonnell S, Qin X, de Dios F, Addou R, Kim J and Kim M J 2015 HfO_2 on UV–O_3 exposed transition metal dichalcogenides: interfacial reactions study *2D Mater.* **2** 014004
[262] Park J H *et al* 2016 Atomic layer deposition of Al_2O_3 on WSe_2 functionalized by titanyl phthalocyanine *ACS Nano* **10** 6888
[263] Das S, Chen H-Y, Penumatcha A V and Appenzeller J 2013 High performance multi-layer MoS_2 transistors with scandium contacts *Nano Lett.* **13** 100
[264] Gong C, Colombo L, Wallace R M and Cho K 2014 The unusual mechanism of partial fermi level pinning at metal-MoS_2 interfaces *Nano Lett.* **14** 1714
[265] Liu D, Guo Y, Fang L and Robertson J 2013 Sulfur vacancies in monolayer MoS_2 and its electrical contacts *Appl. Phys. Lett.* **103** 183113
[266] McGovern I, Dietz E, Rotermund H, Bradshaw A, Braun W, Radlik W and McGilp J 1985 Soft x-ray photoemission spectroscopy of metal-molybdenum bisulphide interfaces *Surf. Sci.* **152** 1203
[267] Durbin T D, Lince J R and Yarmoff J A 1992 Chemical interaction of thin Cr films with the MoS_2(0001) surface studied by x-ray photoelectron spectroscopy and scanning Auger microscopy *J. Vac. Sci. Technol.* A **10** 2529
[268] Lince J R, Carre D J and Fleischauer P D 1987 Schottky-barrier formation on a covalent semiconductor without fermi-level pinning: the metal-MoS_2(0001) interface *Phys. Rev.* B **36** 1647
[269] Domask A, Gurunathan R and Mohney S 2015 Transition metal–MoS_2 reactions: review and thermodynamic predictions *J. Electron. Mater.* **44** 4065
[270] English C D, Shine G, Dorgan V E, Saraswat K C and Pop E 2016 Improved contacts to MoS_2 transistors by ultra-high vacuum metal deposition *Nano Lett.* **16** 3824
[271] McDonnell S, Smyth C, Hinkle C L and Wallace R M 2016 MoS_2–titanium contact interface reactions *ACS Appl. Mater. Interfaces* **8** 8289
[272] Feng L-P, Su J, Li D-P and Liu Z-T 2015 Tuning the electronic properties of Ti–MoS_2 contacts through introducing vacancies in monolayer MoS_2 *Phys. Chem. Chem. Phys.* **17** 6700
[273] Kang J, Sarkar D, Liu W, Jena D and Banerjee K 2012 A computational study of metal-contacts to beyond-graphene 2D semiconductor materials *2012 IEEE Int. Electron Devices Meeting (IEDM)* (Piscataway, NJ: IEEE) 17.4. 1
[274] Guimarães M H, Gao H, Han Y, Kang K, Xie S, Kim C-J, Muller D A, Ralph D C and Park J 2016 Atomically-thin ohmic edge contacts between two-dimensional materials *ACS Nano* **10** 6392

[275] Wang J I-J, Yang Y, Chen Y-A, Watanabe K, Taniguchi T, Churchill H O and Jarillo-Herrero P 2015 Electronic transport of encapsulated graphene and WSe_2 devices fabricated by pick-up of prepatterned hBN *Nano Lett.* **15** 1898
[276] Lee G H *et al* 2015 Highly stable, dual-gated MoS_2 transistors encapsulated by hexagonal boron nitride with gate-controllable contact, resistance, and threshold voltage *ACS Nano* **9** 7019
[277] Secor E B and Hersam M C 2015 Emerging carbon and post-carbon nanomaterial inks for printed electronics *J. Phys. Chem. Lett.* **6** 620
[278] Green A A and Hersam M C 2009 Solution phase production of graphene with controlled thickness via density differentiation *Nano Lett.* **9** 4031
[279] Zhu J, Kang J, Kang J, Jariwala D, Wood J D, Seo J-W T, Chen K-S, Marks T J and Hersam M C 2015 Solution-processed dielectrics based on thickness-sorted two-dimensional hexagonal boron nitride nanosheets *Nano Lett.* **15** 7029
[280] Zhu J, Liu X, Geier M L, McMorrow J J, Jariwala D, Beck M E, Huang W, Marks T J and Hersam M C 2016 Layer-by-layer assembled 2D montmorillonite dielectrics for solution-processed electronics *Adv. Mater.* **28** 63
[281] Kang J, Seo J-W T, Alducin D, Ponce A, Yacaman M J and Hersam M C 2014 Thickness sorting of two-dimensional transition metal dichalcogenides via copolymer-assisted density gradient ultracentrifugation *Nat. Commun.* **5** 5478
[282] Kang J, Wood J D, Wells S A, Lee J-H, Liu X, Chen K-S and Hersam M C 2015 Solvent exfoliation of electronic-grade, two-dimensional black phosphorus *ACS Nano* **9** 3596
[283] Kang J, Wells S A, Wood J D, Lee J H, Liu X, Ryder C R, Zhu J, Guest J R, Husko C A and Hersam M C 2016 Stable aqueous dispersions of optically and electronically active phosphorene *Proc. Natl Acad. Sci. USA* **113** 11688
[284] Kang J, Wells S A, Wood J D, Lee J-H, Liu X, Ryder C R, Zhu J, Guest J R, Husko C A and Hersam M C 2016 arXiv:1604.05677
[285] Secor E B, Prabhumirashi P L, Puntambekar K, Geier M L and Hersam M C 2013 Inkjet printing of high conductivity, flexible graphene patterns *J. Phys. Chem. Lett.* **4** 1347
[286] Secor E B, Lim S, Zhang H, Frisbie C D, Francis L F and Hersam M C 2014 Gravure printing of graphene for large-area flexible electronics *Adv. Mater.* **26** 4533
[287] Hyun W J, Secor E B, Hersam M C, Frisbie C D and Francis L F 2015 High-resolution patterning of graphene by screen printing with a silicon stencil for highly flexible printed electronics *Adv. Mater.* **27** 109
[288] Jakus A E, Secor E B, Rutz A L, Jordan S W, Hersam M C and Shah R N 2015 Three-dimensional printing of high-content graphene scaffolds for electronic and biomedical applications *ACS Nano* **9** 4636
[289] Secor E B, Ahn B Y, Gao T Z, Lewis J A and Hersam M C 2015 Rapid and versatile photonic annealing of graphene inks for flexible printed electronics *Adv. Mater.* **27** 6683
[290] Jariwala D, Sangwan V K, Wu C-C, Prabhumirashi P L, Geier M L, Marks T J, Lauhon L J and Hersam M C 2013 Gate-tunable carbon nanotube–MoS_2 heterojunction pn diode *Proc. Natl Acad. Sci. USA* **110** 18076
[291] Jariwala D, Sangwan V K, Seo J-W T, Xu W, Smith J, Kim C H, Lauhon L J, Marks T J and Hersam M C 2014 Large-area, low-voltage, antiambipolar heterojunctions from solution-processed semiconductors *Nano Lett.* **15** 416
[292] Sangwan V K, Jariwala D, Kim I S, Chen K-S, Marks T J, Lauhon L J and Hersam M C 2015 Gate-tunable memristive phenomena mediated by grain boundaries in single-layer MoS_2 *Nat. Nanotechnol.* **10** 403
[293] Jariwala D, Howell S L, Chen K-S, Kang J, Sangwan V K, Filippone S A, Turrisi R, Marks T J, Lauhon L J and Hersam M C 2016 Hybrid, gate-tunable, van der Waals p–n Heterojunctions from pentacene and MoS_2 *Nano Lett.* **16** 497
[294] Reimer L 2013 *Transmission Electron Microscopy: Physics of Image Formation and Microanalysis* vol 36 (Berlin: Springer)
[295] Storm A, Chen J, Ling X, Zandbergen H and Dekker C 2003 Fabrication of solid-state nanopores with single-nanometre precision *Nat. Mater.* **2** 537
[296] Xu Q, Wu M-Y, Schneider G F, Houben L, Malladi S K, Dekker C, Yucelen E, Dunin-Borkowski R E and Zandbergen H W 2013 Controllable atomic scale patterning of freestanding monolayer graphene at elevated temperature *ACS Nano* **7** 1566
[297] Qi Z J, Rodriguez-Manzo J A, Botello-Mendez A R, Hong S J, Stach E A, Park Y W, Charlier J C, Drndic M and Johnson A T 2014 Correlating atomic structure and transport in suspended graphene nanoribbons *Nano Lett.* **14** 4238
[298] Masih Das P *et al* 2016 Controlled sculpture of black phosphorus nanoribbons *ACS Nano* **10** 5687
[299] Xie P, Xiong Q, Fang Y, Qing Q and Lieber C M 2012 Local electrical potential detection of DNA by nanowire-nanopore sensors *Nat. Nanotechnol.* **7** 119
[300] Traversi F, Raillon C, Benameur S, Liu K, Khlybov S, Tosun M, Krasnozhon D, Kis A and Radenovic A 2013 Detecting the translocation of DNA through a nanopore using graphene nanoribbons *Nat. Nanotechnol.* **8** 939
[301] Puster M, Rodríguez-Manzo J A, Balan A and Drndic M 2013 Toward sensitive graphene nanoribbon–nanopore devices by preventing electron beam-induced damage *ACS Nano* **7** 11283
[302] Puster M, Balan A, Rodríguez-Manzo J A, Danda G, Ahn J-H, Parkin W and Drndić M 2015 Cross-talk between ionic and nanoribbon current signals in graphene nanoribbon-nanopore sensors for single-molecule detection *Small* **11** 6309
[303] Lu Y, Merchant C A, Drndic M and Johnson A C 2011 In situ electronic characterization of graphene nanoconstrictions fabricated in a transmission electron microscope *Nano Lett.* **11** 5184
[304] Rodriguez-Manzo J A, Qi Z J, Crook A, Ahn J H, Johnson A T and Drndic M 2016 In situ transmission electron microscopy modulation of transport in graphene nanoribbons *ACS Nano* **10** 4004
[305] Cretu O, Botello-Mendez A R, Janowska I, Pham-Huu C, Charlier J C and Banhart F 2013 Electrical transport measured in atomic carbon chains *Nano Lett.* **13** 3487
[306] Balan A, Chien C-C, Engelke R and Drndić M 2015 Suspended solid-state membranes on glass chips with sub 1-pF capacitance for biomolecule sensing applications *Sci. Rep.* **5** 17775
[307] Shekar S, Niedzwiecki D J, Chien C-C, Ong P, Fleischer D A, Lin J, Rosenstein J K, Drndic M and Shepard K L 2016 Measurement of DNA translocation dynamics in a solid-state nanopore at 100 ns temporal resolution *Nano Lett.* **16** 4483
[308] Fischbein M D and Drndić M 2008 Electron beam nanosculpting of suspended graphene sheets *Appl. Phys. Lett.* **93** 113107
[309] Merchant C A *et al* 2010 DNA translocation through graphene nanopores *Nano Lett.* **10** 2915
[310] Schneider G F, Kowalczyk S W, Calado V E, Pandraud G, Zandbergen H W, Vandersypen L M and Dekker C 2010 DNA translocation through graphene nanopores *Nano Lett.* **10** 3163
[311] Garaj S, Hubbard W, Reina A, Kong J, Branton D and Golovchenko J 2010 Graphene as a subnanometre trans-electrode membrane *Nature* **467** 190
[312] Liu K, Feng J, Kis A and Radenovic A 2014 Atomically thin molybdenum disulfide nanopores with high sensitivity for DNA translocation *ACS Nano* **8** 2504
[313] Liu S *et al* 2013 Boron nitride nanopores: highly sensitive DNA single-molecule detectors *Adv. Mater.* **25** 4549
[314] Kwok H, Briggs K and Tabard-Cossa V 2014 Nanopore fabrication by controlled dielectric breakdown *PloS One* **9** e92880
[315] Yanagi I, Akahori R, Hatano T and Takeda K-I 2014 Fabricating nanopores with diameters of sub-1 nm to 3 nm using multilevel pulse-voltage injection *Sci. Rep.* **4** 5000

[316] Kuan A T, Lu B, Xie P, Szalay T and Golovchenko J A 2015 Electrical pulse fabrication of graphene nanopores in electrolyte solution *Appl. Phys. Lett.* **106** 203109
[317] Feng J *et al* 2015 Electrochemical reaction in single layer MoS_2: nanopores opened atom by atom *Nano Lett.* **15** 3431
[318] Rodríguez-Manzo J A, Puster M, Nicolaï A, Meunier V and Drndic M 2015 DNA translocation in nanometer thick silicon nanopores *ACS Nano* **9** 6555
[319] Thiemann S, Sachnov S, Porscha S, Wasserscheid P and Zaumseil J 2012 Ionic liquids for electrolyte-gating of ZnO field-effect transistors *J. Phys. Chem.* C **116** 13536
[320] Zhang J, Triola C and Rossi E 2014 Proximity effect in graphene–topological-insulator heterostructures *Phys. Rev. Lett.* **112** 096802
[321] Tizei L H G, Lin Y-C, Mukai M, Sawada H, Lu A-Y, Li L-J, Kimoto K and Suenaga K 2015 Exciton mapping at subwavelength scales in two-dimensional materials *Phys. Rev. Lett.* **114** 107601
[322] Ceballos F, Cui Q, Bellus M Z and Zhao H 2016 Exciton formation in monolayer transition metal dichalcogenides *Nanoscale* **8** 11681
[323] Steinhoff A, Kim J-H, Jahnke F, Rosner M, Kim D-S, Lee C, Han G H, Jeong M S, Wehling T O and Gies C 2015 Efficient excitonic photoluminescence in direct and indirect band gap monolayer MoS_2 *Nano Lett.* **15** 6841
[324] Rosner M, Steinke C, Lorke M, Gies C, Jahnke F and Wehling T O 2016 Two-dimensional heterojunctions from nonlocal manipulations of the interactions *Nano Lett.* **16** 2322
[325] Mak K F and Shan J 2016 Photonics and optoelectronics of 2D semiconductor transition metal dichalcogenides *Nat. Photon.* **10** 216
[326] Fogler M, Butov L and Novoselov K 2014 High-temperature superfluidity with indirect excitons in van der Waals heterostructures *Nat. Commun.* **5** 4555
[327] Guo Y, Sun D, Ouyang B, Raja A, Song J, Heinz T F and Brus L E 2015 Probing the dynamics of the metallic-to-semiconducting structural phase transformation in MoS_2 crystals *Nano Lett.* **15** 5081
[328] Hersam M C 2015 The reemergence of chemistry for post-graphene two-dimensional nanomaterials *ACS Nano* **9** 4661
[329] Ryder C R, Wood J D, Wells S A and Hersam M C 2016 Chemically tailoring semiconducting two-dimensional transition metal dichalcogenides and black phosphorus *ACS Nano* **10** 3900
[330] Hersam M C 2015 Defects at the two-dimensional limit *J. Phys. Chem. Lett.* **6** 2738
[331] Liu X, Balla I, Bergeron H and Hersam M C 2016 Point defects and grain boundaries in rotationally commensurate MoS_2 on epitaxial graphene *J. Phys. Chem.* C **120** 20798
[332] Kang J, Jariwala D, Ryder C R, Wells S A, Choi Y, Hwang E, Cho J H, Marks T J and Hersam M C 2016 Probing out-of-plane charge transport in black phosphorus with graphene-contacted vertical field-effect transistors *Nano Lett.* **16** 2580
[333] Mannix A J *et al* 2015 Synthesis of borophenes: anisotropic, two-dimensional boron polymorphs *Science* **350** 1513
[334] Waduge P, Bilgin I, Larkin J, Henley R Y, Goodfellow K, Graham A C, Bell D C, Vamivakas N, Kar S and Wanunu M 2015 Direct and scalable deposition of atomically thin low-noise MoS_2 membranes on apertures *ACS Nano* **9** 7352